Modeling Towards Lattice-Matched

Dilute Nitride GaNPAs on Silicon Multijunction Solar Cells

by

Yongjie Zou

A Dissertation Presented in Partial Fulfillment
of the Requirements for the Degree
Doctor of Philosophy

Approved July 2019 by the
Graduate Supervisory Committee:

Stephen M. Goodnick, Chair
Christiana B. Honsberg
Richard R. King
Dragica Vasileska

ARIZONA STATE UNIVERSITY

August 2019

ABSTRACT

Silicon photovoltaics is the dominant contribution to the global solar energy production. As increasing conversion efficiency has become one of the most important factors to lower the cost of photovoltaic systems, the idea of making a multijunction solar cell based on a silicon bottom cell has attracted broad interest. Here the potential of using dilute nitride GaNPAs alloys for a lattice-matched 3-terminal 2-junction Si-based tandem solar cell through multiscale modeling is investigated. To calculate the electronic band structure of dilute nitride alloys with relatively low computational cost, the $sp^3d^5s^*s_N$ tight-binding model is chosen, as it has been demonstrated to obtain quantitatively correct trends for the lowest conduction band near Γ, L, and X for dilute-N GaNAs. A genetic algorithm is used to optimize the $sp^3d^5s^*$ tight-binding model for pure GaP and GaAs for their optical properties. Then the optimized $sp^3d^5s^*s_N$ parametrizations are obtained for GaNP and GaNAs by fitting to experimental bandgap values. After that, a virtual crystal approach gives the Hamiltonian for GaNPAs alloys. From their tight-binding Hamiltonian, the first-order optical response functions of dilute nitride GaNAs, GaNP, and GaNPAs are calculated. As the N mole fraction varies, the calculated critical optical features vary with the correct trends, and agree well with experiment. The calculated optical properties are then used as input for the solar device simulations based on Silvaco ATLAS. For device simulation, a bottom cell model is first constructed to generate performance results that agree well with a demonstrated high-efficiency Si heterojunction interdigitated back contact (IBC) solar cell reported by Kaneka. The front a-Si/c-Si interface is then replaced by a GaP/Si interface for the investigation of the sensitivity of the GaP/Si interface to interface defects in terms of degradation of the IBC cell performance, where we find that

an electric field that induces strong band bending can significantly mitigate the impact of the interfacial traps. Finally, a lattice-matched 3-terminal 2-junction tandem model is built for performance simulation by stacking a dilute nitride GaNP(As) cell on the Si IBC cell connected through a GaP/Si interface. The two subcells operate quasi-independently. In this 3-terminal tandem model, traps at the GaP/Si interface still significantly impact the performance of the Si subcell, but their effects on the GaNP subcell are relatively small. Assuming the interfacial traps are well passivated, the tandem efficiency surpasses that of a single-junction Si cell, with values close to 33% based on realistic parameters.

ACKNOWLEDGMENTS

I would like to acknowledge those who have helped me advance through my Ph.D. program, those from whom I'm still trying to learn to improve myself as a person and as a researcher, and those who have shared their love and support with me.

First, I would like to thank my Ph.D. advisor, Prof. Stephen Goodnick for giving me the chance to do research on solid-state physics that can be applied to photovoltaics, although I didn't have much background in physics to start my Ph.D. program. Thank you for being such a deep and vast "knowledge pool" whenever I brought questions to you on a regular basis. And your humor and cheerful support made the mentally challenging days much easier.

Chapter 1 involves my knowledge in detailed balance modeling, which I gained from a short-term project on making a multijunction detailed balance code to work. This set my foot in the door of photovoltaic research. I should thank Prof. Honsberg and Prof. Bowden for giving me my very first project at ASU.

I also thank Prof. Holman for giving me the opportunity to explore a bit in experimental PV research in the early days of my Ph.D. program, by letting me to work on a summer project with very well-defined goals and tasks. Although I didn't continue that project, some of the skills I learned, especially the scientific writing habits, are transferable. I wish I have had practiced these habits through my entire Ph.D. life, as I realize.

I also want to thank Prof. Vasileska for sharing your knowledge and patience when I needed help in equation derivation and coding. And Rebecca, Patty, Margie, Ruby, and Katie, thanks for your helps in countless scheduling and paperwork.

I'm thankful to be part of ERC 525. Have you ever seen the rocks conglomerate in an office? I have, thanks to the "rock (climbing and music) trio" Prad, Robin, and Josh. As far as I remember, they keep rocking the world every minute. Sorry Prad for not going with you last week. Natasa, the runner, cheerleader, happy hour organizer, multi-national researcher, thanks for being a great inspiration and support to me. Abdul, the hacker, who seems to be able to solve all tough problems, thanks for all the helpful discussions.

To the folks I've met in my outdoor adventures, thanks for sharing a salmon pack, or water, or a tent, or a photo, or laughter with me. It's pure happiness to spend time with you in the best place, Nature! Especially Jordan, thank you for keeping me company for the past few years. Michelle, Dongyi, and Sensei Dave, I'm happy to be able to learn some wonderful skills from you.

And of course, I'm most indebted to my family. Thank you for your love, understanding, and support, without which I may not have quit my job and started this journey.

TABLE OF CONTENTS

Page

CHAPTER Page

CHAPTER Page

LIST OF TABLES

Table Page

LIST OF FIGURES

Figure Page

Figure Page

Figure Page

Figure Page

Chapter 1

INTRODUCTION

1.1 Introduction to Photovoltaics

Photovoltaic (PV) devices, also called solar cells, convert absorbed photons into charge carriers. Connecting a PV cell under illumination to a resistive load extracts electric power from it. In 1954, Bell Laboratories reported the first practical silicon solar cell based on a p-n junction, demonstrating an efficiency of 6% [1]. Improving the efficiency of solar cells has been one of the main goals of both academic and industrial research on PV. To estimate the potential of a material for making solar cells in terms of efficiency, Shockley and Queisser used a detailed balance model to calculate the ideal efficiency limits of single-junction (or single-transition-gap) solar cells [2]. Figure 1.1 shows the detailed balance limits of single-junction solar cells, assuming radiative emission only exit the cells from the front due to perfect back reflectors [3]. The maximum detailed balance limit of a single-junction solar cell under AM1.5G one sun is 33.7% at a bandgap of 1.34 eV [4]. By the end of 2017, under standard conditions (AM1.5G, 1000 W/m^2 or one sun, 25 °C), the highest verified efficiency of single-crystal silicon solar cells was 26.7% [5], while for GaAs solar cells, the best efficiency to date is 29.1% [6]. These efficiency records for Si and GaAs single-junction cells are already close to the theoretical maximum values for a single-bandgap device.

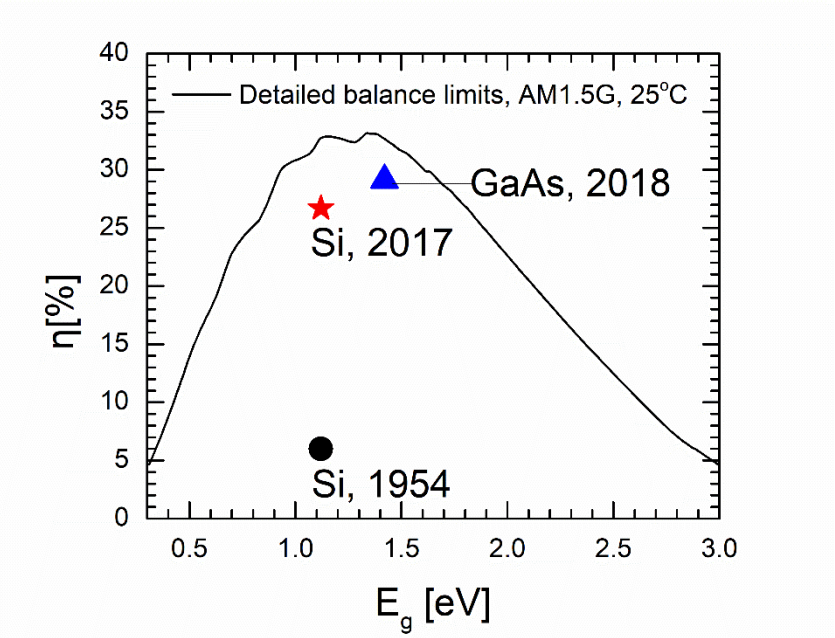

Figure 1.1 Detailed balance limits of single-junction solar cells with perfect back-side reflectors (under AM1.5G, one sun, 25 °C) [3]. The current record efficiencies of Si and GaAs solar cells are also indicated by symbols [6].

There are a number of assumptions in the Shockley-Queisser (SQ) analysis, which include no photon absorption below the bandgap, that all photons with above-bandgap energies are absorbed, that each absorbed photon converts into one electron-hole pair, and that all photo-generated carriers are extracted at the band edges. As shown in Figure 1.2 [7], the two main components of energy loss in solar cells are the relaxation loss and the loss of below-bandgap photons. That is, if the photo-generated carriers have excess energy with respect to the band edges, they relax to the band edges quickly, and the energy difference is transferred to the lattice as heat, and if the photon energy is smaller than the bandgap, they are not absorbed. Other losses include radiative recombination and the difference between the applied bias and the bandgap [7].

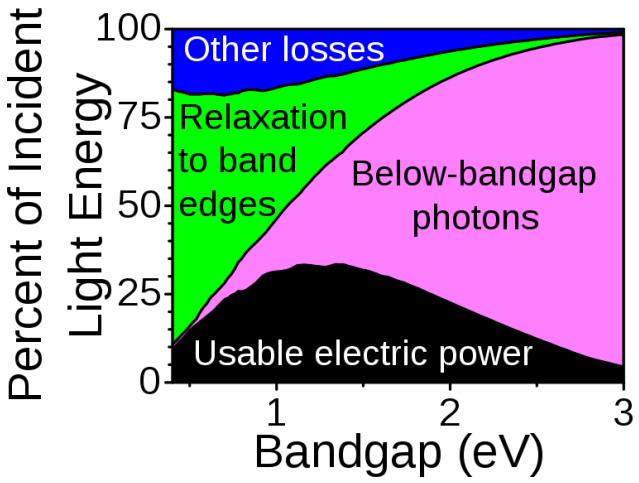

Figure 1.2 Energy losses in solar cells above the Shockley-Queisser limits (black area) [7].

Advanced-concept solar cells are designed to go beyond the SQ limit, by circumventing the assumptions in the SQ analysis. They include multijunction solar cells, hot-carrier solar cells, multi-exciton generation solar cells, intermediate-band solar cells, and thermophotovoltaics [8].

1.2 Multijunction Solar Cells

Multijunction solar cells, or tandem solar cells if the subcells are stacked vertically, have been successfully demonstrated with efficiencies higher than the SQ limit. Figure 1.3 shows that multijunction solar cells can reduce the two main energy loss mechanisms in solar cells, i.e., thermalization loss and below-bandgap photon loss, by stacking multiple materials with different bandgaps along the optical pathway.

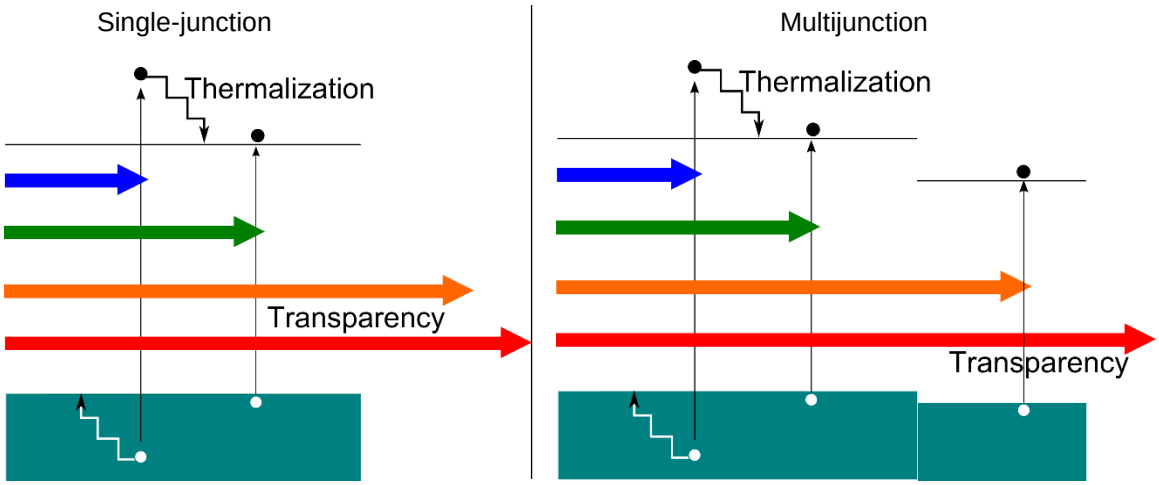

Figure 1.3 Energy losses in solar cells through carrier thermalization and sub-bandgap photon passing through the solar active material can be reduced by multijunction structures.

Detailed balance calculations have been performed on multijunction solar cells [4], [9]–[11], by lifting the single-bandgap assumption. The efficiency limits for different numbers of junctions correspond to different bandgap combinations, dictated by the incident spectrum and by the electrical connection. The subcells in multijunction solar cells can be connected either in series (constrained) or independently (unconstrained). With these two different connection types, the engineering of the tradeoff between thermalization loss and transmission loss is different. The detailed balance efficiencies under AM1.5G 1 sun illumination of these two connection types have been calculated for two-junction tandems with the bottom cell absorber fixed at the Si bandgap (1.12 eV), and are plotted as a function of the top cell bandgap in Figure 1.4. In series connection, there is a current matching requirement. Any current mismatch reduces the tandem efficiency significantly. Therefore, the optimal top cell bandgap peaks very sharply near 1.7 eV, giving 45.1%. Without the current matching requirement (in independent connection), it is slightly better to reduce the thermalization loss of the photons with energies higher than 1.8 eV, boosting

the tandem efficiency to 45.3%, and the peak becomes smooth and broad. In this case, tandem efficiency is above 44.9% for top cell bandgap between 1.7 eV and 2.0 eV.

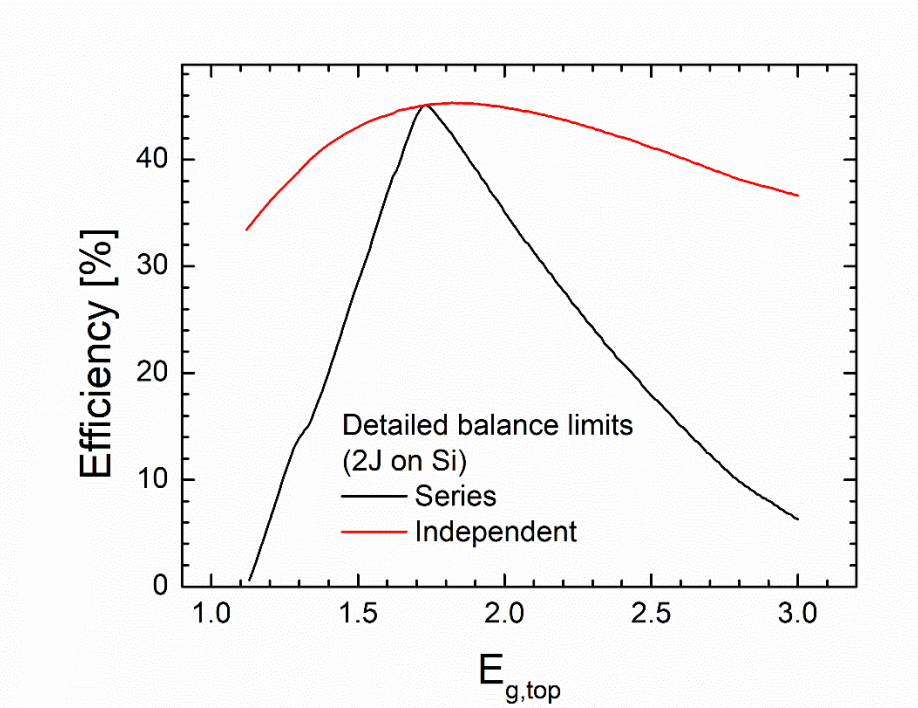

Figure 1.4 Detailed balance efficiency for two-junction tandem with a Si bottom cell under 1x AM1.5G illumination [12]. The black and red curves show the efficiencies for the case of series connection and of independent connection, respectively.

To date, the highest solar cell efficiency is 46.0%, achieved with a GaInP/GaAs; GaInAsP/GaInAs bonded four-junction solar cell [13]. However, for flat-plate or low-x (low-concentration) solar applications, these tandems are not cost competitive.

Silicon solar cells are low-cost with high performance for single-gap cells, and currently dominate the PV market (> 90%). One way to capitalize on the existing infrastructure of Si cell manufacturing is to realize multijunction solar cells based on Si subcells.

There have been different efforts in improving the technologies of making Si-based multijunction solar cells. Recently, a collaborative work by Ohio State University, SolAero Technologies Corp., and University of New South Wales made a monolithic GaAsP/Si 2-terminal (2T) tandem with 20.1% efficiency [6]. Feifel *et al*. [14] also used the direct growth approach and made a GaInP/GaAs/Si 2T tandem with a metamorphic buffer layer, reaching an efficiency of 22.3%. Within the same material system, Cariou *et al*. [15] fabricated a GaInP/GaAs/Si 2T tandem through wafer bonding and achieved an efficiency of 33.3%. Essig *et al*. [16] used the mechanical stacking approach and made 32.8% GaAs/Si and 35.9% GaInP/GaAs/Si 4-terminal (4T) tandems. Besides III-V on Si, perovskite on Si has become a popular material system for multijunction solar cells. Jošt *et al*. [17] made a 25.5% perovskite/Si 2T tandem with a textured light management foil on the front side. Oxford PV announced [18] a 28% 2T perovskite/Si tandem, surpassing the current record efficiency of single-junction Si cell.

A 2T tandem can be fabricated monolithically and has advantage in simple interconnection, but the current matching constrain makes the search for the perfect material for Si-based tandem difficult. A 4T tandem does not require current matching, and thus allows more flexible material selection and higher spectral tolerance. However, at least two growth substrates are needed for one 4T tandem, and additional power electronics are required for interconnection. A 3-terminal tandem has the advantages of the 2T and 4T schemes, although the interconnection is still more complicated than the 2T case. There has been a continuous effort by a team from the National Renewable Energy Laboratory in understanding 3T GaInP/Si lattice-mismatched tandems, using a transparent conductive

adhesive as a tunnel junction [19], [20]. In this work, we investigate the lattice-matched approach for 3T Si-based tandems.

Figure 1.5 shows the bandgap energies of major group-IV, III-V, II-VI, and IV-VI materials as a function of lattice constant [21]. ZnS, AlP, and GaP have lattice constants close to that of Si, but their absorption edges are too high to make high-efficiency Si-based tandems (see Figure 1.4). GaNP(As) alloys, a group of dilute nitrides, can be grown lattice-matched to Si and can cover a bandgap range between 1.5–2.0 eV [22], and are therefore good candidates for making Si-based multijunction solar cells.

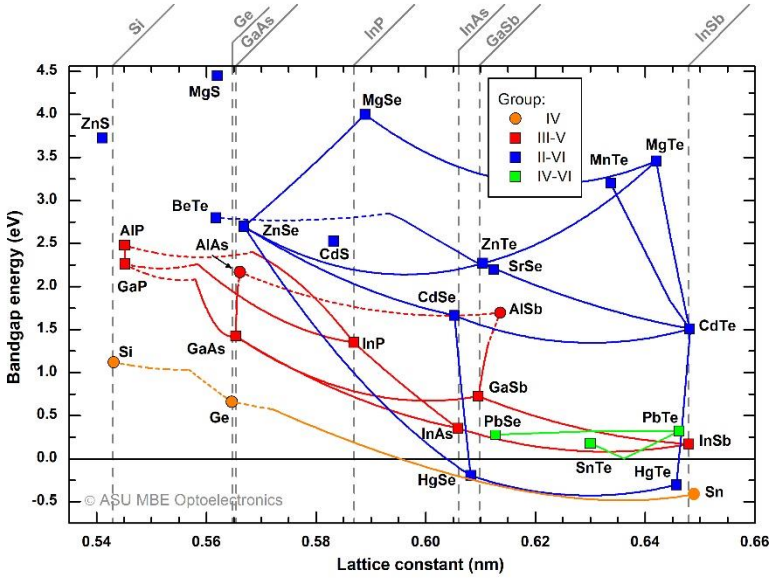

Figure 1.5 Bandgap energies of major group-IV, III-V, II-VI, and IV-VI materials as a function of lattice constant (Adapted from Ref. [21]).

1.3 Introduction to Dilute Nitrides

Weyers et al. found that replacing 1.4% of As atoms with N atoms in GaAs lowers its bandgaps by 0.17 eV at 77 K [23]. This was optically measured on samples grown with the metalorganic chemical vapor deposition (MOCVD) technique. Later on, similar trends in the bandgaps of GaN_xAs_{1-x} alloys in the dilute [N] limit were reproduced on samples grown by gas-source molecular beam epitaxy (GS-MBE) [24], by pseudopotential calculations with large supercells [25], [26], as well as by other works [27], [28]. This kind of drastic bandgap reduction by such a small fraction of isovalent atoms is generally unseen in other alloys, but it is also observed in GaN_xP_{1-x} [29]–[31], InN_xP_{1-x} [32], [33], InN_xAs_{1-x} [34], InN_xSb_{1-x} [35], and GaN_xSb_{1-x} [14], with *x* typically smaller than 0.05. This distinct group of alloys are called dilute nitrides.

Having exceptionally large bowing of the bandgaps with respect to their chemical compositions, accompanied by the gradual changes in lattice constants, dilute nitrides can be used to make many lattice-matched heterostructures on GaAs (or Ge) substrates, e.g. GaInNAs/GaAs, and on Si substrates, e.g. GaNP(As)/Si for applications in light-emitting devices/optoelectronic integrated circuits [24], and multijunction photovoltaic cells [22]. Using dilute nitride as the material for the bottom cell, a monolithic GaInP/GaAs/GaInNAs multijunction solar cell was fabricated, exhibiting a conversion efficiency of 44% under 942 suns [36], [37].

Although pure GaP is an indirect bandgap material, N-doped GaP was traditionally used as an active material for light-emitting diodes from green to yellow lighting [38], [39], with the N traps acting as efficient radiative emission centers. But not until molecular beam

epitaxy (MBE) is used for the growth of GaP, N incorporation was limited to less than 2×10^{20} cm^{-3}. Baillargeon *et al*. [29] were able to use MBE to grow GaN_xP_{1-x} with x as high as 3.4%, and they found that the photoluminescence (PL) peak red shifts as the N concentration increases above a threshold. Based on the measured decrease in the PL intensity from N concentration of 1×10^{20} cm^{-3} to 6×10^{20} cm^{-3}, they argued that the material has an indirect fundamental bandgap. Using the dielectric theory of electronegativity (DTE) developed by Van Vechten [40], they predicted that GaN_xP_{1-x} would show semimetallic and metallic behaviors if x could be as high as 0.27–0.66, and a transformation from indirect bandgap to direct bandgap near $x = 0.43$. Liu *et al.* [30] and Bi and Tu [31] also attributed the square root relations of the absorption spectra measured from their samples, $x \leq 0.024$ and $x \leq 0.16$, respectively, to the bandgaps being indirect. Bi and Tu [31] observed a much smaller bandgap bowing than the one derived by Baillargeon *et al.* [29], and they suggested that GaNP is a semiconductor rather than a semimetal. Using empirical pseudopotential calculations on 512-atom supercells, Bellaiche *et al.* [26] predicted the indirect-direct bandgap crossover occur around $x = 0.03$.

However, Xin *et al.* measured room-temperature PL from their GaNP samples of high crystalline quality, verified by x-ray rocking curves, and found the PL intensities increase from $x = 0.007$ to 0.013, and decrease for x above 0.013. They argued that the bandgaps of the GaNP samples are direct in nature and that the increased strain in samples with x higher than 0.013 lowers the crystal quality and hence the PL intensities. They suggested the earlier experimental conclusions of the GaNP bandgaps being indirect were probably due to low material quality, which is plausible, especially for the samples with x up to 0.16, as the solid solubility of GaN into GaP should be limited to a few percent [41]. Shan *et al.*

[42] also showed, with photomodulated transmission and reflectance experiment, that the bandedge transition E_- of GaNP are direct in nature, which cannot be detected in the indirect-bandgap GaP. In addition, they resolved a higher-energy transition, E_+, with photoreflectance, and they were able to explain the nitrogen concentration (≥ 0.003) dependence of both the E_- and E_+ with the band anti-crossing model they proposed earlier [43], [44]. Ilahi et al. [45] and Zelazna et al. [46] also measured direct-bandgap optical transitions in P-rich GaNPAs, which, without N, would be in the indirect-bandgap alloy range of GaPAs.

1.4 Dilute Nitrides/Si for Low-cost Two-junction Solar Cells

The key to make Si-based tandems commercially viable is to take advantage of the low-cost Si bottom cell and grow the top cell directly on Si, where lattice-matched epitaxy is needed to maximize the material quality.

Dilute nitride (dilute-N) $GaN_xP_{1-x-y}As_y$ has a bandgap range covering 1.7 eV [47], and is lattice-matched to Si when $y = 0.098 + 4.636x$, according to Vegard's law, which has shown excellent agreement with first-principle calculations [48] and X-ray measurements [49]. Thus, there has been interest recently in making GaNPAs (1.7 eV)/Si (1.1 eV) series-connected 2J tandem cells [50]–[52].

However, dilute nitrides (III-N-V alloys with dilute mole fraction of N) generally exhibit short minority carrier diffusion lengths [22], probably due to the large size differences between N atoms and the matrix isovalent atoms, the breaking of periodicity, and non-optimized growth processes. As a result, dilute nitride solar cells to date usually show low quantum efficiency and small photo-current. This suggests that dilute nitrides

are not a good choice for making series-connected solar cells with Si, because of the side effects of current matching.

To make a dilute nitride/Si 2J tandem, a more promising configuration is a parallel connection. With this approach, the performance of the bottom Si cell will not be significantly affected by the lower current from the dilute nitride cell, and the efficiency boost from adding a lower-performance cell on a Si cell is more likely, as discussed later.

The goal of this work is to study to the material properties of dilute-N GaNP(As), GaNP(As) hereafter, and to gauge the potential of using them to make low-cost high-efficiency Si-based multijunction solar cells. A multiscale theoretical approach is used here to avoid expensive experiments, and to expedite the process to reduce the target experimental parameter space. First, the atomistic tight-binding approximation is used to calculate the band structures of dilute nitrides, which are the foundation of further investigation of their photovoltaic-relevant material properties. With the calculated band structures, a fullband Monte Carlo simulator is used to understand the physics of carrier transport in GaNP(As), although more trials with different physical models are still needed to match experimental results. The band structures are also used to calculate the optical properties of GaNP(As). Currently, only direct transitions are included given that GaNP(As) are direct-bandgap materials. Using these calculated optical properties of GaNP(As), preliminary simulations with Silvaco ATLAS [53] were performed on three-terminal two-junction (3T2J) GaNP(As)/Si tandem solar cells. Realistic material parameters are used for the design of the 3T2J tandem structures. More realistic modeling of GaNP(As)/Si should

also include the physics at the GaP/Si heterovalent interface. Hence, some preliminary simulations of GaP/Si interfaces are performed as well.

Chapter 2

CALCULATION OF THE ELECTRONIC STRUCTURE OF DILUTE-NITRIDE GaNPAs

2.1 Introduction

The electronic band structure of a material describes the possible energy states that an electron can occupy, which dictates the electrical and optical properties of the material. Knowing the electronic band structure of GaNPAs alloys lays the foundation for further understanding of their properties that are crucial to the performance of photovoltaic devices.

Take the near bandgap optical properties of GaAs and of GaP as examples. Figure 2.1 shows the electronic band structure of GaAs and of GaP at room temperature. The conduction band minimum (CBM) and valence band maximum (VBM) of GaAs occur at the same wave vector, Γ, indicating GaAs is a direct-bandgap material. This means an electron occupying an energy state near the VBM of GaAs can absorb a photon with an energy of the bandgap, and make a direct transition to an unoccupied state near the CBM. However, the VBM and CBM of GaP occur at different wave vectors, making direct optical transitions between the VBM and CBM impossible, since photons have extremely small momentums and momentum are conserved during the transitions. Thus, GaP requires higher order processes involving phonons and photons to conserve both the energy and momentum during band-to-band optical transitions (indirect transitions). This means that GaP does not strongly absorb light near the bandgap, the energy difference between the CBM and the VBM, while GaAs does. As shown in Figure 2.2, the absorption coefficient of GaAs is much higher than that of GaP near their corresponding bandgap.

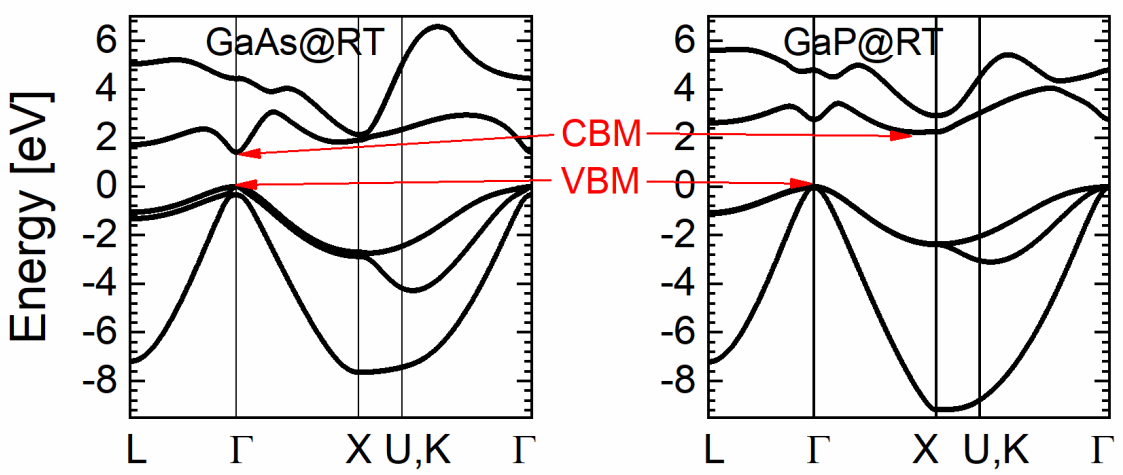

Figure 2.1 The electronic band structure of GaAs (left) and of GaP (right) calculated in this work, along the high-symmetry wave vector lines in the reciprocal space. The red arrows indicate the conduction band minimum (CBM) and valence band maximum (VBM).

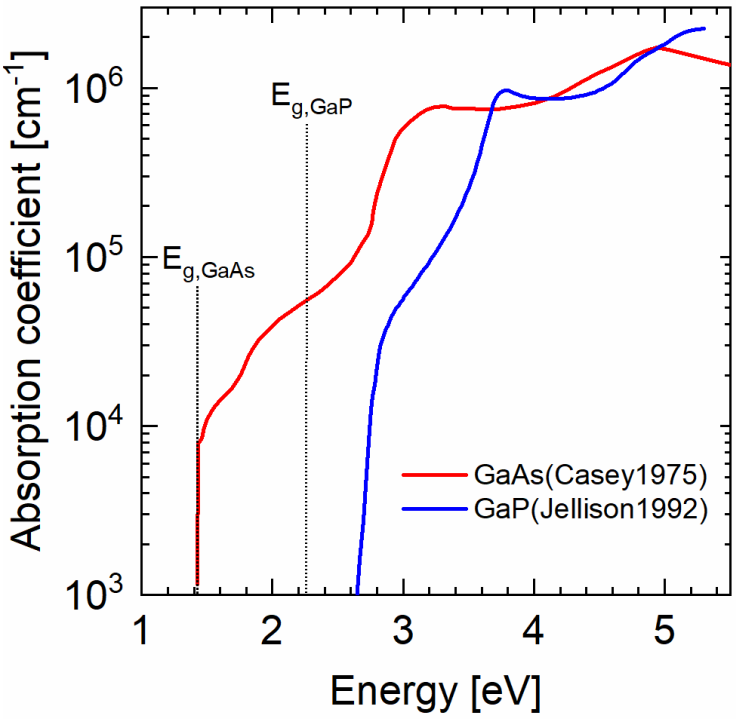

Figure 2.2 Experimentally measured [54], [55] absorption coefficients of GaAs and GaP.

2.2 The Band Anti-crossing (BAC) Model

The concept of BAC originates from the insight from a hydrostatic pressure study. Shan *et al*. applied hydrostatic pressure to $Ga_{0.92}In_{0.08}As$ and $Ga_{0.92}In_{0.08}N_xAs_{1-x}$ and measured their fundamental bandgaps with photomodulated transmission [43]. The bandgap of $Ga_{0.92}In_{0.08}As$ increases linearly with increasing hydrostatic pressure. However, with nitrogen added, the bandgap increase slows down as the pressure goes higher, and the bandgaps tend to saturate. For the two $Ga_{0.92}In_{0.08}N_xAs_{1-x}$ alloys with lower N content, the saturation energy is near 1.72 eV, which is close to the well-known N impurity level in GaAs. As the N fraction goes higher, not only does the bandgap becomes lower, but the slope of the bandgap increase with pressure also decreases. These suggest that the extended lowest conduction band states are affected by the localized N states.

They then proposed the band anticrossing model which states that the localized N states strongly interact with the energetically-close lowest conduction band states, and they mix together and split into two bands. It can be written as a perturbation in the form of an eigenvalue problem [43]:

$$\begin{vmatrix} E - E_M & V_{MN}(x) \\ V_{MN}(x) & E - E_N \end{vmatrix} = 0, \tag{2.1}$$

where E_M is the energy of the matrix material conduction bandedge, E_N is the energy of nitrogen level, and $V_{MN}(x)$ is the interaction between the bandedge states and the N states, which increases with N fraction x. The solution to Equation 2.1 is

$$E_{\pm} = \frac{1}{2}\left\{E_N + E_M \pm [(E_N - E_M)^2 + 4V_{MN}^2(x)]^{1/2}\right\}. \tag{2.2}$$

Not only does this model agree with the fact that the fundamental bandgap decreases as x increases, it also predicts the existence of an upper band which is difficult to detect. They were able to detect this transition with photomodulated reflectance. This model has been successfully used to reproduce the measured E_- and E_+ transitions of GaNP at 295 K, with $E_N = 2.15$ eV and $V_{MN} = 3.05\sqrt{x}$ eV [44].

However, the coupling strength between the N states and the conduction bandedge states is different for different wave vectors. To calculate the electronic structure throughout the first Brillouin zone, one needs to obtain the dispersion of V_{MN}, which is not trivial. Shtinkov *et al.* [56] used a tight-binding model (further discussed in the next sections) to calculate the electronic structure of GaNAs, and achieved good agreement with experimental observation not only near zone center, but also near L and X.

2.3 The Tight-binding Approximation

In general, the main problem in electronic band structure calculation is solving the Schrödinger equation, which can be written in the general form as

$$\mathbf{H}|\mathbf{\Psi}\rangle = E|\mathbf{\Psi}\rangle, \tag{2.3}$$

where $\mathbf{H}$ is the Hamiltonian, $\mathbf{\Psi}$ is the electron wave function, and E is the energy. This can be viewed as an eigenvalue problem. Finding solutions to Equation 2.3 is not trivial. With limited amount of time and computational resources, it is usually done with approximations.

The tight-binding (TB) approximation is a relatively fast and accurate approach for electronic structure calculation. It was first proposed by Bloch [57] and later simplified and

parameterized by Slater and Koster [58]. It views the electrons as tightly bound to the atomic cores, and the electron wavefunctions are approximated as linear combinations of orthogonalized atomic orbitals,

$$\begin{aligned}\mathbf{\Psi}_{\mathbf{k}}^{\alpha}(\mathbf{r}) &= \frac{1}{N^{1/2}}\sum_{a}\exp\left(i\mathbf{k}\cdot\mathbf{R}_a\right)\phi^{\alpha}\left(\mathbf{r}-\mathbf{R}_a\right) \\ &= \frac{1}{N^{1/2}}\sum_{a}\exp\left(i\mathbf{k}\cdot\mathbf{R}_a\right)\psi^{\alpha}\left(\mathbf{r}-\mathbf{R}_a\right)\end{aligned} \tag{2.4}$$

where $\mathbf{k}$ is the wave vector, $\mathbf{r}$ is a vector in real space, a is the index of atoms, $\mathbf{R}_a$ is the real space position of atom a, α is the index of atomic orbitals, ϕ^{α} is the true atomic orbital, and N is the number of unit cells in the volume. The true atomic orbitals are not orthogonal. They are orthogonalized as Löwdin [59] orbitals, ψ^{α}, while preserving the symmetries of the orbitals. With Equation 2.4, the Hamiltonian matrix element is given by

$$\begin{aligned}H_{ab}^{\alpha\beta} &= \left\langle \mathbf{\Psi}_{\mathbf{k}}^{\alpha}\middle|\mathbf{H}\middle|\mathbf{\Psi}_{\mathbf{k}}^{\beta}\right\rangle \\ &= \frac{1}{N}\sum_{a,b}\exp\left[i\mathbf{k}\cdot\left(\mathbf{R}_b-\mathbf{R}_a\right)\right]\times \\ &\qquad \left\langle\psi_a^{\alpha}\left(\mathbf{r}-\mathbf{R}_a\right)\middle|\mathbf{H}\middle|\psi_b^{\beta}\left(\mathbf{r}-\mathbf{R}_b\right)\right\rangle \\ &= \sum_{b}\exp\left[i\mathbf{k}\cdot\left(\mathbf{R}_b-\mathbf{R}_a\right)\right]\times \\ &\qquad \left\langle\psi_a^{\alpha}\left(\mathbf{r}-\mathbf{R}_a\right)\middle|\mathbf{H}\middle|\psi_b^{\beta}\left(\mathbf{r}-\mathbf{R}_b\right)\right\rangle \\ &= \sum_{b}\exp\left[i\mathbf{k}\cdot\left(\mathbf{R}_b-\mathbf{R}_a\right)\right]\sigma_{ab}^{\alpha\beta}\end{aligned} \tag{2.5}$$

where a and b are the indices of atoms, and α and β are the indices of atomic orbitals. The third step in Equation 2.5 takes into account that summing over either of the indices of atoms cancels $1/N$. The last step shows that the TB method treats the difficult-to-calculate

integrals of the atomic orbitals as disposable parameters, $\sigma_{ab}^{\alpha\beta}$, which are obtained by fitting to more accurate calculations or experimental data.

Including more orbitals into the tight-binding scheme increases the level of accuracy of the approximated electronic structure on the one hand, but raises the computational complexity on the other. Within the Slater-Koster framework, Chadi and Cohen [60], [61] showed that an sp^3 basis (s, p_x, p_y, p_z) is usually sufficient to accurately describe the valance bands of diamond and zinc-blende crystals. Later, Vogl, Hjalmarson, and Dow [62] added an excited s orbital (s^*) to the sp^3 basis to allow the adjustment of the energies of the lowest conduction band near the X and L symmetry points. Jancu et al. [63] argued that the inclusion of all five d orbitals is necessary to correctly describe the pressure dependence of the energy of X_{6c} (the lowest conduction band state near X), and demonstrated the success of a nearest-neighbor $sp^3d^5s^*$ model to reproduced the main features of the valence bands and the lowest two conduction bands of group-IV and III-V materials. Since then, the $sp^3d^5s^*$ tight-binding model has been widely used for cubic crystal semiconductors.

2.4 Optimizing the $sp^3d^5s^*$ Tight-binding Parametrization

The use of the Slater-Koster TB method requires the disposable parameters, the on-site energies and the overlap integrals, to be fit first. Available $sp^3d^5s^*$ parametrizations [63], [64] are typically fit to the relevant band edge energies and effective masses, which is good for electrical calculations. For photovoltaic applications, accurate information of the optical properties of the materials is important. Here we fit the $sp^3d^5s^*$ model to match

not only the typical band edge energies and effective masses, but also critical optical transition energies.

For a III-V material, the $sp^3d^5s^*$ basis set comprises 31 independent parameters, which include 8 on-site energies, 21 two-center hopping integrals, and 2 spin-orbit interaction energies [63]. Fitting a set of 31 parameters to match the relevant band energies, effective masses, and optical transition energies, is a non-trivial global optimization problem. A genetic algorithm mimics the natural selection process to obtain high-quality solutions to an optimization problem. Klimeck *et al*. [65] used a genetic algorithm to obtain 3 sets of sp^3s^* parameters for Si, with a comparison to those from Vogl, Hjalmarson, and Dow's work [62]. Here, to solve the multi-dimensional nonlinear global optimization problem, we pair the in-house TB solver with an open-source parallel genetic algorithm library, PGAPack [66], developed by Argonne National Laboratory.

At the starting point, the 31 parameters are randomly initialized as "genes" within reasonable parameter boundaries and are then packaged into a "chromosome". According to the specified population size, multiple chromosomes are randomly created to form the initial generation. During each generation, each chromosome is evaluated by calling the $sp^3d^5s^*$ TB solver, generating relevant band parameters, and comparing them to the target values with specific weights. The "chromosome" that generates band parameters closet to the target values is given the highest rank, and so on. A selected number of the highest-ranked chromosomes will survive the generation, and give birth to the next generation through crossover, and mutation. Thus, the next generation goes through the same random process. All generations have the same population size. One can assume a good solution

has been reached when a particular number of generations have passed, when the last few generations are extremely similar, or when almost all the chromosomes are the same in the generation. Factors that may change the fit of the solution include (a) the size of the population, (b) ending criteria, (c) weights of the target, (d) survival rate, (e) probabilities of crossover and mutation, and (f) the seed value for the random number generator. For the same number of evaluations, which equals to the product of population size and number of iterations, our experience is that choosing a larger population size, with respect to a larger number of iterations, usually gives better results. The fitting procedure is summarized in Figure 2.3.

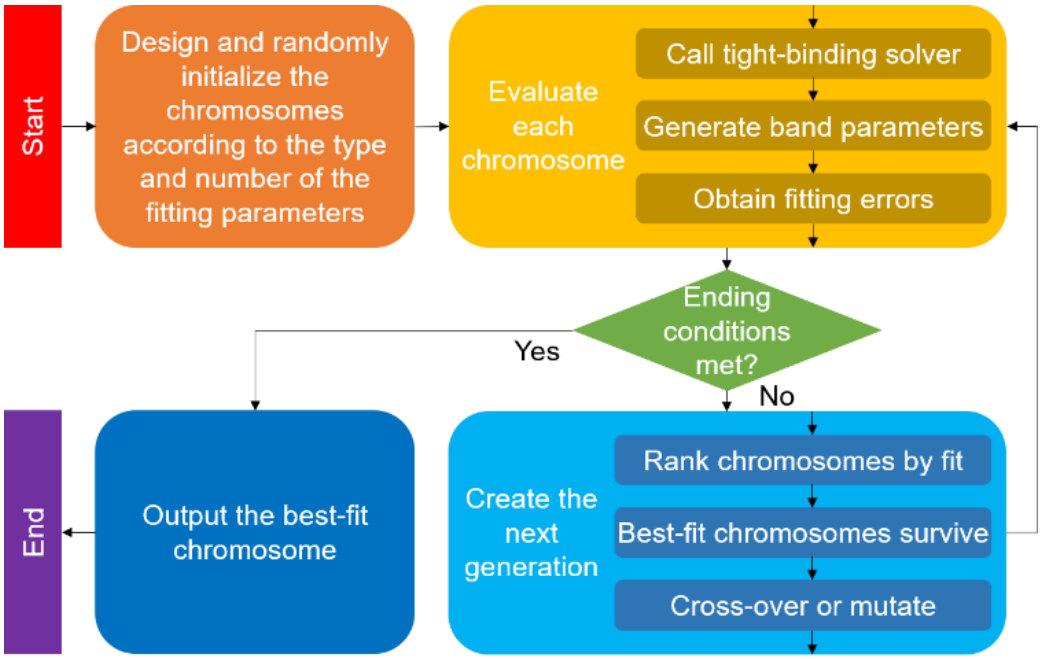

Figure 2.3 Flow chart of the fitting procedure for the tight-binding parameters.

We carried out the optimization procedure for GaP and GaAs to fit experimental band energies for the conduction band bottom at Γ, *L*, *X*, the valence band split-off energy, and

the effective masses at these points, as well as optical transition energies, E_1, $E_1 + \Delta_1$, E_0', and E_2. These optical transitions are marked in the electronic structure of GaAs in Figure 2.4. For the effective masses that have relatively large uncertainties, we put less weight on fitting these values. After the fitting procedure above, we obtained the Slater-Koster-type $sp^3d^5s^*$ parameters for GaP and GaAs, which are listed in Table 2.1.

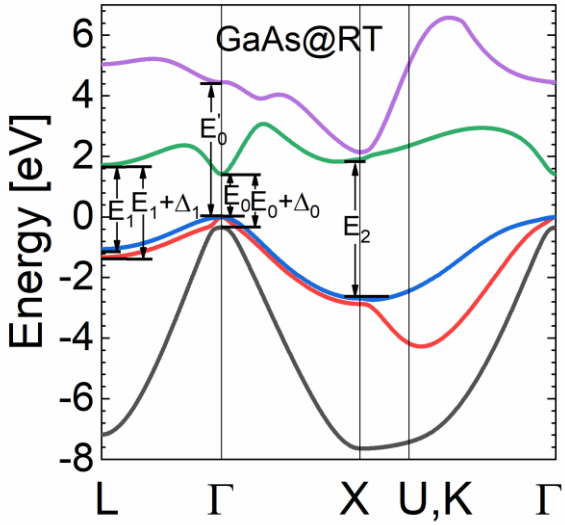

Figure 2.4 Optical transition energies E_0, $E_0 + \Delta_0$, E_1, $E_1 + \Delta_1$, E_0', and E_2 for GaAs at room temperature.

Table 2.1 Optimized Slater-Koster-type nearest-neighbor $sp^3d^5s^*$ parameters for GaP and GaAs at room temperature. The lattice constants are in units of Å, and all other parameters are in units of eV. The parameter notation is consistent with that of Jancu *et al.*'s [63].

Parameters	GaP	GaAs
a_0	5.4508	5.6532
E_s^c	-0.71823	-0.36374
E_p^c	6.21668	8.13245
E_d^c	12.85561	20.62765
$E_{s^*}^c$	19.63221	14.12705

E_s^a	-6.07142	-9.66064
E_p^a	2.07966	2.48628
E_d^a	15.03221	21.71325
$E_{s^*}^a$	20.26761	15.18635
$ss\sigma$	-1.85072	-1.85238
$s_c p_a \sigma$	3.37883	2.82860
$s_c d_a \sigma$	-2.38353	-2.33514
$s_c s_a^* \sigma$	-1.16664	-1.48694
$s_a p_c \sigma$	2.18465	2.50423
$s_a d_c \sigma$	-3.11886	-1.24536
$s_a s_c^* \sigma$	-0.66599	-0.59257
$pp\sigma$	3.62258	4.04989
$pp\pi$	-0.99926	-1.60088
$p_c d_a \sigma$	-1.86188	-1.89807
$p_c d_a \pi$	1.96330	3.82055
$p_c s_a^* \sigma$	2.49661	1.89681
$p_a d_c \sigma$	-0.89955	-2.30529
$p_a d_c \pi$	1.25412	2.36166
$p_a s_c^* \sigma$	3.71479	3.16348
$dd\sigma$	-0.87592	-3.07285
$dd\pi$	2.12065	4.76324
$dd\delta$	-1.51045	-1.34699
$d_c s_a^* \sigma$	-0.07141	-0.34281
$d_a s_c^* \sigma$	-0.25448	-0.29833
$s^* s^* \sigma$	-4.02230	-2.16846
$\Delta_c/3$	0.00002	0.00551
$\Delta_a/3$	0.01967	0.13714

Taking the $sp^3d^5s^*$ parameters in Table 2.1, the TB solver generated the electronic structure of GaAs and GaP at room temperature, which are plotted along high-symmetry lines of the first Brillouin zones of these three face-centered cubic lattices in Figure 2.5. These plots have been shifted so that their valence band maxima are all at 0 eV. Given the availability of literature reports, the electronic structure of GaAs generated from our optimized $sp^3d^5s^*$ parameters is compared to that from quasiparticle self-consistent GW (QSGW) theory [67], as shown in Figure 2.5. The QSGW calculation was carried out for low temperature, and we shifted their conduction bands -0.1 eV to approximate the temperature effect. The QSGW calculation does not account for spin-orbit coupling, and we shifted the second top-most valence band -0.34 eV for comparison. Except for the systematically overestimated gaps of the QSGW structure [67], the two have general agreements in shape, especially for the lowest conduction band between *L* and Γ and for the split-off valence band.

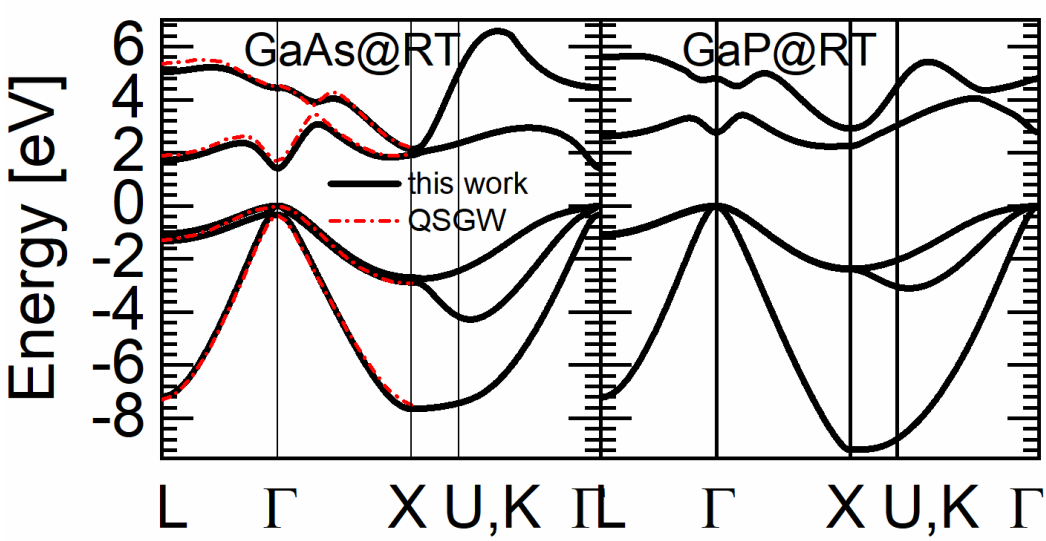

Figure 2.5 Energy dispersion along high-symmetry lines for GaAs and GaP at room temperature (black solid lines). The energy dispersion of GaAs by this work is compared to that from a quasiparticle self-consistent GW calculation [67] (red dash-dot lines).

We then compare the relevant band energies, effective masses, and optical transition energies from the present models with those from other sources in Tables 2.2 and 2.3. The first four columns of these tables are values from experiments and two notable compilations, and they are used as a reference to evaluate the calculated results. All the TB calculations included in the tables are based on the nearest-neighbor $sp^3d^5s^*$ model. For GaAs, TB can generally generate conduction band energies much closer to experimental values than first-principles calculations, e.g. the QSGW calculation mentioned above, and a local-density approximation (LDA) with self-energy corrections [68], given the empirical nature of the TB calculations. Our TB results have similar effective masses and conduction band energies as two previous TB works [69], [70], but have improved optical transition energies, as the latter is one of the main focuses of our fitting procedures. For GaP, the available calculations of band parameters are not as abundant as those for GaAs. We used a TB

parameter set published for low temperature [63], and applied hydrostatic tensile strain, from lattice constant $a(0K)$ to $a(300K)$, for comparison. Our TB results show good agreement with the reference, especially for the conduction band energies, E_1 and E_2, though the split-off energy is overestimated and the hole effective masses have larger errors than those from the two previous TB works. Overall, our optimized TB parameter sets for GaAs and GaP give reasonably good agreement to commonly referred relevant band values, including optical transition energies.

Table 2.2 Comparison of room-temperature band parameters of GaAs from experiment and different calculations. E_Γ, E_X, and E_L are energies w.r.t. the top of the valence band, and other energies are gap energies. All energies are in units of eV, and relative effective masses are unitless.

Parameter	*Exp. A*[a]	*Exp. B*[b]	*Cmp. A*[c]	*Cmp. B*[d]	*TB I*[e]	*TB II*[f]	*LDA*[g]	*QSGW*[h]	*This work*
E_Γ		1.42	1.42	1.43	1.4159	1.416	1.21	1.67	1.4188
E_X			1.90	1.91	1.9015	1.910		1.95	1.9099
E_L			1.71	1.72	1.7012	1.708		1.89	1.7207
E_0'		4.44		~4.54				4.53	4.45
Δ_0		0.37	0.34	0.341	0.3265	0.367			0.34
E_1	2.91	2.91		~2.9	2.76	3.28	2.90	3.18	2.89
Δ_1	0.18	0.22		0.222	0.27	0.31			0.24
E_2	4.78	4.96		~5.2	4.34	5.47	~4.4	4.85	4.81
$m^*_{e,\Gamma}$			0.067	0.067	0.0657	0.067		0.077	0.067
$m^*_{e,Xl}$			1.3	1.3	1.8808	1.480			0.36
$m^*_{e,Xt}$			0.23	0.23	0.1753	0.204			0.16
$m^*_{e,Ll}$			1.9	1.9	1.7275	1.446			1.65
$m^*_{e,Lt}$			0.075	0.075	0.0967	0.136			0.36
$m^*_{hh,[100]}$			0.35	0.33	0.3769	0.337			0.328

$m^*_{hh,[110]}$	0.64	0.58	0.6566	0.619	0.600
$m^*_{hh,[111]}$	0.89	0.78	0.8391	0.813	0.786
$m^*_{lh,[100]}$	0.090	0.090	0.0825	0.083	0.082
$m^*_{lh,[110]}$	0.081	0.080	0.0755	0.074	0.074
$m^*_{lh,[111]}$	0.078	0.077	0.0736	0.072	0.055
m^*_{so}	0.172	0.165	0.1624	0.160	0.156

Table 2.3 Comparison of room-temperature band parameters of GaP from experiment and different calculations. E_Γ, E_X, and E_L are energies w.r.t. the top of the valence band, and other energies are gap energies. All energies are in units of eV, and relative effective masses are unitless.

Parameter	*Exp. A*[a]	*Exp. B*[b]	*Cmp. A*[c]	*Cmp. B*[d]	*TB I*[e]	*TB II*[f]	*LDA*[g]	*This work*
E_Γ	2.76		2.92	2.76	2.85	2.79	2.05	2.7662
E_X			2.27	2.26	2.36	2.31	1.80	2.2536
E_L			2.64	2.63	2.55	2.53		2.6249
E_0'	4.78	4.8		4.74	4.46	4.62		4.79
Δ_0			0.08	0.085	0.080	0.090		0.041
E_1	3.7	3.73		3.71	3.64	3.92	3.52	3.70
Δ_1	< 0.1			0.055	0.1	0.09		0.035
E_2	5.05	5.08		5.28	5.40	5.71	~4.65	5.10
$m^*_{e,\Gamma}$			0.13	0.114	0.127	0.13		0.114
$m^*_{e,Xl}$			2.0	6.9	15.3	0.82		3.08
$m^*_{e,Xt}$			0.253	0.252	0.26	0.21		0.31
$m^*_{e,Ll}$			1.2	1.18	1.77	1.59		3.42
$m^*_{e,Lt}$			0.15	0.15	0.39	0.42		0.58
$m^*_{hh,[100]}$				0.34	0.35	0.38		0.488
$m^*_{hh,[110]}$				0.53	0.72	0.71		0.841

$m^*_{hh,[111]}$		0.66	0.98	0.91	1.060
$m^*_{lh,[100]}$		0.20	0.15	0.16	0.124
$m^*_{lh,[110]}$		0.16	0.12	0.13	0.112
$m^*_{lh,[111]}$		0.15	0.09	0.10	0.084
m^*_{so}	0.25	0.34	0.22	0.46	0.200

2.5 A Simple Virtual Crystal Approximation with the Tight-binding Scheme

A general approach to obtain the TB parameters for an alloy is to interpolate from the sets of parameters for the corresponding pure materials, and treat the alloy as a pseudo-pure material, based on the virtual crystal approximation (VCA). However, the variation of the bandgaps of dilute nitrides with respect to composition is highly nonlinear between those of the pure materials, rendering a simple VCA approach inaccurate in describing these relations. Figure 2.6 shows the bandgaps of InGaAs and GaNP as functions of their compositions. The TB calculations based on the VCA were done by linear interpolation from their parent Hamiltonians. The results show that the VCA does not perform well when bowing is significant. Although there are more complicated VCA techniques, that have better bowing performance by introducing (e.g. as in Ref. [71]) 17 extra fitting parameters for each parent material, the complication counteracts the idea of the VCA being a simple and fast approximation, and they have not been proven to work well on dilute nitrides, which have extremely large bowing when the N content is smaller than about 0.5% and smaller bowing at higher N fractions.

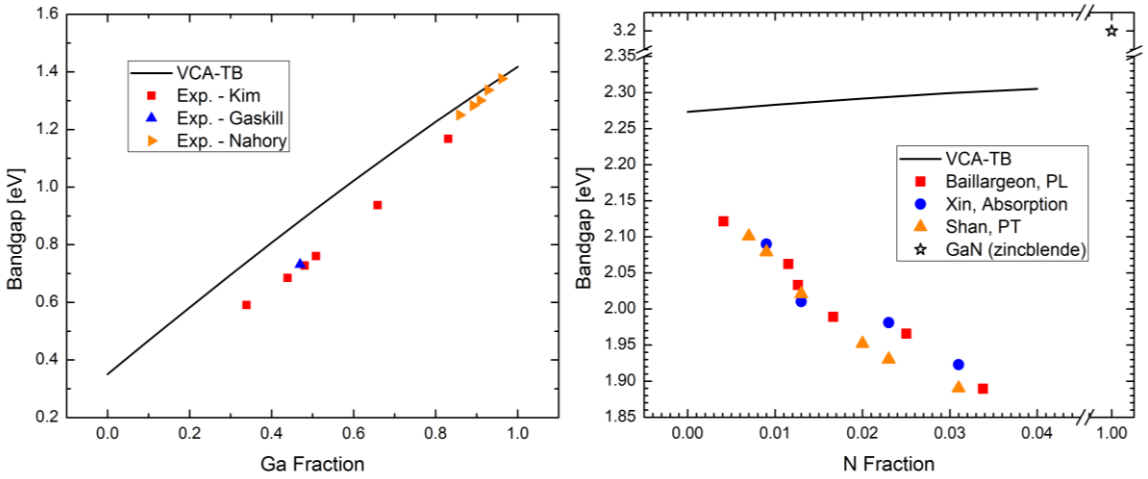

Figure 2.6 Bandgaps vs. compositions measured by different groups [29], [72]–[76] (filled symbols) and calculated by TB with parameters obtained with VCA at 300 K for (a) InGaAs and (b) GaNP. The bandgap of zincblende GaN is also included in the plot on the right as a reference (open star).

2.6 The $sp^3d^5s^*s_N$ Tight-binding Model for Dilute-Nitride GaNPAs

Shtinkov *et al*. modified the $sp^3d^5s^*$ TB model into a $sp^3d^5s^*s_N$ model to calculate the band structure of dilute-nitride (dilute-N) GaNAs alloys [56]. On top of the $sp^3d^5s^*$, the $sp^3d^5s^*s_N$ model adds an N-related s orbital to anion sites, s_N, and a two-center integral, $s_c s_N \sigma$, for the coupling between the cation s orbital and the new s_N orbital, resembling the E_N and V_{MN} terms in the BAC model, respectively. The model assumes the interaction between s_N and all other orbitals is negligible, given that the N states affect only the lowest conduction bands.

Here, the $sp^3d^5s^*s_N$ model is used in our electronic structure calculations for dilute-N GaNPAs alloys. For the construction of the $sp^3d^5s^*s_N$ Hamiltonian for the quaternary alloy, we first adopt the $sp^3d^5s^*$ parametrization for GaP and GaAs tabulated in Section

2.5 [77], and then determine the E_{s_N} and $s_c s_N \sigma$ parameters for GaNP and GaNAs, respectively, based on the fit to experimental bandgap data. Table 2.4 shows the two sets of E_{s_N} and $s_c s_N \sigma$ parameters we use in the calculation. Finally, the GaNPAs $sp^3d^5s^*s_N$ Hamiltonian is obtained via a linear interpolation of the GaNP and GaNAs $sp^3d^5s^*s_N$ Hamiltonians. For bulk alloy calculations, no strain is considered.

Table 2.4 The on-site energies, E_{s_N} and the coupling terms, $s_c s_N \sigma$ used in the $sp^3d^5s^*s_N$ calculations for GaNP and GaNAs. Units are in eV. (Adapted from [77].)

	E_{s_N}	$s_c s_N \sigma$
GaN_xP_{1-x}	2.18	$-1.2\sqrt{x}$
GaN_xAs_{1-x}	1.65	$-0.93\sqrt{x}$

Figure 2.7 plots the calculated band structure of GaAs and $GaN_{0.035}As_{0.965}$ at 300 K. The colors highlight that the lowest conduction band (CB) of GaAs splits into two CBs (E_- and E_+) of $GaN_{0.035}As_{0.965}$. As shown in Figure 2.8, with increasing N mole fraction, the E_- band shifts down in energy while the E_+ band rises up, and the fundamental bandgap decreases.

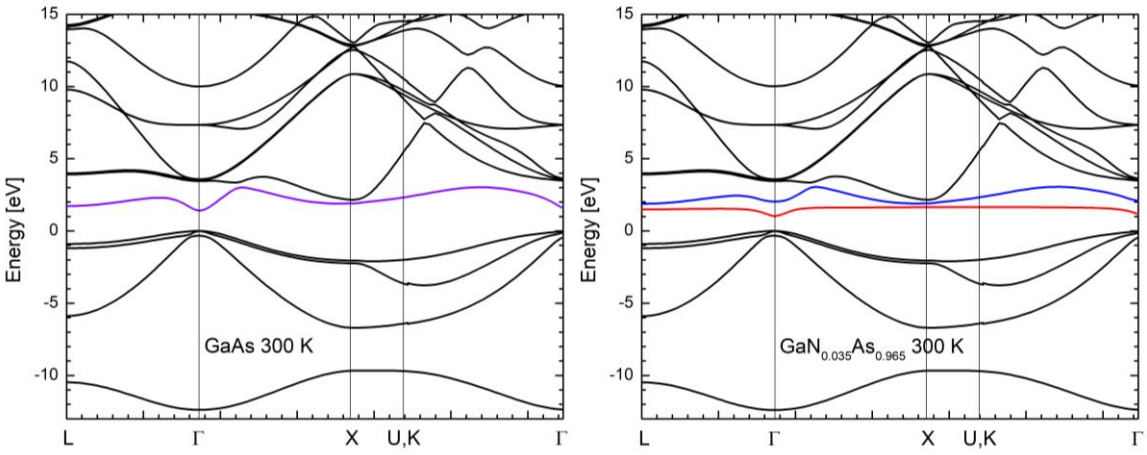

Figure 2.7 Electronic structure of GaAs (left) and $GaN_{0.035}As_{0.965}$ (right) at 300 K calculated with the $sp^3d^5s^*s_N$ model along high-symmetry lines. The lowest conduction band (CB) of GaAs and the lowest two CBs of $GaN_{0.035}As_{0.965}$ are highlighted with colors.

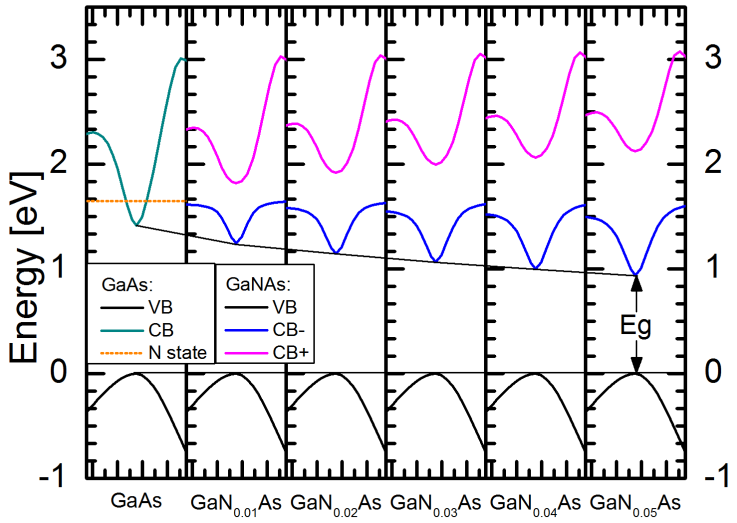

Figure 2.8 Electronic structure of GaAs and GaN_xAs_{1-x} along L-Γ-X calculated with the $sp^3d^5s^*s_N$ model.

Likewise, bandgaps can be extracted from the calculated band structure of GaN_xP_{1-x}. Figure 2.9 compares the bandgap values of GaN_xP_{1-x} calculated from the $sp^3d^5s^*s_N$ model with experimental data and other theoretical calculations. The dotted line corresponding to

the TB calculations with the simple VCA scheme is the same as explained in Figure 2.6. The large supercell calculations with pseudopotentials provide the Γ valley minimums and X valley minimums [26]. Their values are down-shifted to reflect the temperature difference for this figure. They cross each other at about $x = 0.032$, indicating the transformation from indirect bandgap material to direct bandgap material, which disagrees with the experimental determination of the bandgap being direct at even much lower N concentrations [76]. The TB results with the $sp^3d^5s^*s_N$ model agree well with the experimental data.

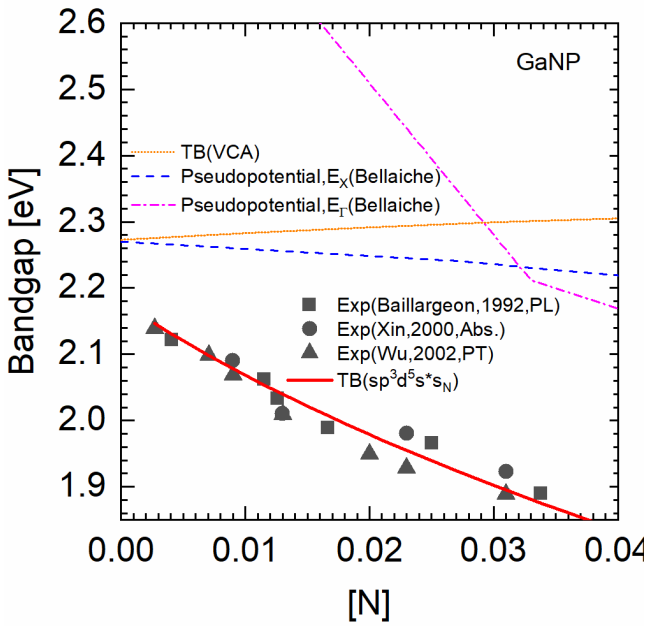

Figure 2.9 The lines show the calculated bandgaps of GaN_xP_{1-x} at 300 K with the TB $sp^3d^5s^*s_N$ model (solid), TB with a simple VCA scheme (dotted), pseudopotential supercell method (dashed) [26], and the filled symbols are the experimental data by different groups [29], [75], [76].

To calculate the electronic structure of $GaN_xP_yAs_{(1-x-y)}$, we use the $sp^3d^5s^*s_N$ parametrization for $GaN_xP_{(1-x)}$ and for $GaN_xAs_{(1-x)}$ to obtain their TB Hamiltonians, and

then linearly interpolate these parent Hamiltonians based on the P/As ratio to obtain the TB Hamiltonian for $GaN_xP_yAs_{(1-x-y)}$.

Relevant to Si-based tandems, $GaN_{0.040}P_{0.872}As_{0.088}$ is lattice-matched to Si. It can be formed by adding N into $GaP_{0.91}As_{0.09}$. Figure 2.10 shows the calculated electronic structure of $GaP_{0.91}As_{0.09}$ and $GaN_{0.040}P_{0.872}As_{0.088}$. $GaP_{0.91}As_{0.09}$ is an indirect-bandgap material with the conduction band minimum located near X. With the incorporation of N, the new conduction band minimum is at the zone center (Γ), leading to a direct bandgap. The N effect is strongest at Γ, becomes weaker towards L, and almost diminishes towards X; The higher conduction bands and the valence bands are mostly unchanged.

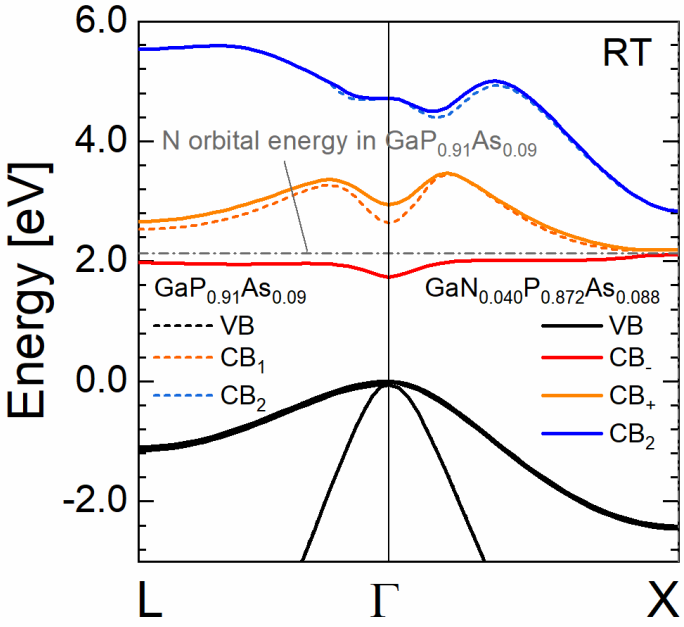

Figure 2.10 The band structure calculated from the $sp^3d^5s^*s_N$ model for $GaN_{0.040}P_{0.872}As_{0.088}$ (solid lines) and from the $sp^3d^5s^*$ model for $GaP_{0.91}As_{0.09}$ (dashed lines). The highest three valence bands (black) for the two materials overlap with each other. The N orbital energy in $GaP_{0.91}As_{0.09}$ is indicated by the dashed-dotted line.

As another demonstration, we extracted the bandgaps of GaNAs, GaNP, and GaNPAs lattice-matched to Si for less than 5.0% N and plotted them in Figure 2.11, although the values for GaNP with less than 3.8% N have already been shown in Figure 2.9. The calculations suggest that the band gap of GaNPAs lattice-matched to Si ranges from 1.97 eV to 1.63 eV for [N]=0.021 to 0.050, good for making Si-based independently connected tandems.

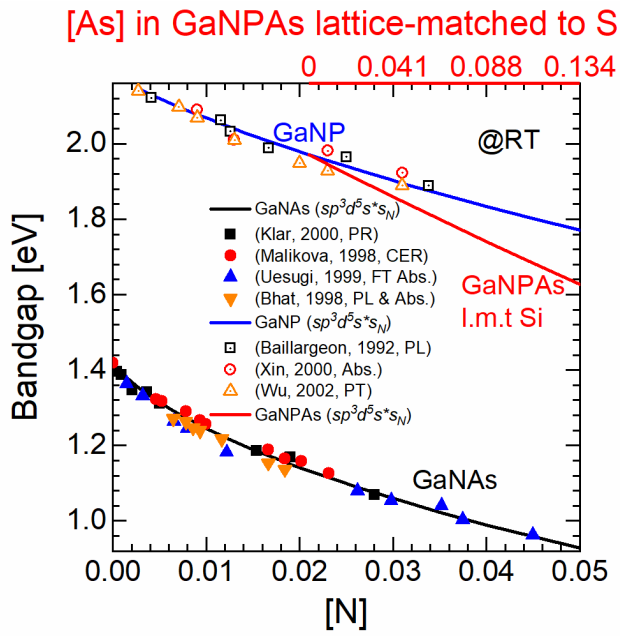

Figure 2.11 Calculated (solid lines) and reported experimental [28], [29], [42], [75], [78]–[80] (symbols) bandgaps of dilute-N GaNP and GaNAs at room temperature (RT). The bandgaps of GaNPAs lattice-matched to Si are plotted from calculation (red solid line). [As] = 0.000 is aligned with [N] = 0.021, that is $GaN_{0.021}P_{0.979}$ is lattice-matched to Si. For [N] < 0.021, there is no GaNP(As) lattice-matched to Si, assuming Vegard's law [48], [81]. Calculations carried out here use the $sp^3d^5s^*s_N$ model.

Chapter 3

CALCULATION OF OPTICAL PROPERTIES OF DILUTE-NITRIDE GaNPAs

3.1 Introduction

As mentioned in previous chapters, dilute-nitride (dilute-N) GaNPAs alloys can be grown lattice-matched to Si while having a large bandgap range. These features combined have brought practical interest to these alloys for applications such as optoelectronic integrated circuits (OEIC) [82]–[84] and high efficiency photovoltaic cells [22], [85].

It is desirable to be able to generate optical properties over a large energy range of dilute-N GaNPAs at arbitrary compositions, as this enables the evaluation of the alloy for different application needs. There have been reports of experimentally measured absorption in only a small sample of the entire dilute-N GaNPAs alloy system [45], [47], [85]–[87], and most of these data are near bandgap only. Theoretical models have been used to calculate the electronic structure of GaNPAs alloys [85], [88], [89]. However, to the best of the author's knowledge, there are lack of publications on the calculation of the optical properties of GaNPAs alloys, such as their refractive indices, absorption coefficients, or dielectric functions, etc. Here we demonstrate a computationally economical atomistic approach to calculate the dielectric functions and absorption coefficients of GaNPAs alloys.

3.2 Method

We first construct the $sp^3d^5s^*s_N$ tight-binding Hamiltonian for dilute-N GaNPAs (as discussed in Section 2.7), and calculate the optical properties as follows.

The probability per unit time for a transition from an initial state $|i\rangle$ to a final state $|f\rangle$ induced by a perturbation of the form $\mathcal{L}e^{\mp i\omega t}$ can be written as

$$\mathcal{P}_{i\to f} = \frac{2\pi}{\hbar}|\langle f|\mathcal{L}|i\rangle|^2\delta\big(E_f - E_i \mp \hbar\omega\big), \tag{3.1}$$

where E_i and E_f are the energies of the initial and final states. As a first-order approximation, we consider only direct transitions. Then the imaginary part of the complex dielectric function $\varepsilon(\omega) = \varepsilon_1(\omega) + i\varepsilon_2(\omega)$ is given by [90]

$$\varepsilon_2(\omega) = \frac{1}{4\pi\epsilon_0}\left(\frac{2\pi e}{m\omega}\right)^2 \sum_{\boldsymbol{k}} |P_{cv}|^2\delta(E_c(\boldsymbol{k}) - E_v(\boldsymbol{k}) - \hbar\omega), \tag{3.2}$$

where ω is the angular frequency of the light, $\boldsymbol{k}$ is the wave vector in reciprocal space, $P_{cv} = \langle c|\hat{\boldsymbol{e}}\cdot\boldsymbol{p}|v\rangle$ is the momentum matrix element, $\hat{\boldsymbol{e}}$ is a unit vector parallel to the electric field of the electromagnetic wave, and $\boldsymbol{p}$ is the momentum operator. Indirect transitions are ignored here. The momentum operator is obtained from the tight-binding Hamiltonian H as [91]

$$\boldsymbol{p}(\boldsymbol{k}) = \frac{m_0}{\hbar}\nabla_{\boldsymbol{k}}H(\boldsymbol{k}), \tag{3.3}$$

where $H(\boldsymbol{k})$ is the TB Hamiltonian. The TB Hamiltonian matrix elements are given by [58]

$$H_{ij}^{mn} = \sum_{\boldsymbol{R}_j} e^{i\boldsymbol{k}\cdot(\boldsymbol{R}_j - \boldsymbol{R}_i)} \int \psi_n^*(\boldsymbol{r} - \boldsymbol{R}_i) H \psi_m\big(\boldsymbol{r} - \boldsymbol{R}_j\big) d^3\boldsymbol{r}\,, \tag{3.4}$$

where $\boldsymbol{R}_i$ and $\boldsymbol{R}_j$ are the positions of the basis atoms i and j on which the orbitals ψ_n and ψ_m are located, respectively. The integral in Eq. (3.4) can be expressed as a sum of on-site energies ($j = i, m = n$) and Slater-Koster-type hopping integrals ($j \neq i$). The exponential

factors of the on-site energies become unity, thus Eq. (3.3) is left with a derivative of the hopping integral parts. Since ε is a linear response function, once we obtain ε_2, ε_1 is given by the Kramers-Kronig relation

$$\varepsilon_1(\omega) = 1 + \frac{2}{\pi}\mathcal{P}\int_0^\infty \frac{\omega'\varepsilon_2(\omega')d\omega'}{\omega'^2 - \omega^2}, \tag{3.5}$$

where $\mathcal{P}$ denotes the Cauchy principle value of the integral. Assuming the relative permeability equals to 1, the refractive index $\tilde{n} = n + ik = \sqrt{\varepsilon}$,

$$n = \sqrt{\frac{|\varepsilon| + \varepsilon_1}{2}}, \tag{3.6a}$$

$$k = \sqrt{\frac{|\varepsilon| - \varepsilon_1}{2}}. \tag{3.6b}$$

The absorption coefficient is related to k by

$$\alpha = \frac{4\pi k}{\lambda_0}. \tag{3.7}$$

where λ_0 is the wavelength of the light in vacuum.

3.3 Calculated Optical Functions of GaP, GaAs

Since our $sp^3d^5s^*s_N$ parametrization for the dilute-N GaNP, GaNAs, and GaNPAs is largely based on our $sp^3d^5s^*$ parametrization optimized for GaP and GaAs (Section 2.5), the appropriateness of the $sp^3d^5s^*s_N$ parametrization for optical calculation depends heavily on the accuracy of optical results from the $sp^3d^5s^*$ parametrization.

Figures 3.1-3.2 show comparisons of the imaginary part of the dielectric functions and absorption coefficients of GaP and GaAs calculated from our TB parameter sets, and those from experiments. To demonstrate the advantageous outcome of the optimization we performed with optical fitting targets, we have also included in the comparison the results calculated from other widely used $sp^3d^5s^*$ TB parametrization. ε_2 functions calculated with ab initio methods are available for GaP and GaAs, we have also plotted a few relatively well-matched results for comparison.

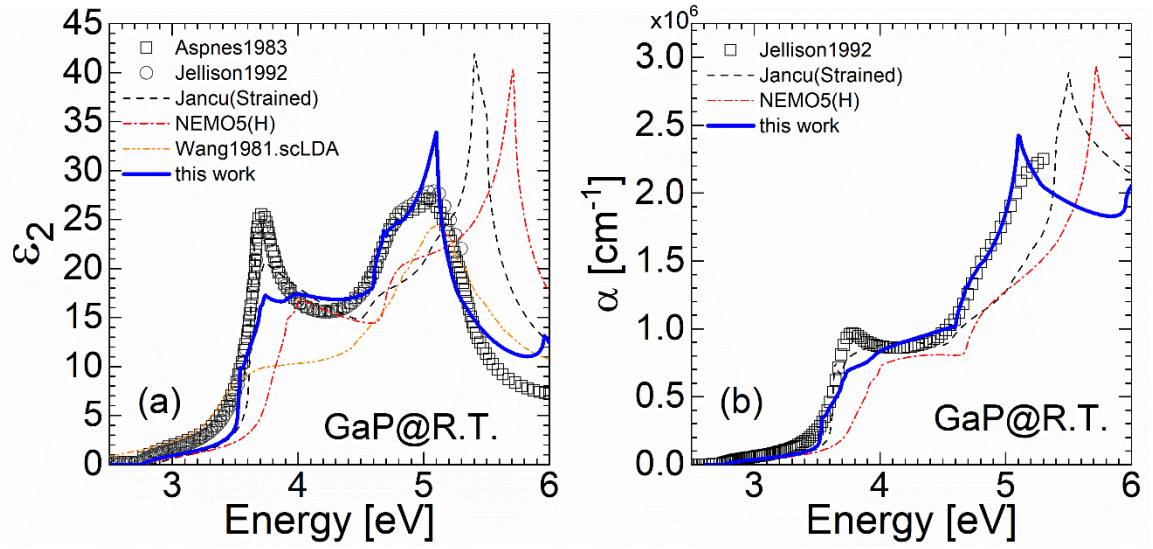

Figure 3.1 The imaginary part of the dielectric function and absorption coefficient of GaP from experiment (open symbols) [55], this work (solid blue curves), and other calculations (broken curves) [63], [64], [68].

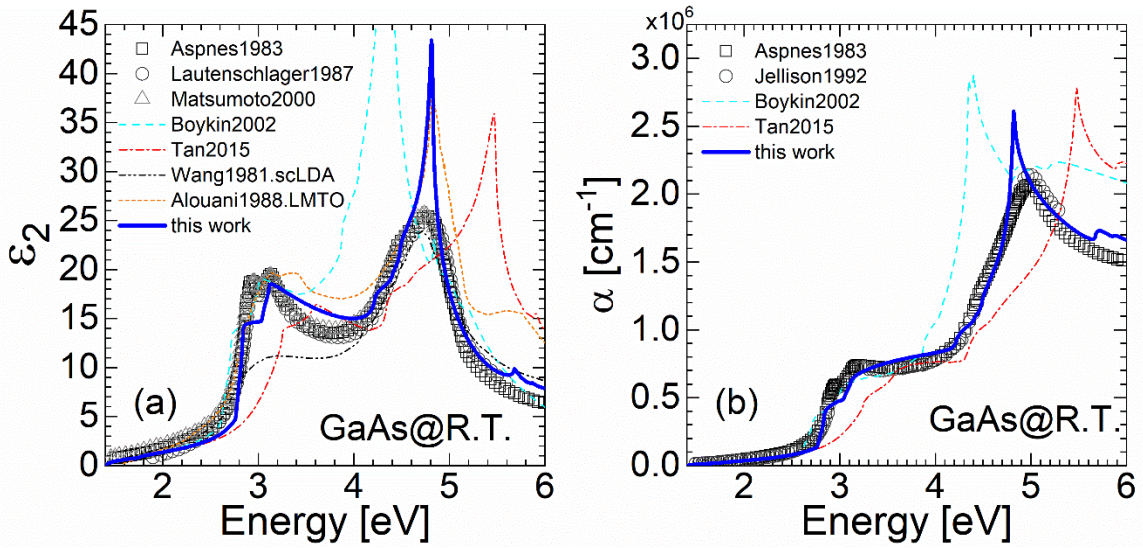

Figure 3.2 The imaginary part of the dielectric function and absorption coefficient of GaAs from experiment (open symbols) [55], [92]–[94], this work (solid blue curves), and other calculations (broken curves) [68]–[70], [95].

The optical functions calculated from our TB parameterization show excellent agreement with the experimental data in terms of the absorption edge, of the E_1 and E_2 peak positions, and of the spin-orbit interaction peak positions for both III-V materials, while experimental peak widths are somewhat broader as we did not include lifetime broadening or indirect transitions. The feature positions and shapes are however quite indicative that the present TB parameter sets should generate more accurate optical properties than other $sp^3d^5s^*$ TB parameter sets in comparison.

3.4 Calculated Optical Functions of Dilute-N GaNP, GaNAs, and GaNPAs

Systematic calculations have been carried out for the optical functions of dilute-N GaNP and GaNAs alloys with increase N mole fraction. As described by the $sp^3d^5s^*s_N$ model, when nitrogen is incorporated into GaP (GaAs), an E_{0-} state and an E_{0+} state form as a result of the anticrossing coupling of the lower (higher) localized N state and the higher

(lower) extended E_0 (also called Γ_c) state of the host. Similarly, E_{1-} and E_{1+} form near L, and E_{2-} and E_{2+} form near X. The increase in the N mole fraction has two main effects: (a) the anticrossing coupling strengthens, and the splitting between the newly formed paired states becomes larger, and (b) the N character decreases and the Γ_c character increases in the E_{0-} state, and the opposite happens in the E_{0+} state. For optical properties, the former effect shifts the transition energy positions, and the latter changes the optical coupling strengths, as the valence band Γ_v state couples much stronger to the extended Γ_c state than to the localized N state.

Figure 3.3 compares the calculated absorption coefficients with experimental measurements from literature. For GaP, there is no significant absorption below the 2.76 eV, because GaP has an indirect fundamental bandgap of 2.26 eV ($\Gamma - X$), and the smallest direct gap $E_0 = 2.76$ eV at Γ. However, it is seen, from both experimental and theoretical results, that there is absorption higher than 1×10^4 cm^{-1} well below 2.26 eV in dilute-N GaNP (due to E_{0-}), and that the absorption rises to more than 1×10^5 cm^{-1} beyond 2.76 eV (due to E_{0+} and E_{1-}). The absorption due to E_{0-} becomes stronger, as the N fraction increases and the Γ_c character increases. The calculated absorption due to E_{0-} for $GaN_{0.021}P_{0.979}$ is about two times stronger than experimental observation. This overestimation may originate from the virtual crystal nature of the $sp^3d^5s^*s_N$ model and thus the inhomogeneity of the dilute nitride alloys are not fully accounted for. Another possible reason could be an underestimation of the localized character of the E_{0-} states, which may be due to the neglect of N cluster states in the $sp^3d^5s^*s_N$ model. However, the

evidence is not strong enough to draw conclusions on this issue. The onset of the absorption also redshifts as the N concentration increases, which is in agreement with experiment.

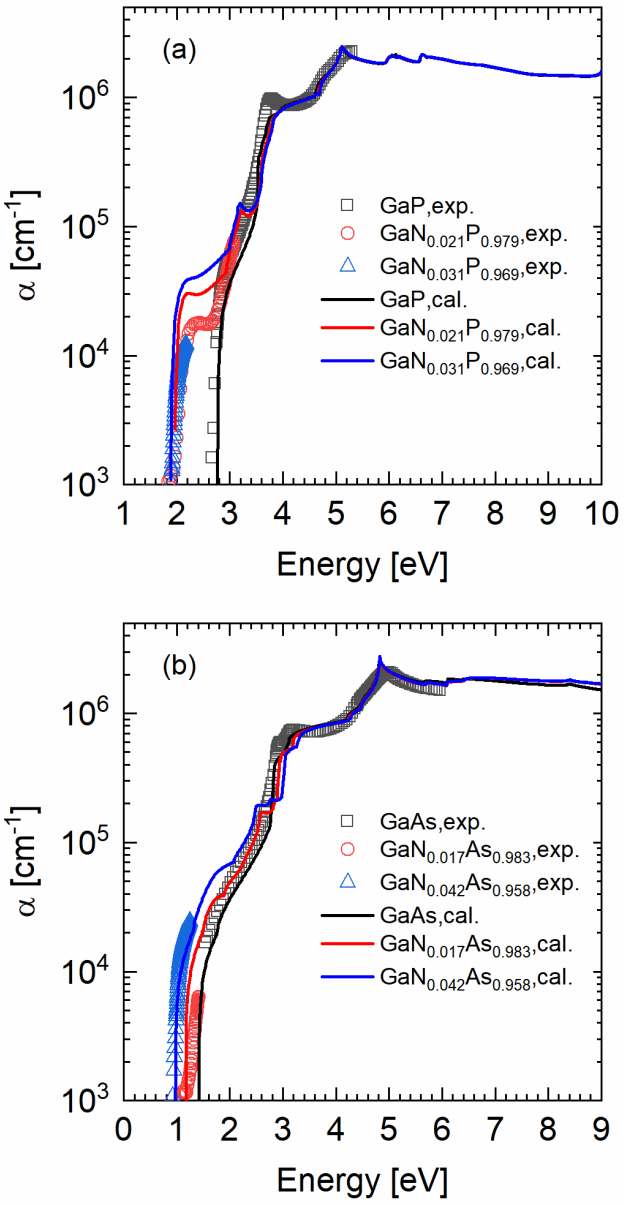

Figure 3.3 Measured (exp., solid symbols) [28], [55], [87], [92], [96]–[98] and calculated (cal., solid lines) absorption coefficients of (a) GaP and dilute-N GaNP, (b) GaAs and dilute-N GaNAs.

For GaNAs, the E_{0-} state has more Γ_c character than N character, as the Γ_c state is lower in energy than the N state. Therefore, the change in the onset of the absorption edge is not as dramatic as in the case of GaNP. Overall, the experimentally measured main effects of the N incorporation into GaP and GaAs are reasonably well described by the $sp^3d^5s^*s_N$ model.

To reveal the trends of the transitions at the critical points, the ε_2 spectra families calculated for GaNP and GaNAs alloys are plotted in Figure 3.4. One should note that some of the weaker optical features, such as E_{0+}, E_{1-}, and $E_{1-} + \Delta_1$, are difficult to see in room-temperature experiment due to lifetime-broadening and indirect transitions, but they are uncovered in the calculated results by including only direct transitions. For GaNP alloys, with increasing N mole fraction, the fundamental bandgap E_{0-} is pushed downward and the E_{0+} is repelled upward, the E_{1-} transition energy decreases and the E_{1+} energy increases, the E_0' slightly blue shifts while the E_{2+} remains essentially unchanged. No features due to spin-orbit interaction are obvious, because the split-off energies are small in GaP and the N incorporation does not change the split-off energies. These trends agree well with experimental observation [99]. The calculated ε_2 functions for GaNAs show very similar trends. The main difference is that the features due to spin-orbit interaction appear, as the split-off energies for GaAs are much larger than the splitting for GaP, although the features due to Δ_0 are not marked, as they are weak compared to those due to Δ_1. The trends in the calculated ε_2 for GaNAs also agree with reported experiments [100], [101].

Although the E_{s_N} and $s_c s_N \sigma$ parameters for GaNP and GaNAs were determined by fitting to their respective bandgaps only, the above examination of the calculated optical

functions suggests that the method used here is suitable for the estimation of the optical properties of dilute nitride alloys.

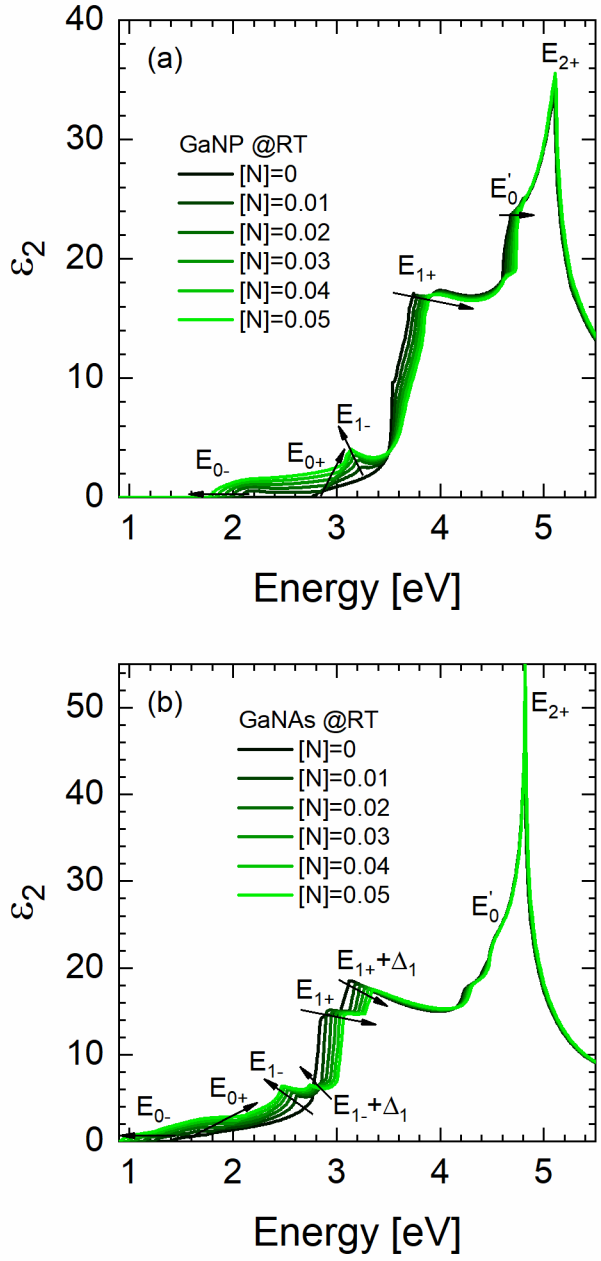

Figure 3.4 Calculated imaginary part of the dielectric functions of (a) GaNP and (b) GaNAs alloys. The arrows indicate the trends of the critical transitions with increasing nitrogen composition.

Finally, we linearly interpolate the $sp^3d^5s^*s_N$ Hamiltonians for GaNP and for GaNAs and apply the same method to calculate the optical functions of GaNPAs. Figure 3.5 shows a comparison of absorption coefficients of GaNPAs from this calculation and from experimental reports. The host materials of these four dilute nitrides are P-rich GaPAs in the indirect-bandgap alloy range [102], [103]. The linearly interpolated E_{s_N} are lower than the Γ_c of these host materials. This scenario is very similar to the case of dilute-N GaNP.

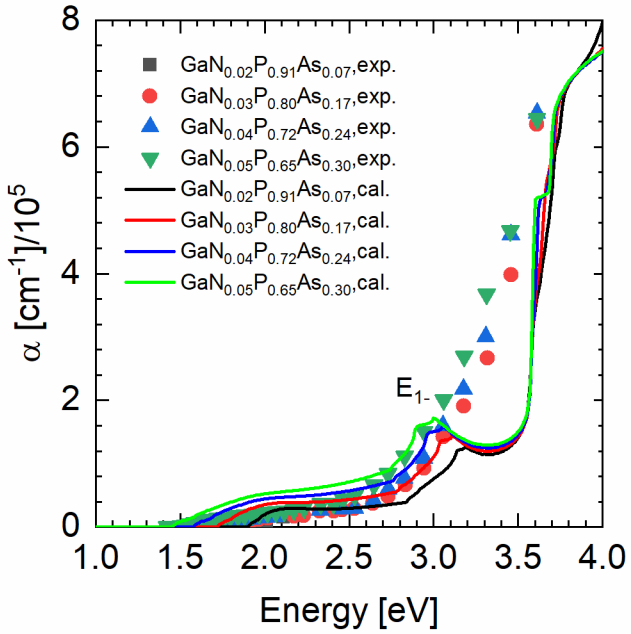

Figure 3.5 Absorption coefficients of GaNPAs alloys at room temperature from experiment [47] and from calculation in this work. (Only a few near bandgap data points for $GaN_{0.02}P_{0.91}As_{0.07}$ are extracted from literature due to digitization difficulty, and they are mostly covered by other data in this plot.)

The calculated spectra show about a factor of 2 overestimation below E_{0+} transitions, compared to experimental data. Further investigation is needed to elucidate the origin of this problem. On another note, this factor of 2 overestimation seems to be consistent with the case of GaNP. It may be possible to obtain more accurate optical calculation by

empirical scaling of the transition strength between the valence band state and the E_{0-} state. The underestimation above E_{1-} is mainly due to the neglect of indirect transitions and lifetime broadening effects. Overall, there is reasonably good agreement between the calculation and the experiment.

To show the effects on absorption of adding N and As into GaP, while keeping the alloy lattice-matched to Si, the calculated absorption coefficients for GaP, $GaN_{0.021}P_{0.979}$, and $GaN_{0.043}P_{0.856}As_{0.101}$ are plotted in Figure 3.6. The addition of N and As largely shifts the absorption edge to lower energy, with $GaN_{0.043}P_{0.856}As_{0.101}$ reaching 1.7 eV. The interaction between N and the host forms E_{1-} and E_{1+}. The former red shifts and the latter blue shifts with increasing N content. But the addition of As into GaP causes the E_1 transition to red shift and compensate the change in the E_{1+} energy.

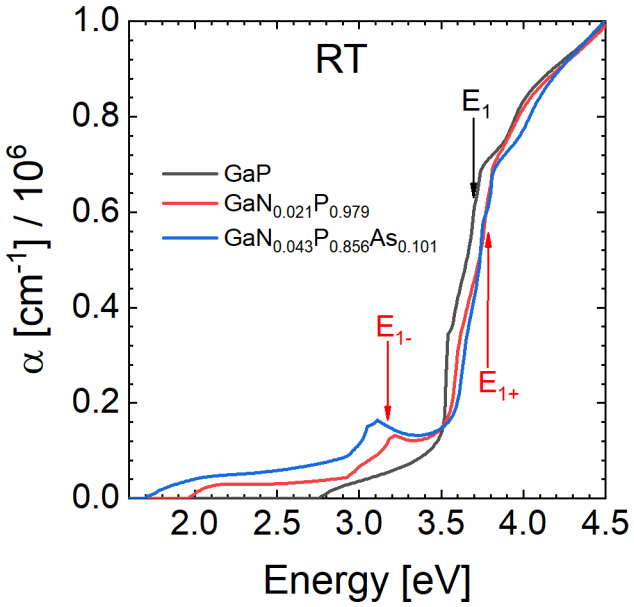

Figure 3.6 Calculated absorption coefficients for GaP, $GaN_{0.021}P_{0.979}$, and $GaN_{0.043}P_{0.856}As_{0.101}$ at room temperature. (The two alloys are lattice-matched to Si.)

In summary, the method used in this chapter can reveal the trends of the optical transitions as the N contents vary in the dilute-N alloys. It can be used as a computationally economical method for estimation of optical properties of dilute nitrides, as the quantitative agreement with experimental data is reasonably good. More accurate calculations may require large supercell Hamiltonians or modification of the $sp^3d^5s^*s_N$ model. The optical response functions calculated with the current method are used in simulations of solar cells involving dilute-N GaNP(As) (Chapter 6).

Chapter 4

MODELING CARRIER TRANSPORT IN DILUTE-NITRIDE GaNP

4.1 Motivation

Geisz *et al*. [104] tried to estimate the minority carrier diffusion lengths in dilute-nitride (dilute-N) GaInNAs from the quantum efficiency data of a $Ga_{0.95}In_{0.05}N_{0.02}As_{0.98}$ layer grown by metalorganic chemical vapor epitaxy (MOCVD). By fitting the measured quantum efficiency data, they concluded that the photo-generated carrier collection was dominated by the field aided collection within the depletion region and obtained the depletion width as 0.10 μm. This means that the minority carrier diffusion length in the GaInNAs layer should be less than 0.10 μm. Although longer minority carrier diffusion lengths were reported later in GaInNAs grown by molecular beam epitaxy (MBE) [105], the values were still well below 1 μm. These diffusion lengths are much smaller than those in high-quality GaAs, limiting the performance of solar cells made from these dilute nitrides.

Similar to the case of GaInNAs above, Geisz *et al*. found dramatic increase in the spectral response of a $GaN_{0.02}P_{0.98}$ on Si structure with the depletion width, and concluded that the carrier collection relied on field-aided collection and that the dilute-N GaNP material has a short diffusion length [50]. GaP/GaNPAs/GaP p-i-n structures also showed poor carrier collected limited by the short diffusion length of dilute-N GaNPAs [52], [106].

The underlining mechanisms causing these short diffusion lengths in dilute nitrides is not well understood. Small electron and hole mobilities have been measured from dilute-N GaNP samples [107], [108], which contribute to the short diffusion lengths. Here, we

use fullband Monte Carlo simulations to try to understand the carrier transport physics in dilute-N GaNP. The results shown in this chapter are a work in progress in this effort, more investigation needs to be done to fully understand the limiting scattering mechanisms on the mobility of dilute-N GaNP.

4.2 Introduction to Fullband Monte Carlo

The semiclassical description of carrier transport is given by the Boltzmann transport equation (BTE),

$$\frac{\partial f(\mathbf{r},\mathbf{k},t)}{\partial t}+\frac{1}{\hbar}\nabla_{\mathbf{k}}E(\mathbf{k})\nabla_{\mathbf{r}}f(\mathbf{r},\mathbf{k},t)+\frac{\mathbf{F}}{\hbar}\nabla_{\mathbf{k}}f(\mathbf{r},\mathbf{k},t)=\left.\frac{\partial f(\mathbf{r},\mathbf{k},t)}{\partial t}\right|_{collison}, \qquad (3.1)$$

where f is the distribution function, **r** is the real space position vector, **k** is the momentum vector, $\hbar$ is Planck's constant, E is the energy, **F** is the field vector. This equation states that the time rate of change of the distribution functions equals to the sum of the rates of change due to diffusion (second term on the left-hand side), drift (third term on the left-hand side), and collisions (the term on the right-hand side), which includes in-scattering and out-scattering.

The ensemble Monte Carlo (EMC) method is a stochastic approach to solve the BTE exactly in the long-time limit. It simulates carrier transport as a series of free flights and scattering events. Macroscopic transport properties are obtained from the ensemble values by tracking the trajectories of a sufficiently large number of particles for a given time duration. The free flights are treated classically, and the scattering events are treated quantum mechanically. The electronic structure determines what states the particles can occupy. TB electronic structures (Chapter 2) throughout the entire first Brillouin zone are

used for this purpose. If from t_1 to t_2, no scattering occurs to a particle, the particle "flies freely" during this time period, and the wave vector of this particle at time t_2 is given by

$$\mathbf{k}(t_2) = \mathbf{k}(t_1) + \frac{q(\mathbf{F} + \mathbf{v} \times \mathbf{B})(t_2 - t_1)}{\hbar}, \tag{3.2}$$

where q is the charge of the particle, $\mathbf{v}$ is the velocity, $\mathbf{B}$ is the magnetic field. The probability of scattering in the time interval dt after a free flight of time t can be written as

$$P(t)dt = \Gamma_{total}[\mathbf{k}(t)] \exp\left[-\int_0^t \Gamma_{total}\left[\mathbf{k}\left(t'\right)\right] dt'\right] dt, \tag{3.3}$$

where $\Gamma_{total}[\mathbf{k}(t)]$ is the total scattering rate at wave vector $\mathbf{k}(t)$

$$\Gamma_{total}[\mathbf{k}(t)] = \sum_i \Gamma_i[\mathbf{k}(t)], \tag{3.4}$$

with Γ_i being the scattering rate due to mechanism i. Traditional EMC expresses the scattering rates as functions of energy through the use of the dispersion relation. During a simulation, it randomly selects the scattering mechanisms, determines the energy of the particle after scattering, and then scans the constant energy surface at that final energy, and randomly chooses the final state based on the weights (probabilities) given by the density of states, overlap integral, and transition matrix element [109]. These calculations are time-consuming. To speed up these simulations, we discretize the Brillouin zone into small cells, and calculate and store the scattering rates from each pair of initial cell and final cell at the beginning of the simulations, and simply use random numbers to select final cell, and only

use the traditional EMC in scarcely populated or less eventful regions (the hybrid fullband cellular automaton/Monte Carlo approach [110]).

The nonpolar phonon scattering rate from a region $\Omega_{\mathbf{k}}$ of band v centered at point $\mathbf{k}$ to a region $\Omega_{\mathbf{k}'}$ in band v' centered around point $\mathbf{k}'$ is written as

$$P_{non,vv'}(\Omega_{\mathbf{k}}, \Omega_{\mathbf{k}'}) = \frac{\pi}{\rho\omega_{\eta\mathbf{q}}}\left|\Delta_{\eta,v'}(\mathbf{q})\right|^2 |I(v, v', \mathbf{k}, \mathbf{k}')|^2 D_{v'}(E', \Omega_{\mathbf{k}'})\left(n_{\eta\mathbf{q}} + \frac{1}{2} \mp \frac{1}{2}\right), \quad (3.5)$$

where ρ is the material density, $\mathbf{q}$ is the wave vector difference $\mathbf{q} = \mathbf{k}' - \mathbf{k}$,, $\Delta_{\eta,v'}(\mathbf{q})$ is the nonpolar matrix element as defined in [109], ω is the phonon frequency, I is the overlap integral between the two states, $D_{v'}(E', \Omega_{\mathbf{k}'})$ is the density of states in $\Omega_{\mathbf{k}'}$ at energy $E' = E \pm \hbar\omega_{\eta\mathbf{q}}$, and $n_{\eta\mathbf{q}}$ is the phonon occupation number determined by the Bose-Einstein distribution. The acoustic and optical deformation potentials $\Delta_{\eta,v'}(\mathbf{q})$ are treated as adjustable parameters to produce good agreement with experimental data. The polar phonon scattering rate is expressed as

$$P_{pol,vv'}(\Omega_{\mathbf{k}}, \Omega_{\mathbf{k}'}) = \frac{\pi e^2 \omega_{\eta\mathbf{q}}}{2\mathbf{q}^2}\left[\frac{1}{\varepsilon_\infty} - \frac{1}{\varepsilon_0}\right] |I(v, v', \mathbf{k}, \mathbf{k}')|^2 D_{v'}(E', \Omega_{\mathbf{k}'})\left(n_{\eta\mathbf{q}} + \frac{1}{2} \mp \frac{1}{2}\right), \quad (3.6)$$

where ε_∞ and ε_0 are the optical and static permittivities, respectively. Ionized dopants act as ionized impurity scattering centers. The ionized impurity scattering rate according to the Brooks-Herring approach [109], [111] is

$$\Gamma_{BH,v}\left(\mathbf{k}, \mathbf{k}'\right) = \frac{Z^2 N_B e^4}{4\pi^2 \hbar \epsilon_0} \sum_{v'} \frac{\left|J\left(\mathbf{k}, \mathbf{k}'\right)\right|^2}{(\beta_s^2 + |\mathbf{k} - \mathbf{k}'|^2)^2} \delta\left(E_v(\mathbf{k}) - E_{v'}(\mathbf{k}')\right), \quad (3.7)$$

where N_B is the ionized impurity concentration, Z is the number of elemental charges of the dopant, and β_s is the Debye-Huckel screening [112] term for non-degenerate systems

$$\beta_s = \left(\frac{e^2 n}{\epsilon_0 k_B T}\right)^2, \tag{3.8}$$

where n is the carrier density, T is the carrier temperature. However, Eq. 3.7 only accounts for two-body interaction. The many-body effect can be approximated by screening using the Ridley model [113], and the ionized impurity scattering rate is corrected as

$$\Gamma_{ion,v}\left(\mathbf{k}, \mathbf{k}'\right) = \frac{v_g(\mathbf{k})}{(2\pi N_B)^{-\frac{1}{3}}}\left[1 - \exp\left(\frac{\Gamma_{BH,v}\left(\mathbf{k}, \mathbf{k}'\right)(2\pi N_B)^{-1/3}}{v_g(\mathbf{k})}\right)\right], \tag{3.9}$$

Alloy scattering due to the fluctuation of crystal potential follows the work of Fischetti and Laux [114] as

$$\Gamma_{alloy}(\mathbf{k}) = \sum_b \theta[E^a(\mathbf{k}) - E^b]\frac{2\pi}{\hbar}\Omega_c x(1-x)\Delta U^2 \rho^b[E^a(\mathbf{k})]\langle|I_{ab}|^2\rangle. \tag{3.10}$$

where a and b are the band indices, $\theta(E)$ is the step function, Ω_c is the cell volume, x is the alloy fraction, ΔU is the effective depth of the scattering well, $\rho^b(E)$ is the nonparabolic density of states in band b.

4.3 Carrier Mobilities of Dilute-N GaNP by Fullband Monte Carlo

The carrier transport properties of GaNP are not well understood. To the author's knowledge so far, there are only two reports on the mobilities in GaNP. In one report, the electron Hall mobilities of S- and Te-doped n-type GaNP were measured at different

temperatures. At room temperature, the electron mobilities are about 20 $cm^2/(V\text{-}s)$. The temperature dependence results seem to suggest the electron Hall mobilities of the n-GaNP are limited by ionized impurity scattering ($\propto T^{1.5}$) [107]. In the other report, the measured hole Hall mobility of C-doped p-type GaNP reduces from 55 $cm^2/(V\text{-}s)$ at 1×10^{17} cm^{-3} hole concentration to 12 $cm^2/(V\text{-}s)$ at 7×10^{19} cm^{-3}. These values are significantly lower than those of GaP, but do not seem to depend on the N fraction, but only on the onset of the addition of N [115].

Here we investigate the carrier mobility of dilute-N GaNP using the fullband Monte Carlo (MC) method described above. First, the optimized $sp^3d^5s^*$ parametrization (Chapter 2) is adopted to calculate the fullband structure of GaP, which is then input into the MC algorithm, where carrier interaction with acoustic phonons, optical phonons, and ionized impurities are included. The acoustic and optical deformation potentials are adjusted to achieve good agreement with experimentally reported mobilities [116]. The comparison is shown in Figure 4.1. The non-smoothness of the curves come from statistical noise, as using a large enough number of particles in the MC simulations to make the curves smooth is impractical at the moment. One should note that the experimental GaP hole mobility was measured in a background of 5×10^{16} cm^{-3} n-type doping, and the simulation took this into account by including doping compensation. As reasonable agreement is achieved, the acoustic and optical deformation potentials are determined.

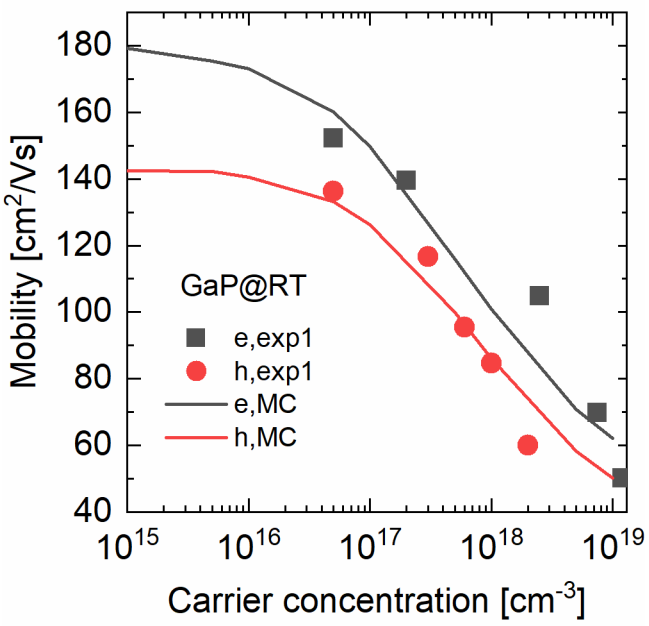

Figure 4.1 Electron (dark grey) and hole (red) mobilities from Hall measurement [116] (symbols) and from fullband Monte Carlo simulation (solid lines).

After that, we use the $sp^3d^5s^*s_N$ parametrization for GaNP (Chapter 2) to account for the effects of N incorporation provided by the $sp^3d^5s^*s_N$ model, and carry out MC simulations with other inputs unchanged. Figure 4.2 compares the simulated and measured electron mobilities. The experiment shows that the 0.4% to 1.9% N content causes about 5 to 8 times reduction in the mobility. The $sp^3d^5s^*s_N$ model reduces the simulated mobilities by about 10 times. This is explained by the small curvature of the E_- band, and thus by the large electron effective mass, calculated with the $sp^3d^5s^*s_N$ model. The simulated values for 0.5% and 2.0% N are quite close, and the noise makes accurate comparison difficult. Overall, the $sp^3d^5s^*s_N$ model can approximately account for the electron mobility reduction due to N incorporation measured for these samples.

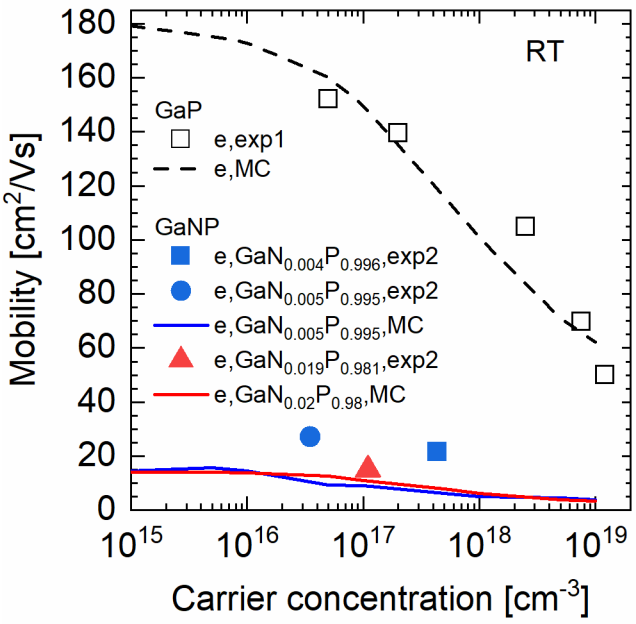

Figure 4.2 Electron mobilities of GaP and GaNP from Hall measurement [107], [116] (symbols) and from fullband Monte Carlo simulation (lines).

Similar MC simulations are done for the holes, and are compared with experiment (see Figure 4.3). As mentioned above, the experimental GaP hole mobility was measured with a background concentration of 5×10^{16} cm^{-3} n-type doping, and the simulation took this into account initially. But for the GaNP samples, there was no unintentional doping reported, therefore, doping compensation was removed from the simulation. Within the noise errors, the simulated hole mobilities are essentially independent of N mole fraction, as the $sp^3d^5s^*s_N$ model does not change the valence band. However, the experimental hole mobilities for GaNP are much lower than those for GaP.

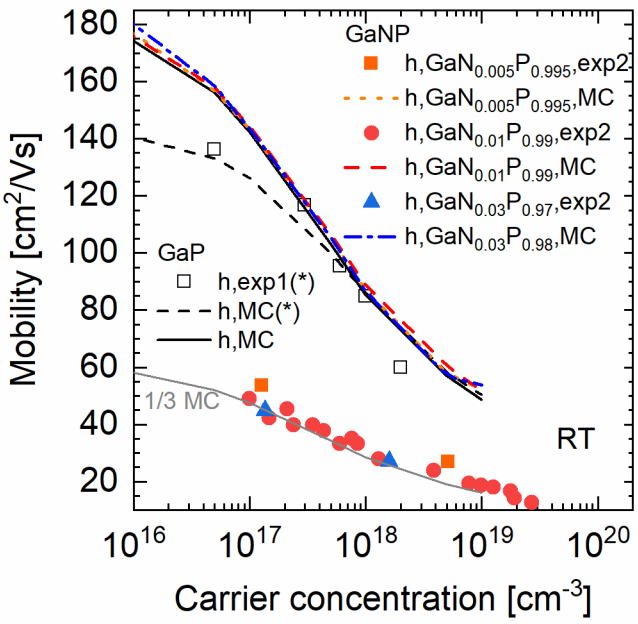

Figure 4.3 Hole mobilities of GaP and GaNP from Hall measurement [116], [117] (symbols) and from fullband Monte Carlo simulation (lines). The (*) indicates there is unintentional n-type doing of 5×10^{16} cm^{-3} [116]. The discrepancy between the black solid line and the black dashed line shows the difference made by the unintentional doping. Without compensation doping, all the hole mobilities simulated without unintentional doping are essentially the same. The grey line is drawn by bringing the black line down to 1/3 of its values.

If the simulated GaNP hole mobilities are brought down to 1/3 of their values (the grey line in Figure 4.3), there could be a good agreement. The mobility μ_h relates to the scattering time τ_h as

$$\mu_h = \frac{e\tau_h}{m^*}, \tag{3.11}$$

Rearranging Eq. 3.11 gives

$$\frac{e}{m^*\mu_h} = \frac{1}{\tau_h} = \frac{1}{\tau_{h,MC}} + \frac{1}{\tau_{h,X}} = \frac{e}{m^*}\left(\frac{1}{\mu_{h,MC}} + \frac{1}{\mu_{h,X}}\right). \tag{3.12}$$

Since $\mu_h \cong 1/3\ \mu_{h,MC}$, there is some scattering mechanism in the real samples that is twice as strong as the sum of the included deformation scattering, polar optical phonon scattering, and ionized impurity scattering.

This strong scattering mechanism has not been identified yet. But it is independent of N content. We did not include alloy scattering or neutral impurity scattering in the simulations for comparison, as they both have obvious dependency on the N mole fraction. One possibility is that the samples may have very high dislocation densities, and the dislocation densities are similar among the samples. Another possibility could be the N incorporation changes the nature of phonon scattering. Further investigation is needed.

Chapter 5

EFFECTS OF GaP/Si INTERFACIAL TRAPS ON A Si HETEROJUNCTION INTERDIGITATED BACK CONTACT SOLAR CELL

5.1 Introduction

Over the past few decades, the efficiencies of single-junction silicon solar cells have improved from less than 10% to the current 26.6% record in an interdigitated back contact (IBC) configuration [118]. The most common similarity among the recent reports of high-efficiency Si solar cells is their high open-circuit voltage (V_{oc}) achieved through a highly passivated heterojunction of crystalline Si (c-Si) with a thin layer of intrinsic amorphous Si (a-Si). To improve upon this, there has been interest in replacing the a-Si layer with a higher bandgap material such as GaP, which should have lower parasitic absorption. Crystalline GaP has the advantage of much higher carrier mobilities (smaller resistive losses) compared to a-Si. In addition to single-junction schemes, GaP can also serve as a buffer layer in a lattice-matched dilute-N GaNPAs/Si multijunction (or tandem) structure, since the lattice constant of GaP is only 0.36% larger than that of Si. However, solar cells with a GaP/Si heterojunction have been shown to have V_{oc} at least 100 meV lower than well passivated Si cells [119]–[121].

One complication in the epitaxial growth of GaP on Si is the formation of antiphase domains (APDs), which stem from the atomic steps on non-perfect Si surfaces. Recently, a double-step treatment has been used to significantly reduce the volume of APDs, which improved the solar device performance [122]. Another way to reduce the APDs is to grow on off-cut ($\geq 4°$) Si wafers [123], [124].

Density functional theory calculations have shown that there are a high density of localized states at the GaP/Si interface due to electron valence mismatch, and that hydrogen can be used to reduce these localized states in the forbidden gap [125]. However, no study has shown how these midgap states impact the performance of an IBC solar cell with a GaP/Si interface.

This chapter presents an investigation on the effects of two-types of single-level midgap traps at the GaP/Si interface on Si heterojunction interdigitated back contact solar cells (SHJ-IBCs). Here midgap means in the middle of the Si bandgap. We first build an SHJ-IBC model with an a-Si(i)/Si(n) front interface and calibrate the model with a demonstrated 26.3% cell [5] as a reference. We then modify the model by replacing the front a-Si layer with a GaP layer. The GaP layer will be either intrinsic or highly n-type doped. Simulations were carried out with increasing density of either donor-like or acceptor-like midgap traps at the GaP/Si interface. The effects of the traps under no field or a front surface field are modeled and discussed.

5.2 The Device Model

We have simulated an a-Si(i)/c-Si(n)/a-Si(i)/IBC (n-, p-type a-Si) solar cell, and GaP/c-Si(n)/a-Si(i)/IBC (n-, p-type a-Si) solar cells, using the numerical 2D simulation package, Silvaco ATLAS [53]. Figure 5.1 shows the simulated structure. Periodic boundary conditions are applied to the left and right boundaries to simulate cells with multiple pn back contact pairs.

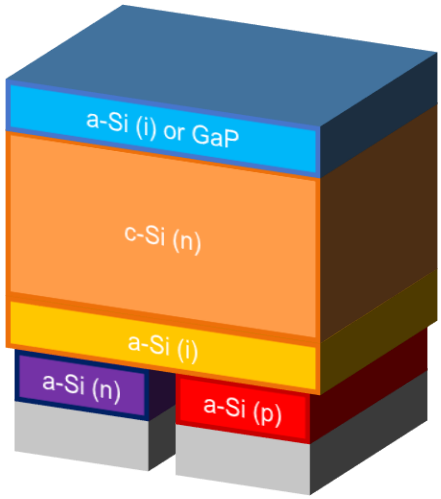

Figure 5.1 Schematic model of the simulated Si heterojunction interdigitated back contact solar cells with either an a-Si/c-Si interface or a GaP/Si interface at the front.

The a-Si layers were described using a defect pool model which assumes exponential tail states and Gaussian-profile states within the bandgap [126]. The drift-diffusion model, Shockley-Read-Hall recombination, and Auger recombination are accounted for in the bulk of the materials, while thermionic emission and field emission models [127], [128] are used to account for carrier transport over and through the hetero-interfaces, with the Richardson constants specified by the effective conduction and valence band density of states. Localized states at the interface are modeled as single-level midgap traps, either donor-like or acceptor-like. The capture cross sections for electrons and holes are both assumed to be 1×10^{-15} cm^2, which is within a reasonable range. Ray tracing was used as the optical model for these simulations. The front surface reflection is specified based on values reported from literature [5]. The number of reflections and the cutoff power ratio were chosen to be 20 and 3×10^{-3}, respectively, to obtain high long-wavelength external

quantum efficiency (EQE). Some of the parameters of the model are summarized in Table 5.1.

Table 5.1 Parameters for the device model.

	c-Si	a-Si (i)	GaP
Thickness (μm)	165 [129]	0.005	0.005
Doping (cm^{-3})	n (1.5×10^{15}) [129]	i	i or n (1×10^{19})
Affinity (eV)	4.05 [130]	3.8 [131]	3.8 [132]
Bandgap (eV)	1.12 [133]	1.75 [134]	2.26 [135]
Refract. indices	[136]	[137]	[55]
N_c (cm^{-3})	3.2×10^{19} [133]	2.0×10^{21} [134]	1.8×10^{19} [138]
N_v (cm^{-3})	1.8×10^{19} [133]	1.0×10^{22} [134]	1.9×10^{19} [138]
μ_n (cm^2/Vs)	1100 [139]	1 [134]	230 [138]
μ_p (cm^2/Vs)	430 [140]	0.05 [134]	130 [138]
Bulk lifetime (s)	8.8×10^{-3} [129]	1×10^{-6} [134]	1×10^{-6} [138]

5.3 Effects of Interfacial Traps on an SHJ-IBC with an Intrinsic a-Si or GaP Front Layer

We first carried out baseline simulations of SHJ-IBC solar cells with a 5-nm intrinsic a-Si layer at the front (AS1), and with a 30-nm intrinsic GaP layer at the front (GP1) without interface traps. Figure 5.2 compares the simulated J-V curves and EQE results with the experimental demonstration from [5]. a-Si(i) has stronger absorption and poorer carrier transport properties compared to GaP, which causes AS1 to have a slightly lower short-wavelength response than GP1. However, the a-Si(i) layer is so thin that the parasitic loss is trivial, and the J-V results for AS1 and GP1 are almost the same. Overall, the AS1 model

should be reasonably close to reality, as compared to the reference cell. The main differences are the higher V_{oc} and fill factor (FF) for the simulations. To obtain an exact match requires fine tuning of layer thickness, doping, or other material parameters, which is not the main focus of this work.

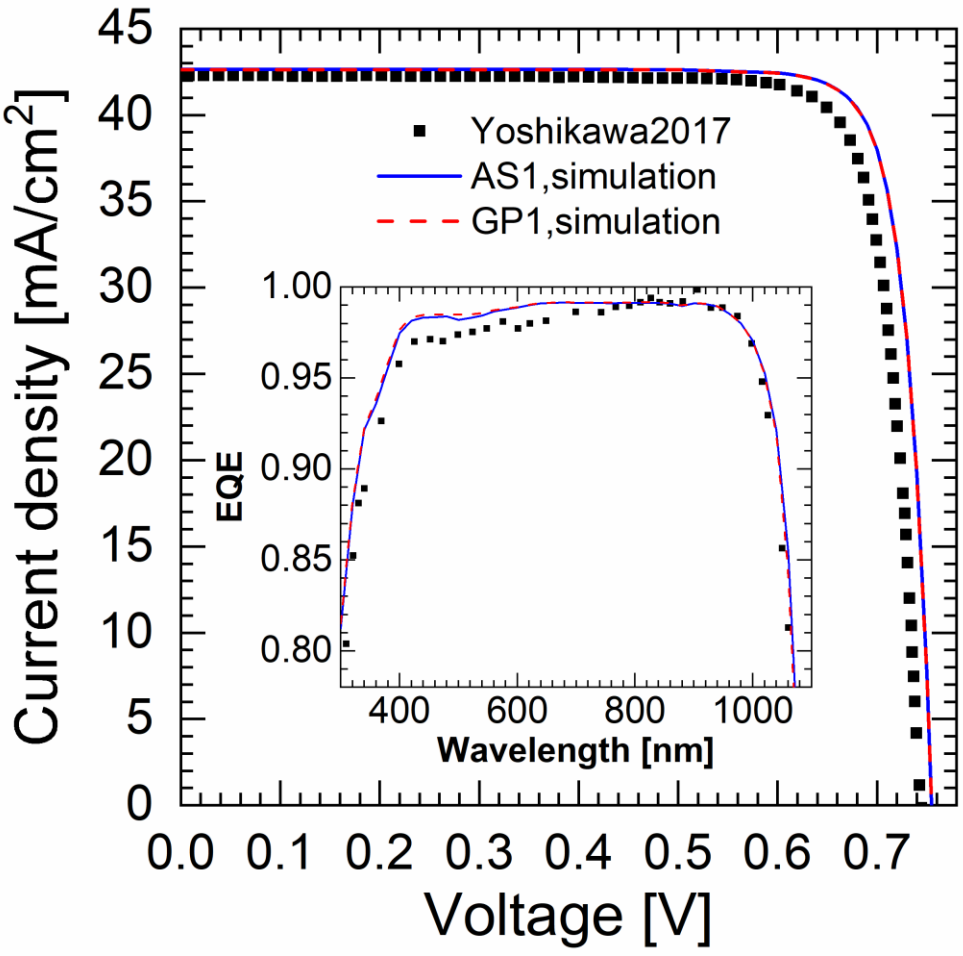

Figure 5.2 Comparison of J-V and EQE (inset) curves from simulations (lines) and experiment [5] (squares). The J-V curves for AS1 and GP1 are essentially overlapping with each other.

Hydrogenated a-Si is well known to provide excellent surface passivation to c-Si. But a real GaP/Si interface may have a high density of trap states as mentioned [125], which

can play a significant role in device performance. Figure 5.3 shows the change in J-V performance by adding either acceptor-like or donor-like single-level midgap traps at the GaP(i)/Si(n) interface. The traps start to make significant impact to the solar cell with a density as small as 1×10^{9} cm^{-2}, which is a low interface state density. In the case of donor trap density of 1×10^{10} cm^{-2}, the short-circuit current density (J_{sc}), V_{oc}, and FF drop 13.7%, 6.3%, and 9.0%, respectively. The maximum contribution to the J_{sc} from the absorption in the thin GaP layer is less than 0.86 mA/cm^2. The traps impact the solar performance mainly through their effect on the carriers generated in the Si. The reduction in J_{sc} only accounts for a small portion of the reduction in V_{oc}. The main reduction in V_{oc} should originate from an increase in the dark saturation current (J_0). Figure 5.4 shows a band diagram of the GaP(i)/Si(n) interface calculated with Silvaco ATLAS [53]. The bands are flat, and both types of carriers can easily access the interface. When there are traps at the interface, these carriers recombine readily. Figure 5.5 shows the recombination rate (RR) near the GaP(i)/Si(n) interface. The RR on the GaP side is much lower than on the Si side, because carrier concentrations are lower in the former than the latter. With $1x10^{10}$ cm^{-2} interface traps, the interface RR is more than six orders of magnitude higher than when there are no interface traps. The higher interface recombination reduces the carrier concentrations in the bulk of Si, and thus the RR in the bulk is smaller than the case without interface traps. However, the bulk RR's are low, and should not be a limiting factor to cell performance.

Since the GaP(i)/Si(n) interface "welcomes" both types of carrier to come close, and the Si has only a low-level of n-type doping, the densities of both types of carriers at the interface are almost equal. Therefore, acceptor-like traps (ALTs) and donor-like traps

(DLTs) induce similar RR's at the interface (Figure 5.5), and have almost the same effect to the device (Figure 5.3).

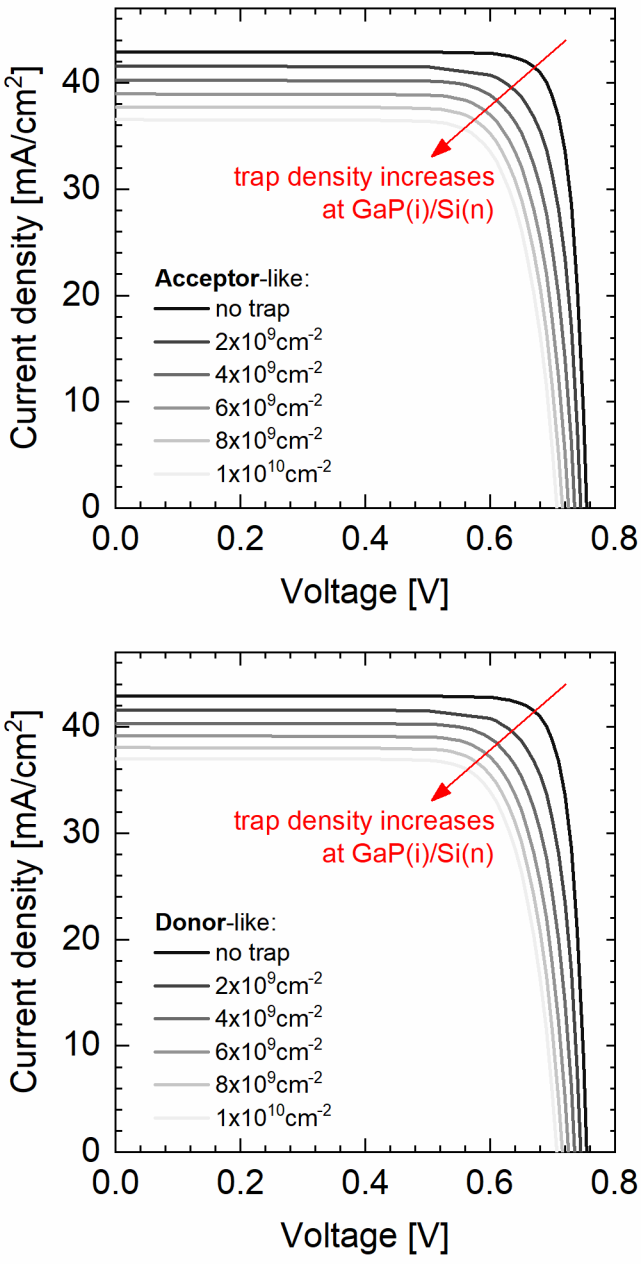

Figure 5.3 J-V curves of GP1 with different densities of interface acceptor-like and donor-like midgap traps.

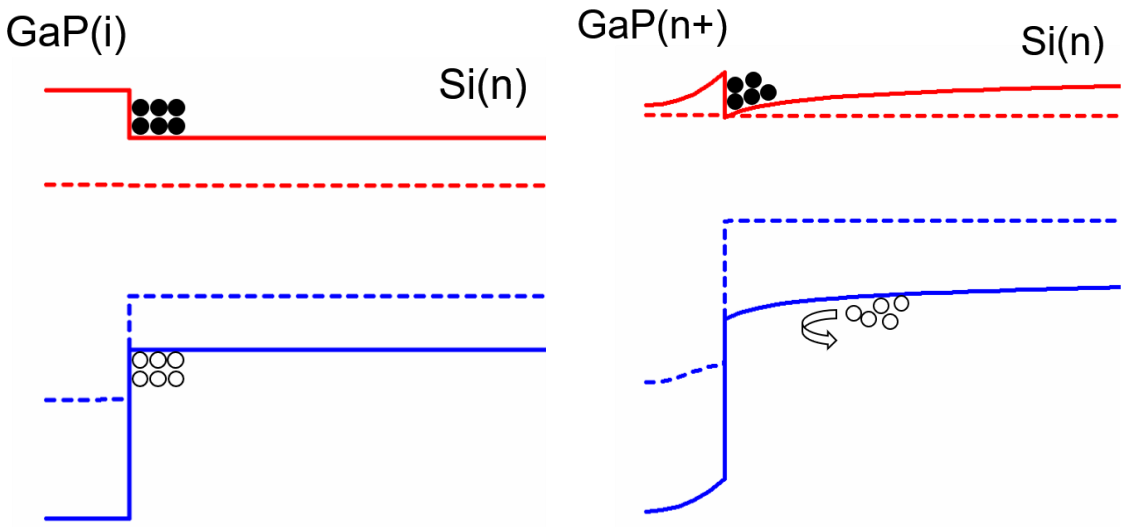

Figure 5.4 Band diagrams of GaP(i)/Si(n) and GaP(n+)/Si(n) interfaces without traps calculated using Silvaco ATLAS [53]. Symbols and texts are drawn for illustration. The solid circles, hollow circles, and solid black lines symbolize electrons, holes, and traps, respectively. The solid red (blue) lines and dashed red (blue) lines represent conduction (valence) bands and electron (hole) quasi-Fermi levels. The large discontinuities in the quasi-Fermi levels indicate that the thermionic emission process is limiting the transport at the heterojunction interface [141].

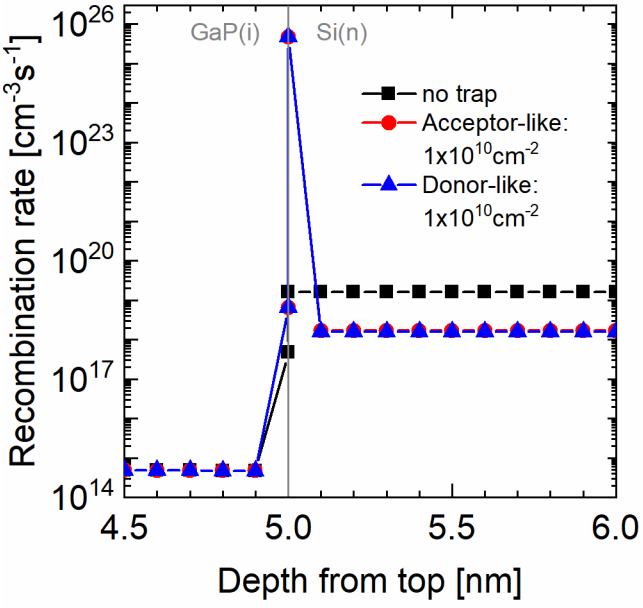

Figure 5.5 Recombination rates at the GaP(i)/Si(n) interface of model GP1, with a grid spacing of 0.1 nm.

5.4 Effects of Interfacial Traps on an SHJ-IBC with a GaP Front Surface Field Layer

High recombination at the front is detrimental to an IBC cell, since the photogenerated carriers need to transport to the back to be collected. Therefore, it is important to keep the carriers from having access to the interface traps at the GaP/Si interface. One way to achieve this is to have a highly doped layer to create a front surface field (FSF) that reduces the density of carriers at the interface. We have simulated SHJ-IBC cells with a GaP(n+)/Si(n) interface (Model GP2) to see the impact of interface traps under the influence of an FSF. Figure 5.4 also shows the band diagrams of GP2 near the GaP/Si interface. With a highly doped n+ GaP layer (1×10^{19} cm^{-3}), the concentration of minority holes in the Si layer is reduced exponentially near the interface, while the concentration of electrons is increased exponentially near the interface.

The interface RR on the Si side for all cases have extracted. Figure 5.6 plots the RR's at the GaP/Si interface with and without an FSF. As mentioned above, the RR's caused by ALTs and DLTs are very close without an FSF. The FSF lowers the RR for about 3 orders of magnitude for a trap density of $1x10^{10}$ cm^{-2}. When the trap density is relatively low, the ALTs and DLTs at the GaP(n+)/Si(n) surface also cause very similar RR, as the band bending and carrier concentrations are largely unchanged.

However, the situation is different for high trap densities. A trap can be either empty or filled. When filled, the trap carries a negative (positive) charge, if it is acceptor-like (donor-like). If there is a significant density of the charged traps at the interface, the band bending and hence the carrier concentrations change, and so does recombination. Figure 5.7 compares the band diagrams near the interface with ALTs or DLTs. Since electrons are

the majority carriers at the GaP(n+)/Si(n) interface, any ALT will most likely be filled with electrons, while a DLT has a small chance to be occupied by a hole. As the ALT density increases, the band bending on the Si side is reduced by the negatively charged interface, and eventually flattens. As shown in Figure 5.7, when the ALT density is $5x10^{12}$ cm^{-2}, the band bending on the Si side is, although reduced, still significant, and the quasi-Fermi level separation in Si is largely unchanged. But when the ALT density is $5x10^{12}$ cm^{-2}, the bands on the Si side are already flat, and the quasi-Fermi level separation is apparently reduced, indicating large reduction of the photogenerated carriers. This is because once the bands on the Si side become flat, most photogenerated carriers will recombine at the front (low carrier concentration in Figure 5.8), rather than being collected at the back of the IBC cell, which strongly degrades the conversion efficiency (Figure 5.9). This can explain the big drop in J-V performance from an ALT density of $4x10^{12}$ cm^{-2} to $5x10^{12}$ cm^{-2}, as shown in Figure 5.9.

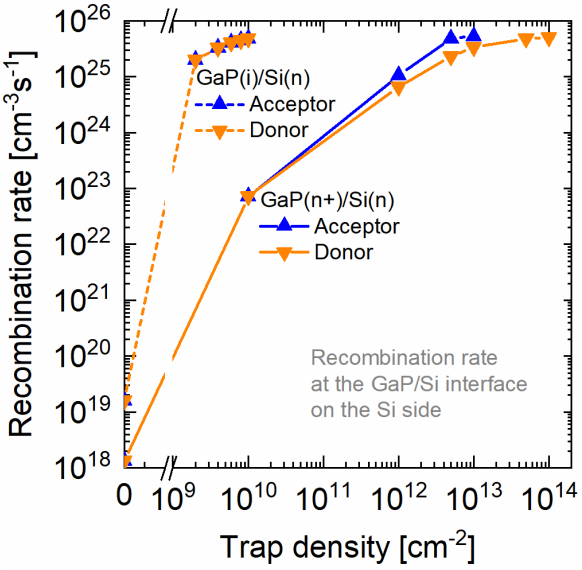

Figure 5.6 Interface recombination rates on the Si side with and without doping in the GaP layer.

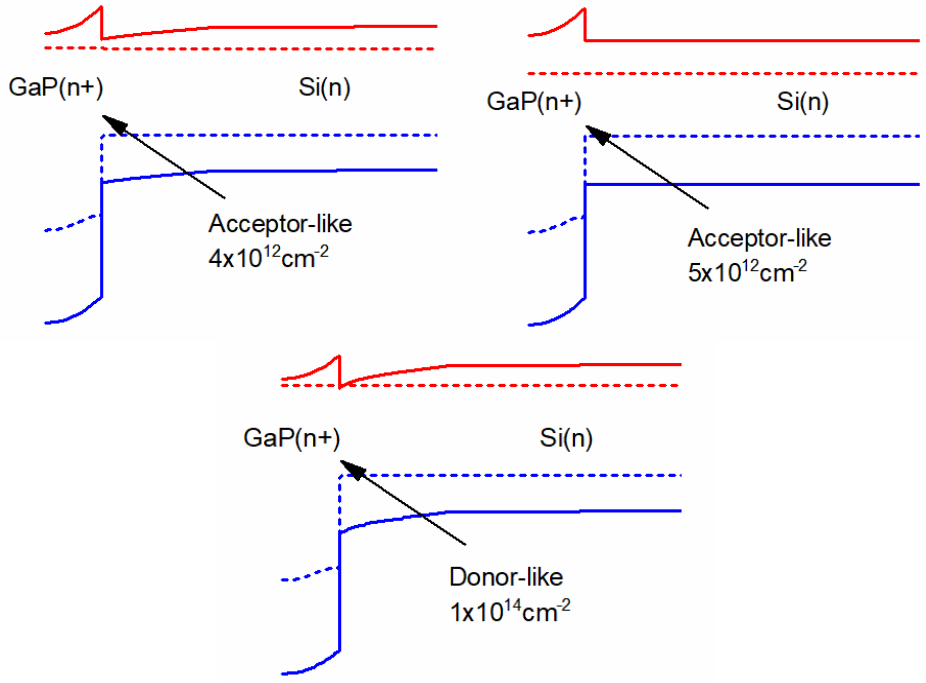

Figure 5.7 Band diagrams of the GaP(n+)/Si(n) interface with $4x10^{12}$ cm^{-2} (upper left) and $5x10^{12}$ cm^{-2} (upper right) acceptor-like traps and $1x10^{14}$ cm^{-2} donor-like traps (lower), calculated with Silvaco ATLAS [53].

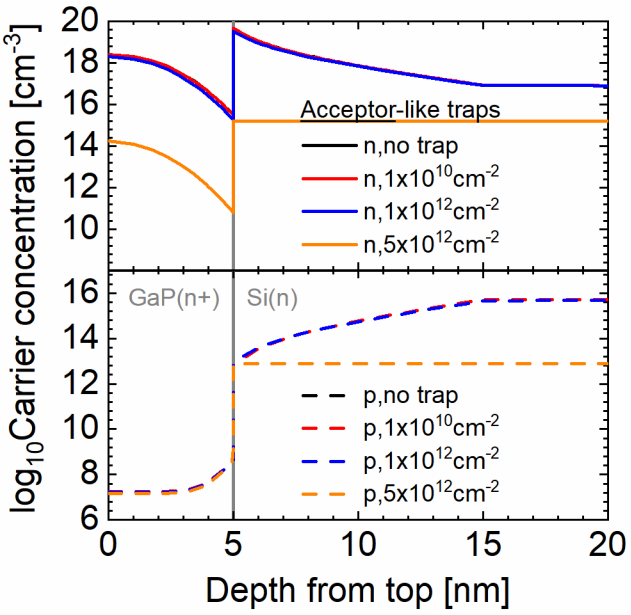

Figure 5.8 Electron (upper panel) and hole (lower panel) concentrations near the GaP(n+)/Si(n) interface with acceptor-like traps.

In the case of DLTs, a hole has a low probability of occupying a trap at the interface. And when it occupies a trap, it is very likely to recombine with a majority electron. The lightly positively charged interface helps maintain or even makes the band bending slightly stronger. As shown in Figure 5.7, the band bending at a DLT density of $1x10^{14}$ cm^{-2} is negligibly larger than the one without traps. This makes the IBC cell very robust against DLTs. The 1/5 of power loss at a DLT density of $1x10^{14}$ cm^{-2} (Figure 9) is relatively low compared to the case of ALTs. The V_{oc} degrades faster than J_{sc}, due to the fast increase in recombination or J_0.

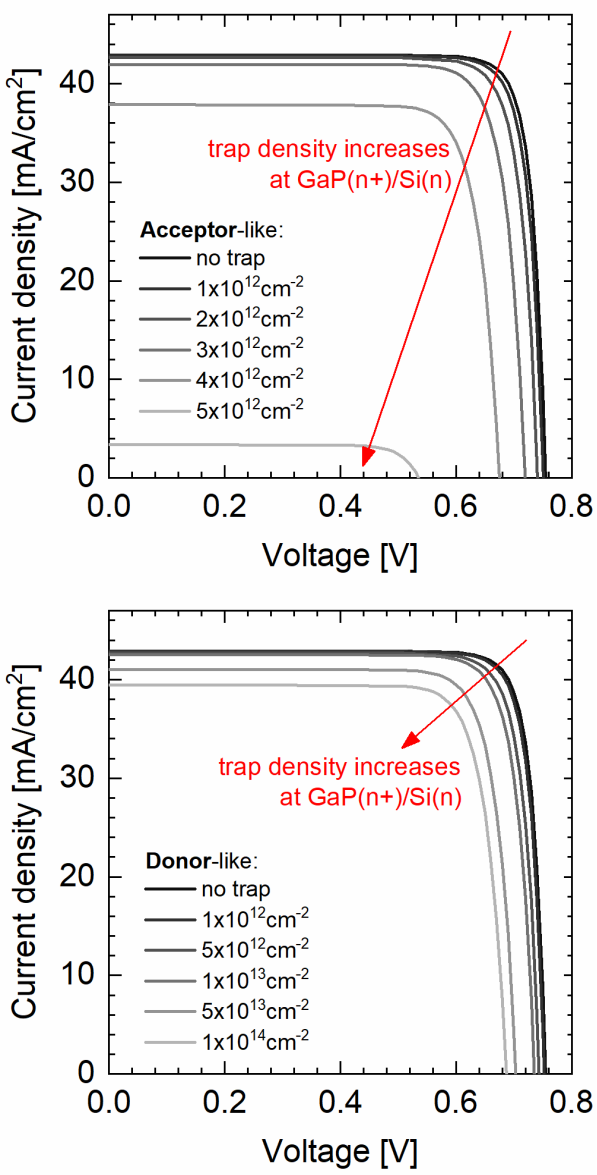

Figure 5.9 J-V curves of the simulated GP2 cells with either acceptor-like midgap traps or donor-like midgap traps at the GaP(n+)/Si(n) interface.

5.5 Conclusion

We have investigated the effects of acceptor-like and donor-like midgap traps at the front GaP/Si interface in interdigitated back contact solar cells through numerical modeling. Both types of traps can severely lower the solar cell performance. However, a strong front

surface field reduces minority carriers at the interface, and thus effectively mitigate degradation caused by both types of traps. A front surface field robustly passivates the type of traps that can either be empty or trap minority carriers, compared to the other type of traps. Identifying the type of traps at the front interface in real structures is crucial to avoid device degradation.

Chapter 6

A LATTICE-MATCHED DILUTE-N GaNP(As)/Si THREE-TERMINAL TWO-JUNCTION SOLAR CELLS

6.1 Introduction to a Three-terminal Two-junction (3T2J) Tandem

Thermalization and transmission are two major intrinsic losses in solar cells [142]. The addition of a higher-bandgap junction onto a Si cell can reduce thermalization losses and achieve higher total efficiency [18], as discussed in Chapter 1.

For common two-junction (2J) tandem designs, the two subcells can be series-connected and output power with two terminals (2T), or be electrically independent with only optical coupling and output power with four terminals (4T). Both have advantages and disadvantages. 2T tandems are monolithic with a simple interconnection, the same as a single junction cell, however, the subcells are restricted by current matching; 4T tandems have flexible optimal material combinations and good spectral tolerance, but they have to sacrifice the simple interconnection, requiring additional power electronics to combine power output, as well as suffering some optical connection losses. A three-terminal (3T) tandem minimizes these tradeoffs, as it is monolithic but avoids current matching and allows flexible material combination and good spectral tolerance.

Nagashima *et al*. [143] proposed using a back-contact type bottom cell for 3T tandems to move the middle terminal to the back and maximize the illuminated area. They simulated an npn bipolar junction transistor (BJT) type AlGaAs/Si 3T tandem with 30.40% total efficiency. Warren *et al*. [144] modeled a tunnel junction (TJ) type GaInP/Si 3T tandem as a single diode connected to a Si IBC cell, and mapped the power generation with different

terminal voltage combinations, and found the total efficiency of a 3T tandem (32.5%) is superior to a 2T tandem (30.6%) and comparable to a 4T tandem (32.4%). Recently, Rienäcker *et al*. [20] measured a Si IBC cell with two base terminals and an emitter terminal in the front-back mode and the IBC mode, and emulated 3T tandem operation by applying a constant current source to the top base terminal. They then proposed an equivalent circuit model that can match their measurement.

Here we model a lattice-matched 3T2J tandem with dilute-N GaNP(As) on Si with Silvaco ATLAS [53], and explore the device performance as a function of material and structural parameters including the effects of traps at the middle GaP/Si interface on the tandem, and the optical coupling between the top and bottom cell. To avoid the complication of a tunnel junction, we model a BJT-type (discussed in [20]) design (Figure 6.1).

The same physical models as in Chapter 5 are used for the bottom cell. The same front surface reflectance specification is moved to the very top instead of one layer above Si. 10 passes of light trapping are allowed with a cutoff power fraction of 0.003. For dilute-N GaNP(As), optical properties from our calculation (Chapter 3) for $GaN_{0.021}P_{0.979}$ (1.97 eV) are used unless otherwise stated, carrier mobilities are taken from Hall measurements [107], [108], and the Shockley-Read-Hall lifetimes are varied as part of the investigation. According to experiments, the radiative lifetimes of GaNP(As) are above 60 ns [51], [145], [146], and the SRH lifetimes range from 0.1 ns to 3.0 ns [146], [147]. At room temperature, SRH recombination dominates. We simulated the GaNP(As) materials with $\tau_{SRH} = 0.3$ ns as a case representing material quality in the early development stage, and with $\tau_{SRH} = 10$

ns as a case for a case for improved material quality. Radiative recombination coefficient, $B_r = 1 \times 10^{-13}$ cm^3/s is used for GaP. Since the radiative lifetime of GaNP(As) is about 10 times larger than that of GaAs (~ 5 ns [148]), $B_r = 7.2 \times 10^{-11}$ cm^3/s is used for GaNP(As), 10 times smaller than that of GaAs [149]. Our simulations show that Auger recombination in GaP and GaNP(As) has negligible effect on the device performance, therefore it is not discussed here.

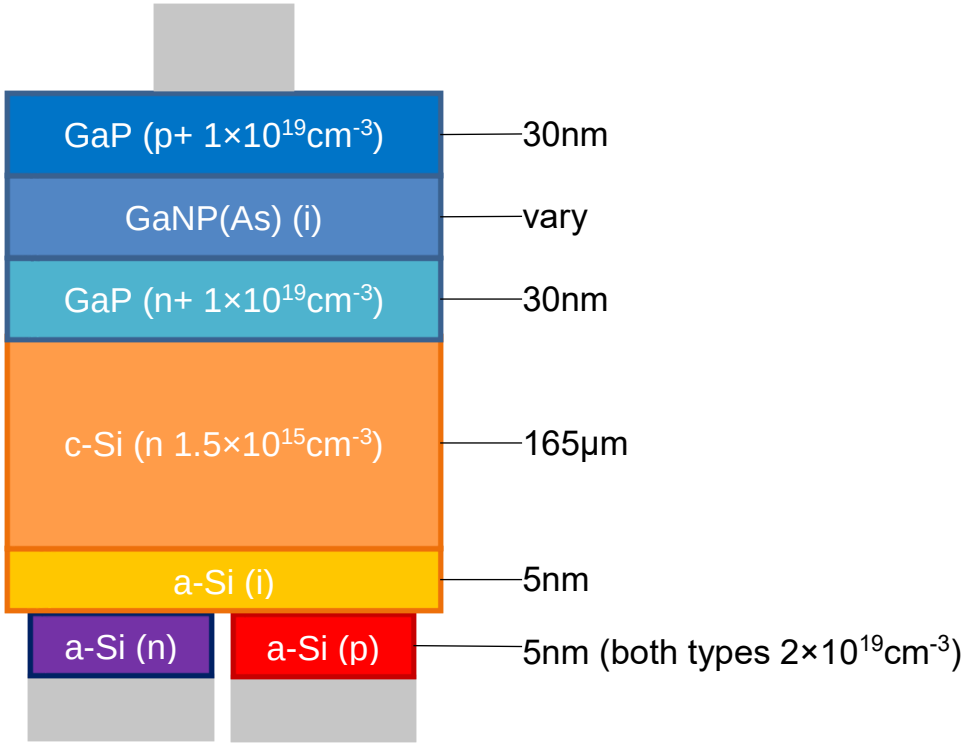

Figure 6.1 Schematic of a dilute-N GaNP(As)/Si 3-terminal 2-junction tandem solar cell (not to scale).

6.2 Independence Between the Two Sub-circuits

The main proposed advantage of a 3T tandem is that it forms two quasi-independent sub-circuits and allows current mismatch. Here, we simulate three cases (a) a 3T tandem as shown in Figure 6.1, (b) a single-junction GaNP cell with the top three semiconductor layers in Figure 6.1 plus a full metal back contact, and (c) a Si heterojunction IBC cell with a front GaP layer as in Chapter 5. For cases b and c, the intrinsic GaNP layers are 0.9 μm thick, with $\tau_{SRH} = 10$ ns. Results with $\tau_{SRH} = 0.3$ ns have the same trends for the independence investigation, and are not shown here.

Figure 6.2 compares the J-V curves of these cases. The J-V scans for cases b and c are straightforward, as there are only two terminals involved. The J-V scans for the 3T tandem is carried out as follow: (1) hold the front-back (FB) terminals at $V_{FB} = 0$ V, and scan the IBC terminals to obtain its maximum power point voltage $V_{IBC,mpp}$; (2) hold the IBC terminals at $V_{IBC} = V_{IBC,mpp}$, and scan the FB terminals to obtain its maximum power point voltage $V_{FB,mpp}$; (3) repeat steps 1 and 2 with $V_{FB} = V_{FB,mpp}$ step 1, until both $V_{FB,mpp}$ and $V_{IBC,mpp}$ converge. The J-V curves for the 3T sub-circuits are plotted after convergence is reached.

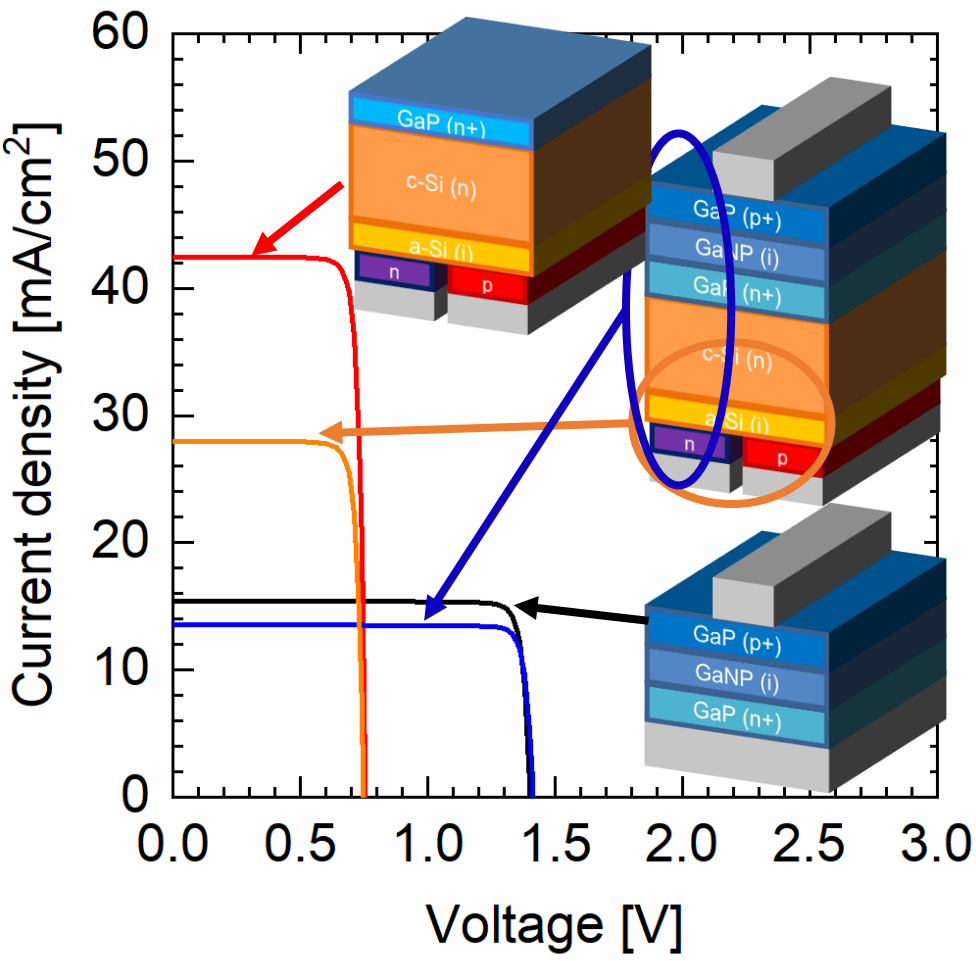

Figure 6.2 J-V curves of a single-junction GaNP cell (black), of a Si IBC cell (red), and of the GaNP sub-circuit (blue) and Si sub-circuit (orange) of a GaNP/Si 3T tandem.

It is seen in Figure 6.2 that both sub-circuit J-V curves have very similar V_{oc} and FF as their single-junction counterparts. Each sub-circuit can freely operate at any bias point while the other sub-circuit is held at an arbitrary bias point, and no current matching is required. Adding the GaP/GaNP layers on top of the Si IBC cell reduces the J_{sc} by 14.46 mA/cm^2, most of which is regenerated as the J_{sc} of the FB sub-circuit (13.62 mA/cm^2) while a small part is lost due to imperfect quantum efficiency. Removing the full back metal of the single-junction GaNP cell, and letting the high energy (> 1.97 eV) light

transmitted to the Si bottom cell makes a J_{sc} difference of 1.86 mA/cm^2. To confirm this is the reason for the J_{sc} difference between the black and blue curves, an extra case without reflection from the full back metal for the single-junction GaNP cell is simulated (see Figure 6.3), which gives the same EQE as the GaNP cell on a Si cell does, and gives smaller EQE than the 1J GaNP cell with 10x light trapping from about 420 nm to 660 nm, as this portion of light gets absorbed in the Si cell in a single pass. Figure 6.4 shows the reallocation of the EQE by rearranging the two single-junction cells into the 3T2J configuration. Figure 6.5 shows that the two sub-circuits are mostly electrically independent.

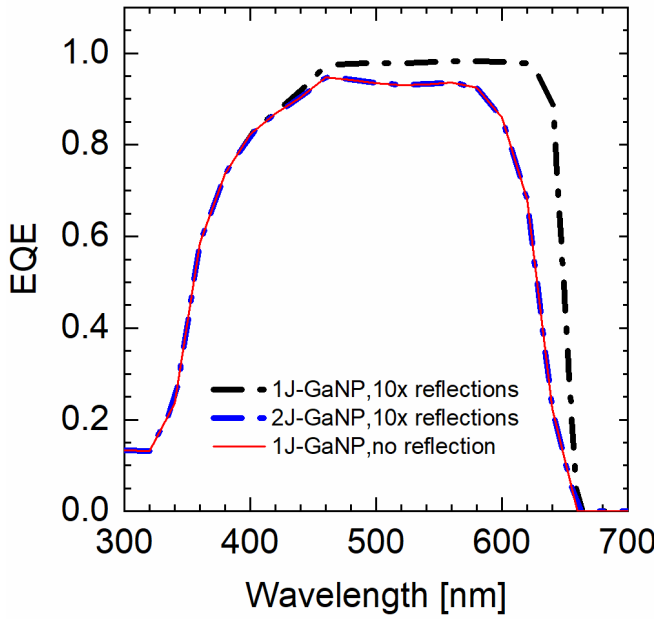

Figure 6.3 External quantum efficiency of the GaNP cell in a single-junction configuration with 10x light trapping (black dotted dashed line) and with no light trapping (red solid line), as well as in a 3T2J configuration (blue dotted dashed line).

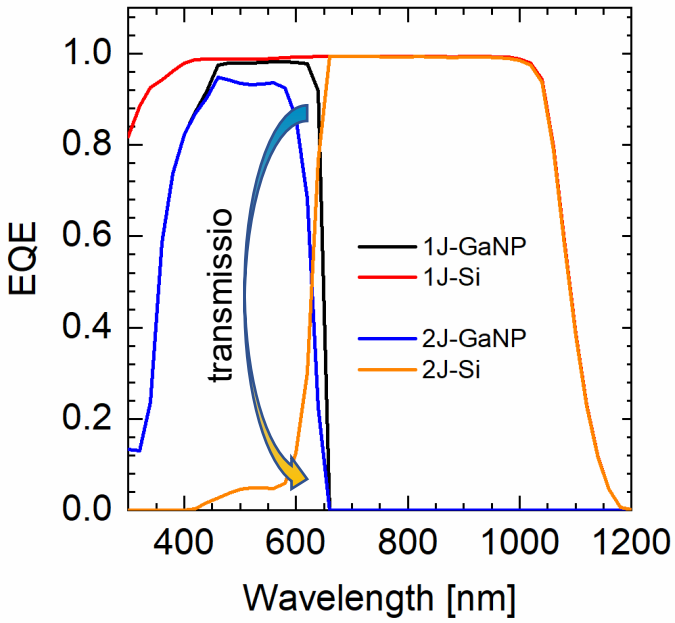

Figure 6.4 External quantum efficiency of the GaNP cell and Si cell in the 1J and 2J configurations. The arrow shows that part of the light between 420 nm and 660 nm transmits from the GaNP top layers into the Si bottom layers.

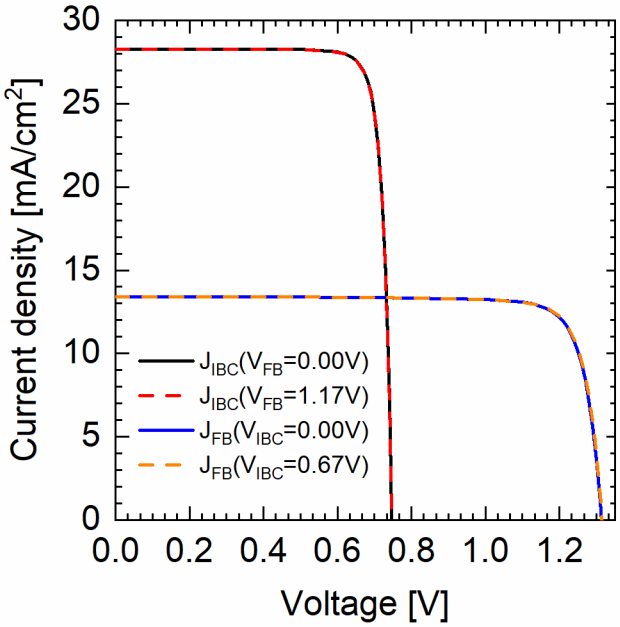

Figure 6.5 J-V curves of the two sub-circuits, IBC (both terminals at the back) and FB (front and back terminals). Each sub-circuit operates at two conditions: the other sub-circuit is at 0 bias or at maximum-power-point bias. Each sub-circuit has nearly identical J-V curves at the two conditions.

6.3 Effects of GaP/Si Interfacial Traps on the Three-terminal Tandem

As shown in Chapter 5, traps at the front GaP/Si interface of an IBC cell can severely impact the cell performance. While a front surface field (FSF) given by a GaP(n+)/Si(n) interface can passivate donor-like traps very well, a very high density of acceptor-like traps can render the FSF ineffective. In this section, we investigate effects of acceptor-like and donor-like single-level midgap traps at the GaP(n+)/Si(n) interface on the dilute-N GaNP/Si 3T2J tandem (see Figure 6.1).

Figure 6.6 shows the J-V curves and EQE of the GaNP subcell and of the Si subcell with and without donor-like traps (DLTs) at the GaP(n+)/Si(n) interface. It is seen that DLTs have essentially no effect on the GaNP subcell, as all the holes are blocked by the GaP(n+) layer and collected at the front terminal. Similar to the case of the single-junction Si IBC cell, the DLTs increase the recombination in the Si subcell and lower its performance, however, these effects are partially mitigated by the field at the GaP(n+)/Si(n) interface.

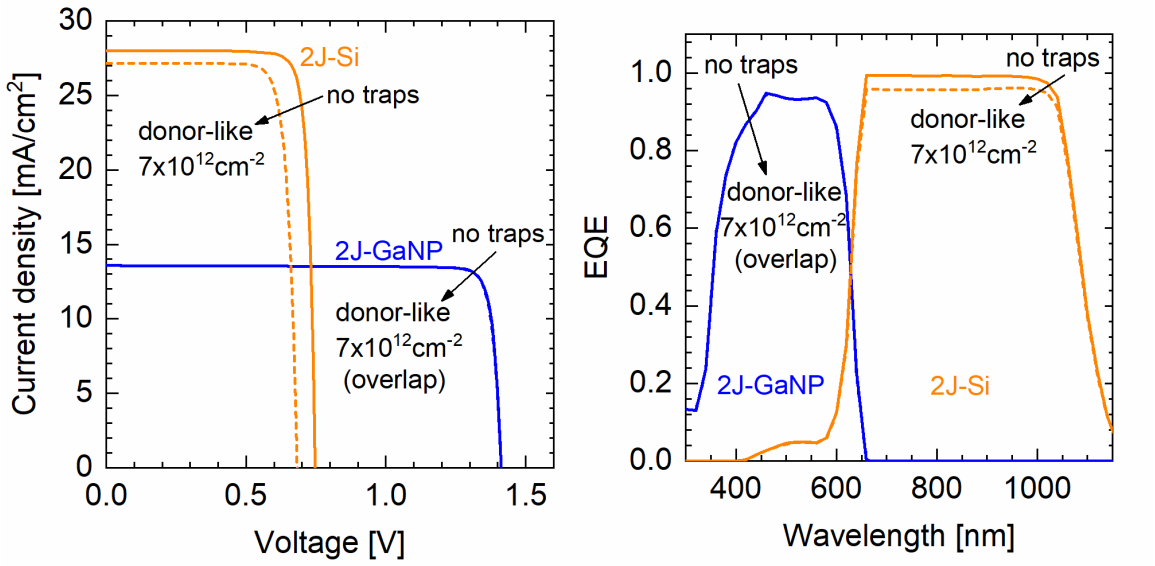

Figure 6.6 J-V curves and EQE curves for the GaNP subcell (blue) and the Si subcell (orange) in the 3T2J configuration without (solid) and with (dashed) donor-like traps at the GaP(n+)/Si(n) interface.

Figure 6.7 shows the J-V curves and EQE of the GaNP subcell and of the Si subcell with and without acceptor-like traps (ALTs) at the GaP(n+)/Si(n) interface. The ALTs do not affect the GaNP subcell at J_{sc}, and act as a resistance to electrons going from the topic to the bottom when the FB voltage is large. Also similar to the case of single-junction Si IBC cell, the ALTs trap electrons, become negatively charge, and flatten the band bending on the Si side. This allows both type of carriers recombine at the interface easily, and severely degrades the cell performance. This affects carriers generated near the front more than those generated near the back.

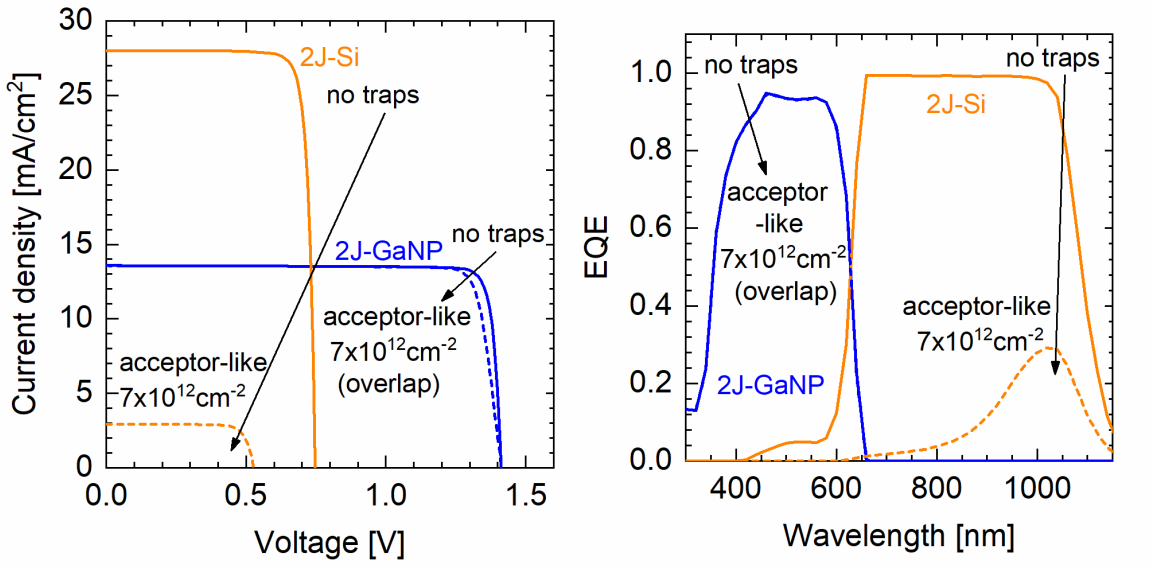

Figure 6.7 J-V curves and EQE curves for the GaNP subcell (blue) and the Si subcell (orange) in the 3T2J configuration without (solid) and with (dashed) acceptor-like traps at the GaP(n+)/Si(n) interface.

In summary, traps at the GaP(n+)/Si(n) interface have very small effect on the GaNP subcell, and they impact the Si subcell similar to that of a single-junction Si IBC cell. The presence of these traps makes the tandem rely more heavily on the GaNP subcell for power generation.

6.4 Optical Coupling in the Three-terminal Tandem

In the 3T2J tandem configuration, the GaNP subcell layers filter part of the shorter-wavelength solar spectrum, and allow the rest to transmit onto the Si subcell (Figure 6.8). More absorption in the GaNP subcell means less absorption in the Si subcell. The addition of an ideal higher-bandgap junction on a single-junction Si cell should reduce thermalization losses. However, if the higher-bandgap junction has poor transport

properties, the electrical loss in the higher-bandgap junction may cancel the gain in reduced thermalization to the Si band edges.

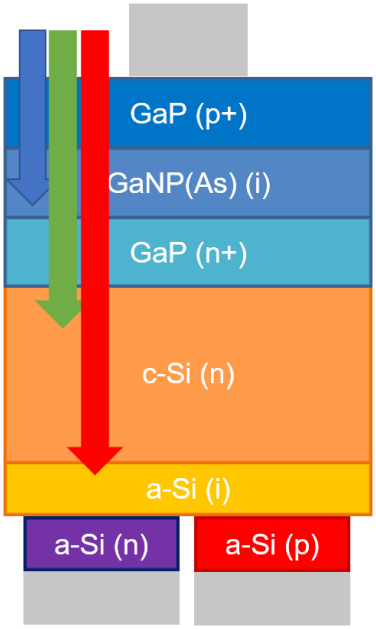

Figure 6.8 Schematic of optical coupling in the 3T2J tandem.

In this section, we investigate how the thickness of the dilute nitride absorber impact the tandem performance, under scenarios for different material qualities, $\tau_{SRH} = 0.3$ ns and $\tau_{SRH} = 10$ ns, as discussed in an earlier section. For bandgap engineering, we also simulated the 3T2J tandem using dilute-N GaNP(As) of different bandgaps, $E_g = 1.97$ eV ($GaN_{0.021}P_{0.979}$) and $E_g = 1.70$ eV ($GaN_{0.043}P_{0.856}As_{0.101}$), both lattice-matched to Si. Figure 6.9 shows the two input absorption spectra for the dilute nitrides calculated with the method in Chapter 3. One should note that $GaN_{0.043}P_{0.856}As_{0.101}$ absorbs photons with energy lower than 1.97 eV while $GaN_{0.021}P_{0.979}$ does not, and that the former materials absorbs stronger almost at every photon energy than that latter.

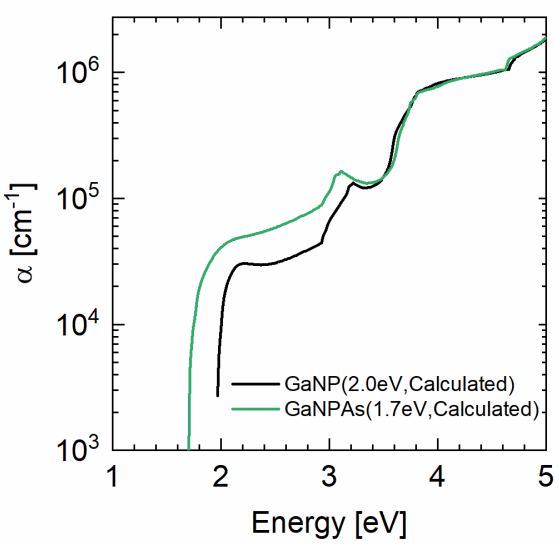

Figure 6.9 Absorption spectra calculated for two dilute-N alloys lattice-matched to Si: $GaN_{0.021}P_{0.979}$ (E_g = 1.97 eV) and $GaN_{0.043}P_{0.856}As_{0.101}$ (E_g = 1.70 eV).

Figure 6.10 compares the total tandem efficiency as a function of the $GaN_{0.021}P_{0.979}$ (E_g = 1.97 eV) layer thickness for different lifetimes ($\tau_{GaNP,SRH}$). Here the SRH recombination centers are assumed to be a single-level state that has the same energy as the intrinsic Fermi level, for the case of the most effective SRH recombination. As the SRH lifetime increases from 0.3 ns to 10 ns and to infinity, the optimum layer thickness increases from 0.4 μm to 0.9 μm and to above 2μm, and the optimum tandem efficiency increases from 29.6% to 32.9% and to above 37.7%.

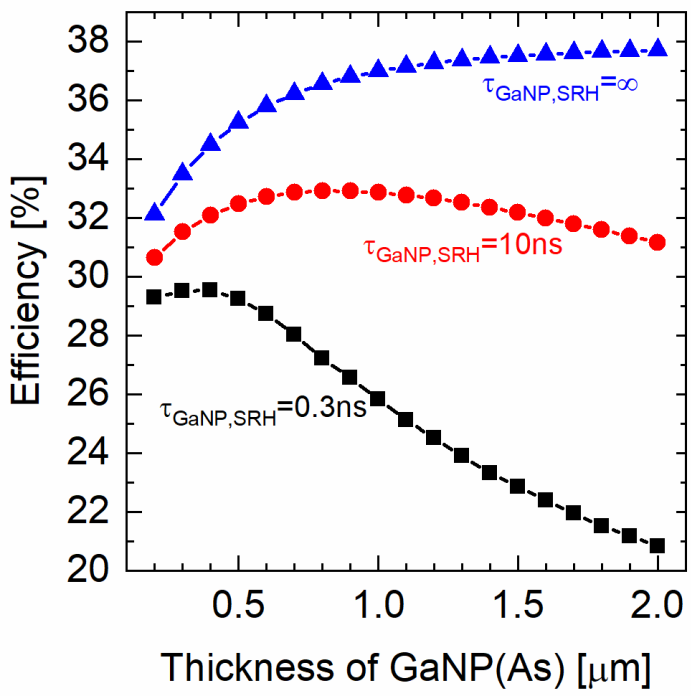

Figure 6.10 Efficiency of the 3T2J tandem as a function of layer thickness of $GaN_{0.021}P_{0.979}$ (E_g = 1.97 eV) with different SRH lifetimes.

To analyze the effects in more details, we decomposed the tandem efficiencies into subcell efficiencies (Figure 6.11). Similar to those of the tandem, the optimum thickness and efficiency of the GaNP subcell increases with the increasing SRH lifetime. As the GaNP thickness increases, the efficiency of the Si subcell decreases, as less light penetrates through the III-V layers onto the bottom Si subcell. However, the change in SRH lifetime of GaNP does not change the effects of the GaNP thickness on the Si subcell. This is because the two subcells are essentially electrically independent and couple only optically (Section 6.2).

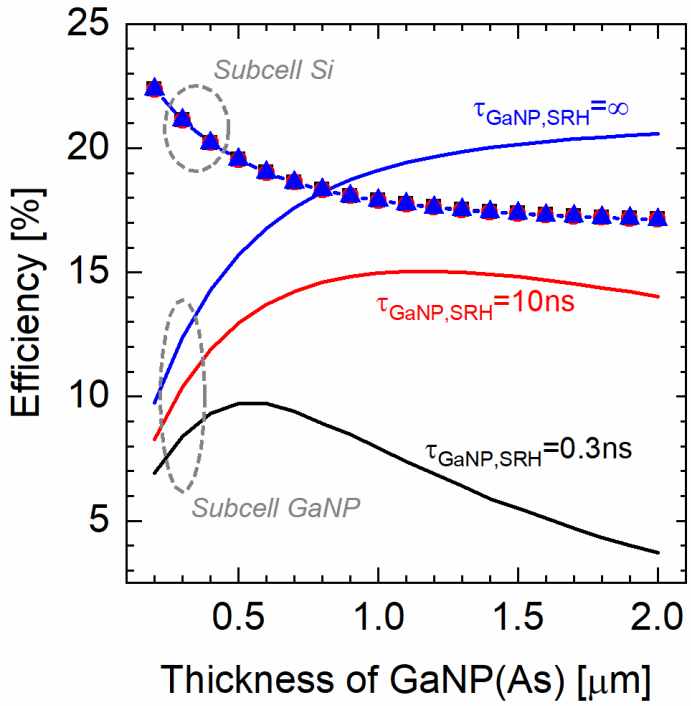

Figure 6.11 Efficiencies of the Si subcell (symbolled lines) and of the GaNP subcell (solid lines) as a function of layer thickness of $GaN_{0.021}P_{0.979}$ (E_g = 1.97 eV) with different SRH lifetimes.

To better explain the effect of the GaNP thickness on the performance of the GaNP subcell, the J-V parameters of the GaNP subcell are plotted as a function of the GaNP thickness (Figure 1.2). As the GaNP layer becomes thicker, more light is absorbed in the GaNP subcell. With a low SRH lifetime (0.3 ns), this initially raises the J_{sc} up. However, when the layer is thicker than ~ 1 μm, the decrease in free carriers through recombination starts to over compensate the increase in photogenerated carriers, and the J_{sc} reduces. As the SRH lifetime decreases or as the GaNP thickness increases, recombination and resistance increase, therefore the V_{oc} and FF decrease. One exception is the FF increases as the GaNP thickness increases for the case with infinite SRH lifetime, which is not well understood yet. One should note that the W_{oc} ($= E_g/q - V_{oc}$) values for the case with 10

ns SRH lifetime are similar to the experimentally measured values in Ref. [150], indicating that improved material quality in the future may allow SRH lifetime longer than 10 ns.

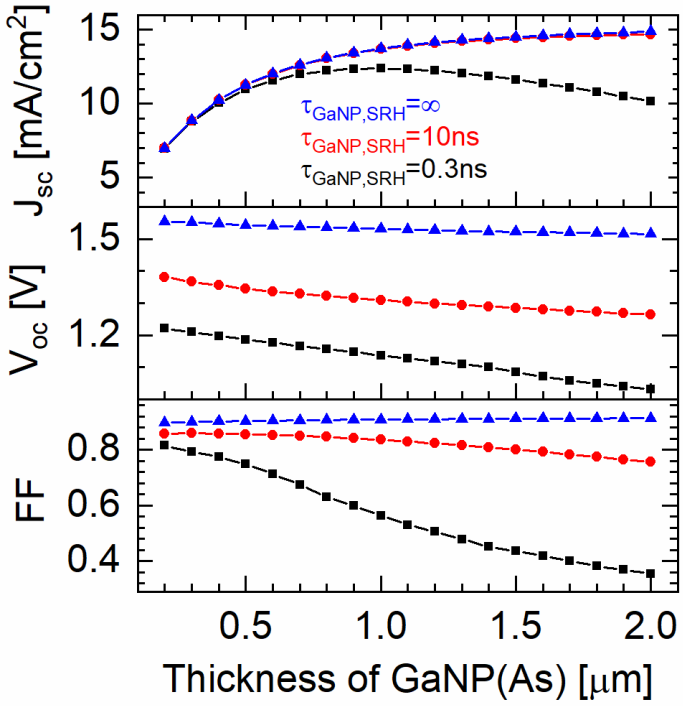

Figure 6.12 J_{sc}, V_{oc}, and fill factor of the GaNP subcell (solid lines) as a function of layer thickness of $GaN_{0.021}P_{0.979}$ (E_g = 1.97 eV) with different SRH lifetimes.

Detailed balance calculations show that an unconstrained 2J tandem with bandgap combinations 1.70eV/1.12eV and 1.97eV/1.12 eV should give similar tandem efficiencies. In Figure 6.13, we compare the tandem performance with bandgap combinations 1.70eV/1.12eV and 1.97eV/1.12 eV using realistic parameters for the GaNP(As)/Si material system, to inform future bandgap engineering. Since detailed balance modeling assumes perfect carrier collection, we show here results with a scenario where the carrier collection property is poor ($\tau_{GaNP(As),SRH} = 0.3$ ns) to see the effects more clearly. As the GaNP(As) thickness increases, the Si subcell efficiency drops more quickly for

$GaN_{0.043}P_{0.856}As_{0.101}$ than for $GaN_{0.021}P_{0.979}$, as the former absorbs more strongly over a wider spectrum range. This also leads to higher efficiency in the GaNPAs subcell when the layer is thinner than 1 μm. As shown in Figure 6.14, this is mostly attributed to the higher J_{sc} for $GaN_{0.043}P_{0.856}As_{0.101}$. However, the V_{oc} and fill factor of the $GaN_{0.043}P_{0.856}As_{0.101}$ cell are lower than those of the $GaN_{0.021}P_{0.979}$ cell, indicating higher recombination due to higher photogenerated carrier concentration. Therefore, when the dilute nitride layer is thick, the $GaN_{0.043}P_{0.856}As_{0.101}$ cell has lower efficiency than the $GaN_{0.021}P_{0.979}$ cell. Overall, when the material quality is poor, the gain in the top dilute nitride cell with a lower bandgap is less than the loss in the bottom Si cell, hence the optimum tandem efficiency is lower for the lower-bandgap case, which is different from the detailed balance prediction.

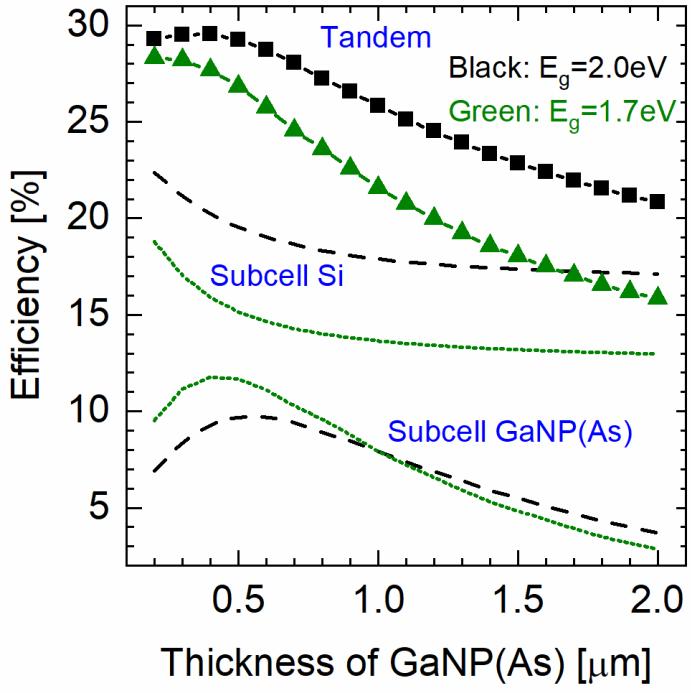

Figure 6.13 Tandem and subcell efficiencies as a function of layer thickness of 1.97 eV $GaN_{0.021}P_{0.979}$ (black) and of 1.70 eV $GaN_{0.043}P_{0.856}As_{0.101}$ (green). $\tau_{GaNP(As),SRH} = 0.3$ ns for both cases.

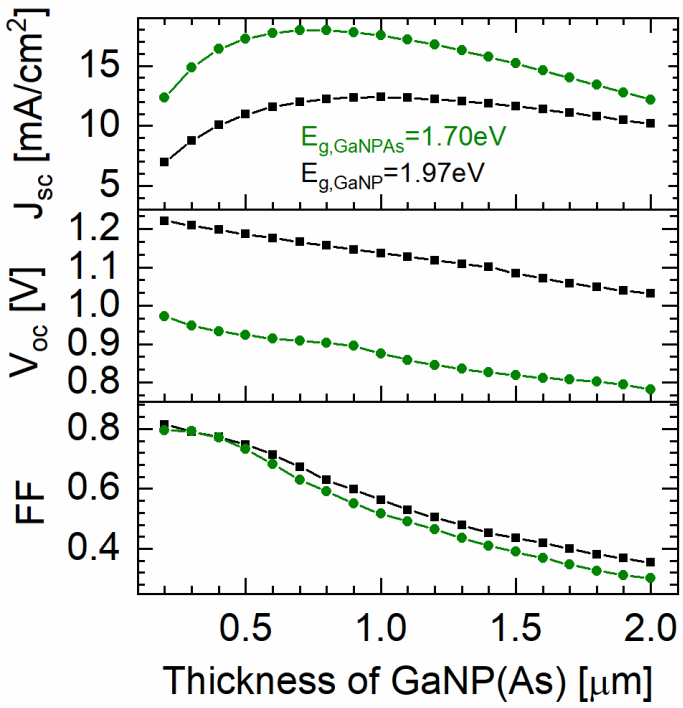

Figure 6.14 J_{sc}, V_{oc} and fill factor of the GaNP(As) subcell efficiency as a function of layer thickness of 1.97 eV $GaN_{0.021}P_{0.979}$ (black) and of 1.70 eV $GaN_{0.043}P_{0.856}As_{0.101}$ (green). $\tau_{GaNP(As),SRH} = 0.3$ ns for both cases.

Chapter 7

CONCLUSION

7.1 Summary

We have optimized the $sp^3d^5s^*s_N$ tight-binding parametrization for dilute-N GaNP and GaNAs by fitting to their experimental bandgaps, and have predicted the bandgaps of dilute-N GaNPAs lattice-matched to Si as a function of [N] (or [As]). The bandgaps range from 1.63 eV to 1.97 eV, covering the optimal top cell bandgap on a Si bottom cell as predicted by detailed balance calculation.

We then calculated the momentum matrix element of dilute-N GaN(P,As) as a simple derivative of the $sp^3d^5s^*s_N$ Hamiltonian, and carried out integration throughout the first irreducible wedge of the Brillouin zone to obtain their first-order optical response functions. The calculated optical response functions expose sharp transition features that facilitate composition dependent analysis. The trends shown in these theoretical results are in excellent agreement with experimental reports. These realistic optical results also suggest that our optimized $sp^3d^5s^*s_N$ model can describe the dilute-N alloy electronic structure quite accurately.

The calculated electronic structure of dilute-nitride GaNP was then input into a fullband Monte Carlo algorithm to model its carrier transport, in an effort to identify the limiting mechanism for electrical properties in these materials. We found that the $sp^3d^5s^*s_N$ model largely accounts for the N incorporation effect on reducing the electron mobility of dilute-N GaNP. But the effect is slightly overestimated, which is probably due to an overestimation of the effective mass. As expected, the $sp^3d^5s^*s_N$ model does not account

for any effect on the decrease of hole mobility with N incorporation, as the valence band remains unchanged in this model. Alloy scattering can lower the hole mobility rapidly, but cannot explain the experimentally measured hole mobility independence of N content. Further investigation is needed.

The epitaxy of GaP on Si is needed as a buffer for a GaNP(As)/Si lattice-matched tandem. But a GaP/Si interface may have structural defects, such as antiphase domains, and the heterovalent nature of the interface induces localized midgap states as well [125]. We found that midgap traps at the front GaP/Si interface can be detrimental to the Si interdigitated back contact cell. A front surface field at a GaP(n+)/Si(n) interface can passivate donor-like traps very well, but it can only passivate acceptor-like traps up to certain trap density, beyond which the filled acceptor-like traps can destroy the band bending which is instrumental to the passivation effect. Identifying the type of traps at the interface is critical for device development.

Finally, we modeled a lattice-matched dilute-N GaNP(As)/Si three-terminal two-junction tandem of the bipolar junction transistor type. The two subcells operate quasi-independently. Midgap traps have a minimal effect on the GaNP(As) subcell, and impact the tandem by degrading the Si subcell as discussed for the single-junction Si IBC cell. If the carrier lifetime (or diffusion length) of the GaNP(As) material is shorter, then the optimal bandgap of the dilute nitride should be larger, and the optimal thickness of the dilute nitride layer should be thinner. If carrier lifetime is 10 ns, a 3T tandem efficiency of 33% can be achieved, which is 6.3% absolute higher than the current single-junction Si

efficiency record. For the radiative limit of the dilute-nitride GaNP(As), the tandem efficiency is about 38%.

7.2 Future Work

As mentioned in Chapter 3, the calculated absorption coefficients for the dilute nitrides are overestimated compared to experimental measurements. This could be due to the neglect of the inhomogeneity of the dilute nitride alloys by the virtual crystal type approach, or due to the exclusion of the localized states induced by N clustering. Two things may be attempted to address these possible causes: (1) use tight-binding Hamiltonians that represent large relaxed random supercells; (2) modify the $sp^3d^5s^*s_N$ model to account for not only isolated N state, but also N cluster states without using a supercell. The latter approach should be more in line with the goal of developing a computational economical tool for the calculation.

Improving the electrical properties of dilute-N GaNPAs alloys is critical for the 3T tandem development. However, we still have not identified the limiting mechanism to carrier transport in these materials. The large hole mobility decrease independent of N content could be caused by scattering due to a high density of dislocations, interstitial defects, or anti-site defects, which may originate from non-ideal epitaxial growth conditions. To test this, accurate dislocation scattering and other point defect scattering model needs to be implemented to check if the discrepancies can be compensated.

REFERENCES

[1] J. Nelson, *The Physics of Solar Cells*. Imperial College, UK, 2003.

[2] W. Shockley and H. J. Queisser, "Detailed Balance Limit of Efficiency of p-n Junction Solar Cells," *J. Appl. Phys.*, vol. 32, no. 3, p. 510, 1961.

[3] S. Rühle, "Tabulated values of the Shockley–Queisser limit for single junction solar cells," *Sol. Energy*, vol. 130, pp. 139–147, Jun. 2016.

[4] S. P. Bremner, M. Y. Levy, and C. B. Honsberg, "Analysis of Tandem Solar Cell Efficiencies Under AM1 . 5G Spectrum using a rapid flux calculation method," *Prog. Photovoltaics Res. Appl.*, vol. 16, pp. 225–233, 2008.

[5] K. Yoshikawa *et al.*, "Silicon heterojunction solar cell with interdigitated back contacts for a photoconversion efficiency over 26%," *Nat. Energy*, vol. 2, no. 5, 2017.

[6] M. A. Green *et al.*, "Solar Cell Efficiency Tables (Version 53)," *Prog. Photovoltaics Res. Appl.*, vol. 27, pp. 3–12, 2018.

[7] Wikimedia Commons, "Shockley-Queisser Limit Breakdown." [Online]. Available: https://commons.wikimedia.org/wiki/File:ShockleyQueisserBreakdown2.svg. [Accessed: 13-Feb-2018].

[8] M. A. Green, "Third generation photovoltaics: Ultra-high conversion efficiency at low cost," *Prog. Photovoltaics Res. Appl.*, vol. 9, no. 2, pp. 123–135, 2001.

[9] A. De Vos, "Detailed balance limit of the efficiency of tandem solar cells," *J. Phys. D. Appl. Phys.*, vol. 13, no. 5, pp. 839–846, May 1980.

[10] A. Martí and G. L. Araújo, "Limiting efficiencies for photovoltaic energy conversion in multigap systems," *Sol. Energy Mater. Sol. Cells*, vol. 43, pp. 203–222, 1996.

[11] A. S. Brown and M. A. Green, "Detailed balance limit for the series constrained two terminal tandem solar cell," *Phys. E*, vol. 14, pp. 96–100, 2002.

[12] J. Lee and C. B. Honsberg, "Limiting efficiencies of multijunction solar cells with multiple exciton generation," *IEEE J. Photovoltaics*, vol. 4, no. 3, pp. 874–880, 2014.

[13] M. A. Green, Y. Hishikawa, A. W. Y. H. Baillie, E. D. Dunlop, and D. H. Levi, "Solar cell efficiency tables (version 51)," *Prog. Photovoltaics Res. Appl.*, vol. 26, pp. 3–12, 2018.

[14] "MehrSi project achieves record 22.3% efficiency for tandem solar cell with III-Vs grown directly on silicon." [Online]. Available: http://www.semiconductor-today.com/news_items/2019/jan/fhg-ise_090119.shtml. [Accessed: 19-Jul-2019].

[15] R. Cariou *et al.*, "III-V-on-silicon solar cells reaching 33% photoconversion efficiency in two-terminal configuration," *Nat. Energy*, vol. 3, pp. 326–333, 2018.

[16] S. Essig *et al.*, "Raising the one-sun conversion efficiency of III–V/Si solar cells to 32.8% for two junctions and 35.9% for three junctions," *Nat. Energy*, vol. 2, no. 9, 2017.

[17] M. Jošt *et al.*, "Textured interfaces in monolithic perovskite/silicon tandem solar cells: Advanced light management for improved efficiency and energy yield," *Energy Environ. Sci.*, vol. 11, no. 12, pp. 3511–3523, 2018.

[18] "Perovskite world record | Oxford PV." [Online]. Available: https://www.oxfordpv.com/news/oxford-pv-perovskite-solar-cell-achieves-28-efficiency. [Accessed: 22-Jun-2019].

[19] E. L. Warren, M. G. Deceglie, M. Rienäcker, R. Peibst, A. C. Tamboli, and P. Stradins, "Maximizing tandem solar cell power extraction using a three-terminal design," *Sustain. Energy Fuels*, pp. 1141–1147, 2018.

[20] M. Rienäcker *et al.*, "Back-contacted bottom cells with three terminals: Maximizing power extraction from current-mismatched tandem cells," *Prog. Photovoltaics Res. Appl.*, vol. 27, pp. 410–423, 2019.

[21] Y.-H. Zhang *et al.*, "Bandgap energies as a function of lattice constants." [Online]. Available: https://mbe.engineering.asu.edu/wp-content/uploads/2018/11/Eg.jpg. [Accessed: 26-Jul-2019].

[22] J. F. Geisz and D. J. Friedman, "III-N-V semiconductors for solar photovoltaic applications," *Semicond. Sci. Technol.*, vol. 17, no. 8, pp. 769–777, 2002.

[23] M. Weyers, M. Sato, and H. Ando, "Red Shift of Photoluminescence and Absorption in Dilute GaAsN Alloy Layers," *Jpn. J. Appl. Phys.*, vol. 31, no. 7A, 1992.

[24] M. Kondow, K. Uomi, K. Hosomi, and T. Mozume, "Gas-Source Molecular Beam Epitaxy of GaN_xAs_{1-x} Using a N Radical as the N Source," *Jpn. J. Appl. Phys.*, vol. 33, no. 8A, pp. L1056–L1058, 1994.

[25] L. Bellaiche, S. H. Wei, and A. Zunger, "Localization and percolation in semiconductor alloys: GaAsN vs GaAsP," *Phys. Rev. B - Condens. Matter Mater. Phys.*, vol. 54, no. 24, pp. 17568–17576, 1996.

[26] L. Bellaiche, S. Wei, and A. Zunger, "Band gaps of GaPN and GaAsN alloys,"

Appl. Phys. Lett., vol. 70, pp. 3558–3560, 1997.

[27] W. G. Bi and C. W. Tu, "Bowing parameter of the band-gap energy of GaN_xAs_{1-x}," *Appl. Phys. Lett.*, vol. 70, pp. 1608–1610, 1997.

[28] R. Bhat, C. Caneau, and L. Salamanca-Riba, "Growth of GaAsN/GaAs, GaInAsN/GaAs and GaInAsN/GaAs quantum wells by low-pressure organometallic chemical vapor deposition," *J. Cryst. Growth*, vol. 195, pp. 427–437, 1998.

[29] J. N. Baillargeon *et al.*, "Luminescence quenching and the formation of the $GaP_{1-x}N_x$ alloy in GaP with increasing nitrogen content," *Appl. Phys. Lett.*, vol. 60, no. 20, pp. 2540–2542, 1992.

[30] X. Liu, S. G. Bishop, J. N. Baillargeon, and K. Y. Cheng, "Band gap bowing in GaP1-xNx alloys," *Appl. Phys. Lett.*, vol. 63, no. 2, pp. 208–210, 1993.

[31] W. G. Bi and C. W. Tu, "N incorporation in GaP and band gap bowing of GaN_xP_{1-x}," *Appl. Phys. Lett.*, vol. 69, no. 24, pp. 3710–3712, 1996.

[32] W. G. Bi and C. W. Tu, "N incorporation in InP and band gap bowing of InNxP1-x," *J. Appl. Phys.*, vol. 80, no. 3, pp. 1934–1936, 1996.

[33] K. M. Yu *et al.*, "Formation of diluted III – V nitride thin films by N ion implantation," *J. Appl. Phys.*, vol. 90, no. 5, pp. 2227–2234, 2001.

[34] H. Naoi, Y. Naoi, and S. Sakai, "MOCVD growth of InAsN for infrared applications," *Solid. State. Electron.*, vol. 41, no. 2, pp. 319–321, 1997.

[35] B. N. Murdin *et al.*, "Band anticrossing in dilute InN_xSb_{1-x}," *Appl. Phys. Lett.*, vol. 81, no. 2, pp. 256–258, 2002.

[36] IQE plc., "Solar Junction surpasses its previous World-Record with certified 44.1% cell efficiency on IQE's production qualified wafers," 2013. [Online]. Available: http://www.iqep.com/media/2013/08/solar-junction/. [Accessed: 25-Jan-2018].

[37] M. A. Green, K. Emery, Y. Hishikawa, W. Warta, and E. D. Dunlop, "Solar cell efficiency tables (version 41)," *Prog. Photovolt Res. Appl.*, vol. 21, pp. 1–11, 2013.

[38] R. A. Logan, H. G. White, and W. Wiegmann, "Efficient green electroluminescence in nitrogen-doped GaP p-n junctions," *Appl. Phys. Lett.*, vol. 13, no. 4, pp. 139–141, Aug. 1968.

[39] R. Nicklin, C. D. Mobsby, G. Lidgard, and P. B. Hart, "Efficient yellow luminescence from vapour grown gallium phosphide with high nitrogen content,"

J. Phys. C Solid State Phys., vol. 4, no. 16, pp. L344–L347, Nov. 1971.

[40] J. A. Van Vechten, "Quantum Dielectric Theory of Electronegativity in Covalent Systems. I. Electronic Dielectric Constant," *Phys. Rev.*, vol. 182, no. 3, pp. 891–905, 1969.

[41] G. B. Stringfehow, "Calculation of the Solubility and Solid-Gas Distribution Coefficient of N in GaP," *j. Electrochem. soc. solid-state Sci. Technol.*, vol. 119, no. 12, pp. 1780–1782, 1972.

[42] W. Shan *et al.*, "Nature of the fundamental band gap in GaNxP1−x alloys," *Appl. Phys. Lett.*, vol. 76, no. 22, pp. 3251–3253, 2000.

[43] W. Shan *et al.*, "Band Anticrossing in GaInNAs Alloys," *Phys. Rev. Lett.*, vol. 82, no. 6, pp. 1221–1224, 1999.

[44] J. Wu, W. Shan, and W. Walukiewicz, "Band anticrossing in highly mismatched III-V semiconductor alloys," *Semicond. Sci. Technol.*, vol. 17, no. 8, pp. 860–869, Aug. 2002.

[45] S. Ilahi *et al.*, "Optical absorption and thermal conductivity of GaAsPN absorbers grown on GaP in view of their use in multijunction solar cells," *Sol. Energy Mater. Sol. Cells*, vol. 141, pp. 291–298, 2015.

[46] K. Zelazna, M. Gladysiewicz, M. P. Polak, S. Almosni, A. Létoublon, and C. Cornet, "Nitrogen-related intermediate band in P-rich GaN x P y As 1 − x − y alloys," no. November, pp. 1–8, 2017.

[47] J. F. Geisz, D. J. Friedman, and S. Kurtz, "GaNPAs Solar Cells Lattice-matched to GaP," in *29th IEEE Photovoltaic Specialists Conference*, 2002, pp. 864–867.

[48] J. Neugebauer and C. G. Van de Walle, "Electronic structure and phase stability of $GaAs_{1-x}N_x$ alloys," *Phys. Rev. B*, vol. 51, no. 16, pp. 10568–10571, 1995.

[49] S. Kurtz, a. a. Allerman, E. D. Jones, J. M. Gee, J. J. Banas, and B. E. Hammons, "InGaAsN solar cells with 1.0 eV band gap, lattice matched to GaAs," *Appl. Phys. Lett.*, vol. 74, no. 1999, pp. 729–731, 1999.

[50] J. F. Geisz, J. M. Olson, D. J. Friedman, K. M. Jones, R. C. Reedy, and M. J. Romero, "Lattice-Matched GaNPAs-on-Silicon Tandem Solar Cells," *31st IEEE Photovolt. Spec. Conf.*, pp. 695–698, 2005.

[51] S. Almosni *et al.*, "Evaluation of InGaPN and GaAsPN materials lattice-matched to Si for multi-junction solar cells," *J. Appl. Phys.*, vol. 113, no. 12, pp. 1–7, 2013.

[52] O. Durand *et al.*, "Monolithic Integration of Diluted-Nitride III-V-N Compounds on Silicon Substrates : Toward the III-V/Si Concentrated Photovoltaics," *Energy*

Harvest. Syst., vol. 1, no. 3–4, pp. 147–156, 2014.

[53] "Silvaco ATLAS." Sunnyvale, 2015.

[54] H. C. Casey, D. D. Sell, and K. W. Wecht, "Concentration dependence of the absorption coefficient for n- and p-type GaAs between 1.3 and 1.6 eV," *J. Appl. Phys.*, vol. 46, no. 1, pp. 250–257, 1975.

[55] G. E. Jellison, "Optical functions of GaAs, GaP, and Ge determined by two-channel polarization modulation ellipsometry," *Opt. Mater. (Amst).*, vol. 1, no. 3, pp. 151–160, Sep. 1992.

[56] N. Shtinkov, P. Desjardins, and R. A. Masut, "Empirical tight-binding model for the electronic structure of dilute GaNAs alloys," *Phys. Rev. B*, vol. 67, no. 8, pp. 1–4, 2003.

[57] F. Bloch, "Über die Quantenmechanik der Elektronen in Kristallgittern," *Zeitschrift für Phys.*, vol. 52, no. 7–8, pp. 555–600, 1929.

[58] J. C. Slater and G. F. Koster, "Simplified LCAO Method for the Periodic Potential Problem," *Phys. Rev.*, vol. 94, no. 6, pp. 1498–1524, 1954.

[59] P. Löwdin, "On the Non-Orthogonality Problem Connected with the Use of Atomic Wave Functions in the Theory of Molecules and Crystals," *J. Chem. Phys.*, vol. 18, no. 3, pp. 365–375, 1950.

[60] D. J. Chadi and M. L. Cohen, "Tight-Binding Calculations of the Valence Bands of Diamond and Zincblende Crystals," *phys. stat. sol.*, vol. 68, pp. 405–419, 1975.

[61] D. J. Chadi, "Spin-orbit splitting in crystalline and compositionally disordered semiconductors," *Physical Review B*, vol. 16, no. 2. pp. 790–796, 1977.

[62] P. Vogl, H. P. Hjalmarson, and J. D. Dow, "A Semi-Empirical Thight-Binding Theory of the Electronic Structure of Semiconductors," *J. Phys. Chem. Solids*, vol. 44, no. 5, pp. 365–378, 1983.

[63] J.-M. Jancu, R. Scholz, F. Beltram, and F. Bassani, "Empirical spds* tight-binding calculation for cubic semiconductors: General method and material parameters," *Phys. Rev. B*, vol. 57, no. 11, pp. 6493–6507, 1998.

[64] S. Steiger, M. Povolotskyi, H. H. Park, T. Kubis, and G. Klimeck, "NEMO5: A parallel multiscale nanoelectronics modeling tool," *IEEE Trans. Nanotechnol.*, vol. 10, no. 6, pp. 1464–1474, 2011.

[65] G. Klimeck, R. C. Bowen, T. B. Boykin, C. Salazar-Lazaro, T. a Cwik, and A. Stoica, "Si tight-binding parameters from genetic algorithm fitting," *Superlattices Microstruct.*, vol. 27, no. 2–3, pp. 77–88, 2000.

[66] D. Levine, “Users Guide to the PGAPack Parallel Genetic Algorithm Library (ANL-95/18),” 1996.

[67] M. Van Schilfgaarde, T. Kotani, and S. Faleev, “Quasiparticle self-consistent GW theory,” *Phys. Rev. Lett.*, vol. 96, no. 22, pp. 1–4, 2006.

[68] C. S. Wang and B. M. Klein, “First-principles electronic structure of Si, Ge, GaP, GaAs, ZnS, and ZnSe. II Optical properties,” *Phys. Rev. B*, vol. 24, no. 6, pp. 3417–3429, 1981.

[69] T. B. Boykin, G. Klimeck, R. C. Bowen, and F. Oyafuso, “Diagonal parameter shifts due to nearest-neighbor displacements in empirical tight-binding theory,” *Phys. Rev. B*, vol. 66, no. 12, pp. 1–6, 2002.

[70] Y. P. Tan, M. Povolotskyi, T. Kubis, T. B. Boykin, and G. Klimeck, “Tight-binding analysis of Si and GaAs ultrathin bodies with subatomic wave-function resolution,” *Phys. Rev. B - Condens. Matter Mater. Phys.*, vol. 92, no. 8, pp. 1–11, 2015.

[71] M. O. Nestoklon, R. Benchamekh, and P. Voisin, “Virtual crystal description of III-V semiconductor alloys in the tight binding approach,” *J. Phys. Condens. Matter*, vol. 28, no. 30, pp. 1–5, 2016.

[72] T. J. Kim *et al.*, “Dielectric functions of $In_xGa_{1-x}As$ alloys,” *Phys. Rev. B*, vol. 68, 2003.

[73] D. K. Gaskill, N. Bottka, L. Aina, and M. Mattingly, “Band-gap determination by photoreflectance of InGaAs and InAlAs lattice matched to InP,” *Appl. Phys. Lett.*, vol. 56, no. 13, pp. 1269–1271, 1990.

[74] R. E. Nahory, M. A. Pollack, and J. C. DeWinter, “Growth and characterization of liquid−phase epitaxial $In_xGa_{1-x}As$,” *J. Appl. Phys.*, vol. 46, no. 2, pp. 775–782, Feb. 1975.

[75] H. P. Xin, C. W. Tu, Y. Zhang, and A. Mascarenhas, “Effects of nitrogen on the band structure of GaN_xP_{1-x} alloys,” *Appl. Phys. Lett.*, vol. 76, no. 10, pp. 1267–1269, 2000.

[76] W. Shan *et al.*, “Nature of the fundamental band gap in GaN_xP_{1-x} alloys,” *Appl. Phys. Lett.*, vol. 76, no. 22, pp. 3251–3253, 2000.

[77] Y. Zou and S. M. Goodnick, “Tight-binding parameters for optical applications of GaAs , GaP , InAs , and their alloys,” *Submitted*, no. Xxxx.

[78] P. J. Klar *et al.*, “From N isoelectronic impurities to N-induced bands in the GaN[sub x]As[sub 1−x] alloy,” *Appl. Phys. Lett.*, vol. 76, no. 23, p. 3439, 2000.

[79] L. Malikova, F. H. Pollak, and R. Bhat, “Composition and temperature dependence of the direct band gap of GaAs$_{1-\text{x}}N$_\text{x}$ ($0 \le \text{x} \le 0.0232$) using contactless electroreflectance,” *J. Electron. Mater.*, vol. 27, no. 5, pp. 484–487, 1998.

[80] K. Uesugi, N. Morooka, and I. Suemune, “Reexamination of N composition dependence of coherently grown GaNAs band gap energy with high-resolution x-ray diffraction mapping measurements,” *Appl. Phys. Lett.*, vol. 74, no. 9, pp. 1254–1256, 1999.

[81] S. Kurtz *et al.*, “Incorporation of nitrogen into GaAsN grown by MOCVD using different precursors,” *J. Cryst. Growth*, vol. 234, pp. 318–322, 2002.

[82] I. Hayashi, “Optoelectronic Devices And Material Technologies For Photo-Electronic Integrated Systems,” *Jpn. J. Appl. Phys.*, vol. 32, no. 1 S, pp. 266–271, 1993.

[83] H. Yonezu *et al.*, “Elemental devices, circuits and processes for a monolithic Si/III-V-N alloy OEIC,” *Opt. Mater. (Amst).*, vol. 27, no. 5, pp. 799–803, 2005.

[84] S. Liebich *et al.*, “Laser operation of Ga(NAsP) lattice-matched to (001) silicon substrate,” *Appl. Phys. Lett.*, vol. 99, no. 7, 2011.

[85] R. Kudrawiec *et al.*, “Electronic Band Structure of $GaN_xP_yAs_{1-x-y}$ Highly Mismatched Alloys : Suitability for Intermediate-Band Solar Cells,” *Phys. Rev. Appl.*, vol. 1, 2014.

[86] Y. J. Kuang *et al.*, “GaNAsP: An intermediate band semiconductor grown by gas-source molecular beam epitaxy,” *Appl. Phys. Lett.*, vol. 102, no. 11, 2013.

[87] K. Zelazna *et al.*, “Nitrogen-related intermediate band in P-rich GaNxPyAs1-x-yalloys,” *Sci. Rep.*, vol. 7, no. 1, pp. 1–8, 2017.

[88] Y. Zhu, H. Yu, and W. Fan, “Band structures and optical gain of strained GaAs x P 1−x−y N y / GaP quantum wells,” *Appl. Phys. A Mater. Sci. Process.*, vol. 98, 2011.

[89] S. Almosni *et al.*, “Evaluation of InGaPN and GaAsPN materials lattice-matched to Si for multi-junction solar cells Evaluation of InGaPN and GaAsPN materials lattice-matched to Si for multi-junction solar cells,” vol. 123509, pp. 1–7, 2013.

[90] P. Y. Yu and M. Cardona, *Fundamentals of Semiconductors: Physics and Materials Properties*, 3rd rev. a. Berlin: Springer Berlin Heidelberg New York, 2005.

[91] L. C. Lew Yan Voon and L. R. Ram-Mohan, “Tight-binding representation of the optical matrix elements: Theory and applications,” *Phys. Rev. B*, vol. 47, no. 23,

pp. 500–508, 1993.

[92] D. E. Aspnes and A. A. Studna, “Dielectric functions of optical parameters of Si, Ge, GaP, GaAs, GaSb, InP, InAs, and InSb from 1.5 to 6.0 eV,” *Phys. Rev. B*, vol. 27, no. 2, pp. 985–1009, 1983.

[93] P. Lautenschlager, M. Garriga, S. Logothetidis, and M. Cardona, “Interband critical points of GaAs and their temperature dependence,” *Phys. Rev. B*, vol. 35, no. 17, pp. 9174–9189, 1987.

[94] S. Matsumoto *et al.*, “Optical characterization of metalorganic vapor-phase epitaxy-grown GaAs1-xNx alloys using spectroscopic ellipsometry,” *J. Cryst. Growth*, vol. 221, no. 1–4, pp. 481–484, 2000.

[95] M. Alouani, L. Brey, and N. E. Christensen, “Calculated Optical Properties of Semiconductors,” *Phys. Rev. B*, vol. 37, no. 3, 1998.

[96] I. A. Buyanova *et al.*, “Direct experimental evidence for unusual effects of hydrogen on the electronic and vibrational properties of GaNxP1-xalloys: A proof for a general property of dilute nitrides,” *Phys. Rev. B - Condens. Matter Mater. Phys.*, vol. 70, no. 24, pp. 1–4, 2004.

[97] G. Pozina, I. Ivanov, B. Monemar, J. V. Thordson, and T. G. Andersson, “Properties of molecular-beam epitaxy-grown GaNAs from optical spectroscopy,” *J. Appl. Phys.*, vol. 84, no. 7, pp. 3830–3835, 1998.

[98] S. Shokhovets, O. Supplie, C. Koppka, S. Krischok, and T. Hannappel, “Optical constants and origin of the absorption edge of GaPN lattice-matched to Si,” *Phys. Rev. B*, vol. 98, no. 7, pp. 1–11, 2018.

[99] G. Leibiger, V. Gottschalch, M. Schubert, G. Benndorf, and R. Schwabe, “Evolution of the optical properties of III-V nitride alloys: Direct band-to-band transitions in (formula presented) (formula presented),” *Phys. Rev. B - Condens. Matter Mater. Phys.*, vol. 65, no. 24, pp. 1–6, 2002.

[100] S. Matsumoto *et al.*, “Optical characterization of metalorganic vapor-phase epitaxy-grown GaAs1-xNxalloys using spectroscopic ellipsometry,” *J. Cryst. Growth*, vol. 221, no. 1–4, pp. 481–484, 2000.

[101] W. K. Hung, M. Y. Chern, Y. F. Chen, Z. L. Yang, and Y. S. Huang, “Optical properties of GaAs 1-x N x on GaAs,” *Phys. Rev. B*, vol. 62, no. 19, pp. 13028–13033, 2000.

[102] A. G. Thompson, M. Cardona, K. L. Shaklee, and J. C. Woolley, “Electroreflectance in the GaAs-GaP Alloys,” *Phys. Rev.*, vol. 146, no. 2, pp. 601–610, 1966.

[103] M. G. Craford, R. W. Shaw, A. H. Herzog, and W. O. Groves, “Radiative recombination mechanisms in GaAsP diodes with and without nitrogen doping,” *J. Appl. Phys.*, vol. 43, no. 10, pp. 4075–4083, 1972.

[104] J. F. Geisz, D. J. Friedman, J. M. Olson, S. R. Kurtz, and B. M. Keyes, “Photocurrent of 1 eV GaInNAs lattice-matched to GaAs,” *J. Cryst. Growth*, vol. 195, no. 1–4, pp. 401–408, 1998.

[105] S. R. Kurtz, J. F. Klem, A. A. Allerman, R. M. Sieg, C. H. Seager, and E. D. Jones, “Minority carrier diffusion and defects in InGaAsN grown by molecular beam epitaxy,” *Appl. Phys. Lett.*, vol. 80, no. 8, pp. 1379–1381, 2002.

[106] M. Da Silva *et al.*, “GaAsPN-based PIN solar cells MBE-grown on GaP substrates: toward the III-V/Si tandem solar cell,” *Phys. Simul. Photonic Eng. Photovolt. Devices Iv*, vol. 9358, p. 93580H, 2015.

[107] Y. Furukawa, H. Yonezu, A. Wakahara, Y. Yoshizumi, Y. Morita, and A. Sato, “Electrical properties of n-type GaPN grown by molecular-beam epitaxy,” *Appl. Phys. Lett.*, vol. 88, no. 14, 2006.

[108] Z. Liu, H. Kawanami, and I. Sakata, “Electrical properties of C-doped p -type GaP and GaPN grown by molecular beam epitaxy,” *Appl. Phys. Lett.*, vol. 96, no. 3, pp. 94–97, 2010.

[109] M. Fischetti and S. Laux, “Monte carlo analysis of electron transport in small semiconductor devices including band-structure and space-charge effects,” *Phys. Rev. B*, vol. 38, no. 14, pp. 9721–9745, 1988.

[110] M. Saraniti, S. M. Goodnick, and S. Member, “Hybrid Fullband Cellular Automaton / Monte Carlo Approach for Fast Simulation of Charge Transport in Semiconductors,” *IEEE Trans. Electron Devices*, vol. 47, no. 10, pp. 1909–1916, 2000.

[111] H. Brooks and Herring, “Scattering by Ionized Impurities in Semiconductors,” *Phys. Rev.*, vol. 83, p. 879, 1951.

[112] P. Y. Yu and M. Cardona, *Fundamental of Semiconductors - Physics and Material Properties*, First. Berlin: Springer-Verlag, 1996.

[113] B. K. Ridley, “Reconciliation of the Conwell-Weisskopf and Brooks-Herring formulae for charged-impurity scattering in semiconductors: Third-body interference,” *J. Phys. C Solid State Phys.*, vol. 10, no. 10, pp. 1589–1593, 1977.

[114] M. V. Fischetti and S. E. Laux, “Band structure, deformation potentials, and carrier mobility in strained Si, Ge, and SiGe alloys,” *J. Appl. Phys.*, vol. 80, no. 4, p. 2234, 1996.

[115] Z. Liu, H. Kawanami, and I. Sakata, “Electrical properties of C-doped p-type GaP and GaPN grown by molecular beam epitaxy,” *Appl. Phys. Lett.*, vol. 96, no. 3, p. 032106, 2010.

[116] Y. C. Kao and O. Eknoyan, “Electron and hole carrier mobilities for liquid phase epitaxially grown GaP in the temperature range 200-550 K,” *J. Appl. Phys.*, vol. 54, no. 5, pp. 2468–2471, 1983.

[117] Z. Liu, H. Kawanami, and I. Sakata, “Electrical properties of C-doped p -type GaP and GaPN grown by molecular beam epitaxy,” *Appl. Phys. Lett.*, vol. 96, no. 3, 2010.

[118] K. Yoshikawa *et al.*, “Exceeding conversion efficiency of 26% by heterojunction interdigitated back contact solar cell with thin film Si technology,” *Sol. Energy Mater. Sol. Cells*, vol. 173, no. June, pp. 37–42, 2017.

[119] T. J. Grassman, J. A. Carlin, B. Galiana, F. Yang, M. J. Mills, and S. A. Ringel, “MOCVD-Grown GaP/Si subcells for integrated III-V/Si multijunction photovoltaics,” *IEEE J. Photovoltaics*, vol. 4, no. 3, pp. 972–980, 2014.

[120] M. Feifel *et al.*, “Gallium Phosphide Window Layer for Silicon Solar Cells,” vol. 6, no. 1, pp. 384–390, 2016.

[121] C. Zhang, E. Vadiee, R. R. King, and C. B. Honsberg, “Carrier-selective contact GaP/Si solar cells grown by molecular beam epitaxy,” *J. Mater. Res.*, vol. 33, no. 4, pp. 414–423, 2018.

[122] M. Feifel *et al.*, “MOVPE Grown Gallium Phosphide-Silicon Heterojunction Solar Cells,” *IEEE J. Photovoltaics*, vol. 7, no. 2, pp. 502–507, 2017.

[123] T. Quinci *et al.*, “Defects limitation in epitaxial GaP on bistepped Si surface using UHVCVD–MBE growth cluster,” *J. Cryst. Growth*, vol. 380, pp. 157–162, 2013.

[124] C. Zhang, A. Boley, N. Faleev, D. J. Smith, and C. B. Honsberg, “Investigation of defect creation in GaP/Si(0 0 1) epitaxial structures,” *J. Cryst. Growth*, vol. 503, pp. 36–44, 2018.

[125] R. V. Meidanshahi, C. Zhang, Y. Zou, C. Honsberg, and S. M. Goodnick, “Electronic Structure of GaP/Si(001) Heterojunctions and the Role of Hydrogen Passivation,” *Prog. Photovoltaics Res. Appl.*, vol. 27, 2019.

[126] M. Powell and S. Deane, “Defect-pool model and the hydrogen density of states in hydrogenated amorphous silicon,” *Phys. Rev. B - Condens. Matter Mater. Phys.*, vol. 53, no. 15, pp. 10121–10132, 1996.

[127] C. M. Wu and E. S. Yang, “Carrier transport across heterojunction interfaces,” *Solid State Electron.*, vol. 22, no. 3, pp. 241–248, 1979.

[128] K. Yang, J. R. East, and G. I. Haddad, “Numerical modeling of abrupt heterojunctions using a thermionic-field emission boundary condition,” *Solid. State. Electron.*, vol. 36, no. 3, pp. 321–330, 1993.

[129] K. Yoshikawa *et al.*, “Silicon heterojunction solar cell with interdigitated back contacts for a photoconversion efficiency over 26%,” *Nat. Energy*, vol. 2, no. 5, 2017.

[130] “Basic Parameters of Silicon (Si).” [Online]. Available: http://www.ioffe.ru/SVA/NSM/Semicond/Si/basic.html. [Accessed: 19-Jul-2019].

[131] A. Froitzheim, R. Stangl, L. Elstner, M. Schmidt, and W. Fuhs, “Interface recombination in amorphous/crystalline silicon solar cells, a simulation study,” *29th IEEE Photovolt. Spec. Conf.*, pp. 1238–1241, 2002.

[132] “Basic Parameters of Gallium Phosphide (GaP).” [Online]. Available: http://www.ioffe.ru/SVA/NSM/Semicond/GaP/basic.html. [Accessed: 19-Jul-2019].

[133] “NSM Archive - Band structure and carrier concentration of Silicon (Si).” [Online]. Available: http://www.ioffe.ru/SVA/NSM/Semicond/Si/bandstr.html. [Accessed: 19-Jul-2019].

[134] K. K. Gandhi, A. Nejim, M. J. Beliatis, C. A. Mills, S. J. Henley, and S. R. P. Silva, “Simultaneous optical and electrical modeling of plasmonic light trapping in thin-film amorphous silicon photovoltaic devices,” *J. Photonics Energy*, vol. 5, Feb. 2015.

[135] S. Adachi, *Properties of Group-IV, III-V and II-VI Semiconductors*. Wiley, 2005.

[136] M. A. Green, “Self-consistent optical parameters of intrinsic silicon at 300 K including temperature coefficients,” *Sol. Energy Mater. Sol. Cells*, vol. 92, no. 11, pp. 1305–1310, 2008.

[137] Z. C. Holman *et al.*, “Current losses at the front of silicon heterojunction solar cells,” *IEEE J. Photovoltaics*, vol. 2, no. 1, pp. 7–15, 2012.

[138] “Electrical properties of Gallium Phosphide (GaP).” [Online]. Available: http://www.ioffe.ru/SVA/NSM/Semicond/GaP/electric.html#Recombination. [Accessed: 18-Jul-2019].

[139] S. S. Li and W. R. Thurber, “The dopant density and temperature dependence of electron mobility and resistivity in n-type silicon,” *Solid State Electron.*, vol. 20, pp. 609–616, 1977.

[140] J. M. Dorkel and P. Leturcq, “Carrier mobilities in silicon semi-empirically related to temperature, doping and injection level,” *Solid State Electron.*, vol. 24, no. 9,

pp. 821–825, 1981.

[141] K. Horio and H. Yanai, “Numerical modeling of heterojunctions including the thermionic emission mechanism at the heterojunct - Electron Devices, IEEE Transactions on,” *IEEE Trans. Electron Devices*, vol. 37, no. 4, pp. 1093–1098, 1990.

[142] L. C. Hirst and N. J. Ekins-Daukes, “Fundamental losses in solar cells,” *Prog. Photovoltaics Res. Appl.*, vol. 19, pp. 286–293, 2011.

[143] T. Nagashima, K. Okumura, K. Murala, and Y. Kimura, “Three-terminal tandem solar cells with a back-contact type bottom cell,” *Conf. Rec. IEEE Photovolt. Spec. Conf.*, pp. 1193–1196, 2000.

[144] E. L. Warren, M. G. Deceglie, M. Rienäcker, R. Peibst, A. C. Tamboli, and P. Stradins, “Maximizing tandem solar cell power extraction using a three-terminal design,” *Sustain. Energy Fuels*, vol. 2, pp. 1141–1147, 2018.

[145] I. A. Buyanova, G. Pozina, J. P. Bergman, W. M. Chen, H. P. Xin, and C. W. Tu, “Time-resolved studies of photoluminescence in GaNxP 1-x alloys: Evidence for indirect-direct band gap crossover,” *Appl. Phys. Lett.*, vol. 81, no. 1, pp. 52–54, 2002.

[146] A. Dobrovolsky *et al.*, “Optical properties of GaP/GaNP core/shell nanowires: a temperature-dependent study,” *Nanoscale Res. Lett.*, vol. 8, pp. 1–5, 2013.

[147] J. F. Geisz, R. C. Reedy, B. M. Keyes, and W. K. Metzger, “Unintentional carbon and hydrogen incorporation in GaNP grown by metal-organic chemical vapor deposition,” *J. Cryst. Growth*, vol. 259, no. 3, pp. 223–231, 2003.

[148] “Electrical properties of Gallium Arsenide (GaAs).” [Online]. Available: http://www.ioffe.ru/SVA/NSM/Semicond/GaAs/electric.html#Recombination. [Accessed: 18-Jul-2019].

[149] Y. P. Varshni, “Band-to-Band Radiative Recombination in Groups IV, VI, and III-V Semiconductors (I),” *Phys. status solidi*, vol. 19, no. 2, pp. 459–514, Jan. 1967.

[150] S. Sukrittanon *et al.*, “Enhanced conversion efficiency in wide-bandgap GaNP solar cells Enhanced conversion efficiency in wide-bandgap GaNP solar cells,” *Appl. Phys. Lett.*, vol. 107, no. 15, 2015.